

DISSERTATION

FLOODWAVE AND SEDIMENT TRANSPORT ASSESSMENT  
ALONG THE DOCE RIVER AFTER THE FUNDÃO TAILINGS DAM  
COLLAPSE (BRAZIL)

Submitted by

Marcos Cristiano Palu

Department of Civil and Environmental Engineering

In partial fulfillment of the requirements

For the Degree of Doctor of Philosophy

Colorado State University

Fort Collins, Colorado

Spring 2019

Doctoral Committee:

Advisor: Pierre Julien

Christopher Thornton

Robert Ettema

Sara Rathburn

Copyright by Marcos Cristiano Palu 2019

All Rights Reserved

## ABSTRACT

### FLOODWAVE AND SEDIMENT TRANSPORT ASSESSMENT ALONG THE DOCE RIVER AFTER THE FUNDÃO TAILINGS DAM COLLAPSE (BRAZIL)

The collapse of the Fundão Tailings Dam in November 2015 spilled 32 Mm<sup>3</sup> of mine waste, causing a substantial socio-economic and environmental damage within the Doce River basin in Brazil. Approximately 90% of the spilled volume deposited over 118 km downstream of Fundão Dam on floodplains. Nevertheless, high concentration of suspended sediment ( $\approx 400,000$  mg/l) reached the Doce River, where the floodwave and sediment wave traveled at different velocities over 550 km to the Atlantic Ocean. The one-dimensional advection-dispersion equation with sediment settling was solved to determine, for tailing sediment, the longitudinal dispersion coefficient and the settling rate along the river and in the reservoirs (Baguari, Aimorés and Mascarenhas). The values found for the longitudinal dispersion coefficient ranged from 30 to 120 m<sup>2</sup>/s, which are consistent with those in the literature. Moreover, the sediment settling rate along the whole extension of the river corresponds to the deposition of finer material stored in Fundão Dam, which particle size ranged from 1.1 to 2  $\mu$ m.

The simulation of the flashy hydrographs on the Doce River after the dam collapse was initially carried out with several widespread one-dimensional flood routing methods, including the Modified Puls, Muskingum-Cunge, Preissmann, Crank Nicolson and QUICKEST. All of these methods presented unsatisfactory results, with prediction errors in peak discharge up to 44%, and differences in timing to peak up to 5 hours.

A new and more accurate one-dimensional flood routing approach was then used, solving the full dynamic equation into an equivalent diffusive wave format and reformulating the hydraulic diffusion coefficient in terms of the Froude number and floodwave celerity. The numerical solution to this new approach was implemented using Crank Nicolson and QUICKEST schemes. The error in predicted peak discharge along the Doce River was reduced to 2%, and the maximum difference found in time to peak was about 1 hour.

Regarding sediment transport, a comprehensive one-dimensional numerical model is developed, coupling the new floodwave propagation algorithm with the numerical solution for advective sediment transport and settling. One of the main features of this model is the ability to simulate the propagation of the floodwave and sediment through the entire Doce River extension with or without reservoirs. A sensitivity analysis showed that a hypothetical decrease in water temperature from 30°C to 5°C would have resulted in a concentration 13 times higher at the outlet. In addition, without the presence of hydropower reservoirs on the Doce River, the sediment concentration at the basin outlet would have been 70,000 mg/l instead of the observed 1,600 mg/l.

Finally, a simplified numerical model based on the Doce River measurements can simulate the hypothetical collapse of 56 tailings dams in the Doce River basin to estimate the potential impact on the water supply for the towns along the river. Those simulation results show that tailings dams located in the Piracicaba basin, a Doce River sub-basin, have the highest potential to adversely impact the water supply of the downstream towns due the volume stored and proximity with populated towns. Ultimately, the collapse of the biggest dams in this sub-basin could affect approximately 1,000,000 people for several days.

## ACKNOWLEDGEMENTS

I believe in God and I believe in Jesus Christ. I thank God for giving me life, strength, courage, faith, peace, perseverance and especially for surrounding me with amazing people. My goal is to help and support others, doing this perhaps I can reflect at least a spark of the love, gentleness and goodness of Jesus Christ, who has a perfect and inspiring life.

I would like to thank Dr Pierre Julien for his priceless assistance in my studies and also for his constant enthusiasm, good mood and his friendship. I am grateful with my committee members: Dr. Robert Ettema, Dr. Christopher Thornton, and Dr. Sara Rathburn for their valuable contribution for my research. I also thank Linda Hinshaw for always being willing to help me.

I would like to thank CNPq (National Council for Scientific and Technological Development - Brazil) for the financial support and for given me the wonderful opportunity to study in U.S.

I am also thankful for all friends I made along this academic journey. I am grateful to the *Rising Stars team*: Chun-Yao Yang, Jai Hong Lee, Weimin Li, Woochul Kang, Neil Andika, Susan Cundiff, Sydney Doidge, Kristin LaForge, José Anderson do Nascimento Batista and Hwa Young Kim. I really appreciated their fellowship and contribution given during the seminars. Thanks also to Prof. Ernesto Sagás for helping me a lot when I just arrived in U.S.

Thanks for Randy and Jan Babcock, Steve and Edie Eckles, Tim and Lorna Green, Mel and Bonnie Crane, John and Susan Morse, and all the members of International Student Incorporated - Fort Collins for giving outstanding assistance to international students like me.

I also really appreciate the constant support and friendship of Wade and Carol, Cameron and Shanni Pacheco and all our friends of Christian Challenge - Fort Collins. I am also thankful for Pastor Bill and Priscila Prater, Mr. Bill Prater (*in memoriam*), Rev. Kimberly Salico-Diehl, John and Diana Finley, Mr. Lee and LauraLee and all the Carter's family, Don and Fran Lambert, Joe and Sandy Martinez, Jeff and Sandy Lindberg and all our friends of American Baptist Church, especially for receiving us like members of their family.

I am grateful for the support of all our family in Brazil, specially my parents José Carlos Palu and Maria Ilda Palu, my aunt Divanir Pallu and my parents-in-law Carlos Alfredo Kock and Luiza Kiyoko Fujita Kock. I am thankful for their patience and understanding during our absence. We missed you so much!

Finally, my deepest thank to my amazing and dedicated wife Susan. I am very grateful for her smile, for her help every day, unceasing support, encouragement and steadfast love. I love you so much!

## DEDICATION

*To Susan, my beloved wife*

## TABLE OF CONTENTS

ABSTRACT .....	ii
ACKNOWLEDGEMENTS .....	iv
DEDICATION .....	vi
LIST OF TABLES.....	x
LIST OF FIGURES .....	xii
LIST OF SYMBOLS .....	xvii
1. INTRODUCTION.....	1
1.1 The Fundão Dam Collapse .....	1
1.2 Data Availability.....	3
1.3 Problem Statement and Opportunity .....	4
1.4 Research Objectives .....	4
2. LITERATURE REVIEW.....	6
2.1 Tailings Dam Failure .....	6
2.2 Tailings Dams in Brazil.....	8
2.3 Modeling of Tailings Dam Failures .....	12
2.4 Steady Flow in Channels .....	15
2.5 Unsteady Flow in Channels .....	16
2.5.1 Governing Equations .....	16
2.5.2 Full Dynamic Wave.....	18
2.5.3 Diffusive Wave Approximation.....	19
2.5.4 Numerical Methods.....	21
2.6 Flood Routing in Reservoirs .....	23
2.7 Sediment Transport in Rivers.....	23
2.7.1 Classification .....	23

2.7.2	Suspended Load .....	25
2.7.3	One-Dimensional Advection-Dispersion Equation for Sediment Transport .....	26
2.7.4	Solutions for the One-Dimensional Advection-Dispersion Equation .....	27
2.7.5	Computation of the Longitudinal Dispersion Coefficient in Rivers .....	28
2.7.6	Changes in River Bed Elevation .....	29
2.8	Suspended Sediment Transport in Reservoirs .....	30
2.9	Hyperconcentrated Flows .....	31
3.	DATA COLLECTION .....	32
3.1	The Doce River Basin .....	32
3.2	The Fundão Dam .....	35
3.3	Available Data in the Doce River .....	39
3.3.1	Hydraulic Geometry and Bed Material .....	41
3.3.2	Cross Section Survey .....	42
3.3.3	Stage Discharge Curves .....	43
3.3.4	Hydrographs .....	46
3.3.5	Turbidity .....	48
3.3.6	Suspended Sediment Concentration .....	49
3.3.7	Particle Size Distribution .....	52
4.	DATA ANALYSIS .....	54
4.1	Spilled Volume Balance .....	54
4.2	Hyperconcentrated Flow Analysis .....	58
4.3	Mode of Sediment Transport along the Doce River .....	59
4.4	Longitudinal Dispersion Coefficient along the Doce River .....	60
4.5	Sediment Settling Rate .....	68
4.6	Volume of Sediment Trapped in the Doce River Reservoirs .....	72
4.7	Observed Difference between the Floodwave and Sediment Transport Propagation .....	74

4.8	Conclusions.....	76
5.	FLOOD ROUTING MODEL .....	77
5.1	Introduction .....	77
5.2	Upper Reach Simulation .....	79
5.3	Evaluation of Flood Routing Methods on the Doce River .....	82
5.4	New Approach to Calculate Floodwave Propagation.....	86
5.4.1	Test of the New Approach on the Doce River .....	89
5.5	Conclusions.....	98
6.	SEDIMENT TRANSPORT MODEL.....	99
6.1	Numerical Model of Suspended Sediment Transport .....	99
6.2	Effects of Changes in Water Temperature .....	105
6.3	Effects of Reservoirs .....	107
6.4	Conclusions.....	111
7.	MODEL APPLICATION TO SIMULATE THE HYPOTHETICAL COLLAPSE OF OTHER TAILINGS DAMS IN THE DOCE RIVER BASIN .....	112
7.1	Tailings Dams in the Doce River Basin.....	112
7.2	Modeling the Suspended Sediment Propagation after a Tailings Dam Failure.....	114
7.3	Conclusions.....	121
8.	CONCLUSIONS.....	122
	REFERENCES .....	125
	APPENDIX A .....	139
	APPENDIX B .....	144
	APPENDIX C .....	146
	APPENDIX D .....	154

## LIST OF TABLES

Table 2.1 – Tailings dams failures in Brazil .....	11
Table 2.2 – Summary of characteristics of widespread methods to calculate flood routing (Leonard, 1979; Abbott & Basco, 1990; Chapra, 2008; Price, 2009; Moin, 2010; Fenton, 2011; McCuen, 2016; USACE, 2016; Julien, 2018).....	22
Table 2.3 – Mode of sediment transport as function of shear and fall velocities .....	24
Table 2.4 – Empirical equations for the estimative of the longitudinal dispersion coefficient.....	28
Table 3.1 – Doce River reservoir data .....	33
Table 3.2 – Summary of collected data on the first survey .....	40
Table 3.3 – Doce River features .....	41
Table 3.4 – Date of survey before and after the dam break .....	43
Table 3.5 – Manning’s n coefficient in the Doce River gaging stations.....	45
Table 3.6 – Discharge peak observed along Doce River after the Fundão Dam collapse.....	47
Table 3.7 – Analysis of hydrograph flashiness .....	48
Table 3.8 – Maximum concentration observed in Doce River after the Fundão Dam collapse ..	50
Table 3.9 – Particle size of the stored material in the Fundão Dam reservoir and collected along the Doce River .....	52
Table 4.1 – Hyperconcentration analysis .....	58
Table 4.2 – Mode of sediment transport in Doce River after the Fundão Dam failure .....	59
Table 4.3 – Longitudinal dispersion coefficient evaluation along the Doce River .....	64
Table 4.4 – Doce River hydraulic parameters.....	65
Table 4.5 – Evaluation of the empirical expressions for the longitudinal dispersion coefficient..	67
Table 4.6 – Settling rate evaluation from the Doce River measurements.....	68
Table 4.7 – Settling rate and representative particle size in the Doce River reservoirs.....	70

Table 4.8 – Dimensionless parameter and particle size observed in the Doce River and in the reservoirs .....	71
Table 4.9 – Doce River reservoirs data and trap efficiency after the Fundão Dam collapse .....	72
Table 4.10 – Calculation of the trapped sediment in the Doce River reservoirs .....	73
Table 4.11 – Estimate of reservoir volume loss after the Fundão Dam collapse.....	74
Table 5.1 – Physical process and equations applied on the flow simulation along the Doce River .....	78
Table 5.2 – River reaches.....	79
Table 5.3 – Floodwave simulation parameters .....	81
Table 5.4 – Summary of parameters applied on the flood routing simulations on Reach A .....	83
Table 5.5 – Quantitative comparison between the flood routing models and the observed discharge on Reach A.....	85
Table 5.6 – Parameters applied on the flood routing simulations on Reach A using the new method .....	90
Table 5.7 – Flood routing simulation with new approach, Reach A.....	90
Table 5.8 – Floodwave simulation parameters .....	94
Table 6.1 - Physical process and equations applied in the sediment transport simulation along the Doce River .....	99
Table 6.2 – Sediment transport simulation parameters .....	100
Table 6.3 – Maximum simulated concentration as function of water temperature .....	105
Table 6.4 – Parameters of Candonga Dam reservoir to estimate the upstream concentration	107
Table 6.5 – Comparison between observed concentrations and the simulation without the reservoirs .....	109
Table 7.1 – Data of reservoirs in the tributaries(Geonetwork, 2007; CEMIG, 2018).....	116

## LIST OF FIGURES

Figure 1.1 – a) Bento Rodrigues Town b) Gesteira Town located 60 km downstream of the Fundão Dam, c) Candonga Dam spillway operation on November 6, d) Doce River at Governador Valadares City (station G4) on November 11, e) Aimorés Dam on November 16 and f) Arrival of the mud on the ocean on November 21 (Simon, 2015; Santos, 2015; Luz, 2015; Biló, 2015; Mesquita, 2015; Moraes, 2015) .....	2
Figure 1.2 – Sketch of floodwave propagation along the Doce River basin .....	3
Figure 2.1 – Location of the tailings dams in Brazil .....	10
Figure 2.2 – Relationship between Impoundment Volume and Outflow volume (Rico et al., 2008).....	13
Figure 2.3 – Relationship between peak discharge and dam factor (Rico et al., 2008).....	14
Figure 2.4 – Propagation of dynamic, kinematic and diffusive waves (Julien, 2018).....	18
Figure 3.1 – The Doce River basin .....	32
Figure 3.2 – The Doce River Hydropower reservoirs: a) Candonga Dam; b) Baguari Dam; c) Aimorés Dam and d) Mascarenhas Dam (Pimentel, 2016; Roberto, 2016; Mesquita, 2015; UOL, 2015).....	33
Figure 3.3 – Population in the Doce River basin.....	34
Figure 3.4 – The Fundão Dam (Morgenstern et al, 2016) .....	35
Figure 3.5 – The Fundão Dam profile (Rezende, 2013) .....	36
Figure 3.6 – Fundão Dam before (a) and after failure (b) (Morgenstern et al., 2016).....	37
Figure 3.7 – Fundão Dam location and the mud flood path.....	38
Figure 3.8 – Location of the data collection sites.....	39
Figure 3.9 – Cross section survey in the Doce River at stations G7 and G6.....	42
Figure 3.10 – Cross section survey in the Doce River at stations G5 and G4.....	42
Figure 3.11 – Cross section survey in the Doce River at stations G3 and G2.....	43

Figure 3.12 – Stage-discharge curves at stations G7 and G6 .....	44
Figure 3.13 – Stage-discharge curves at stations G5 and G4 .....	44
Figure 3.14 – Stage-discharge curves at stations G3 and G2 .....	44
Figure 3.15 – Doce River, 55 km downstream of station G3 in 05/03/2005, $Q \approx 1,000 \text{ m}^3/\text{s}$ (Google, 2018) .....	45
Figure 3.16 – Doce River, 55 km downstream of station G3 in 08/09/2017, $Q \approx 130 \text{ m}^3/\text{s}$ (Google, 2018) .....	46
Figure 3.17 – Observed hydrographs after the Fundão Dam failure .....	47
Figure 3.18 – Relationship of turbidity and suspended sediment concentration measured in the Doce River after the Fundão Dam collapse .....	49
Figure 3.19 – Hydrograph and suspended sediment concentration at gaging stations G6 and G5 .....	51
Figure 3.20 – Hydrograph and suspended sediment concentration at gaging stations G4 and G3 .....	51
Figure 3.21 – Hydrograph and suspended sediment concentration at gaging stations G2 and G1 .....	51
Figure 3.22 – Particle size distribution of the Fundão Dam impounded material and observed along the Doce River .....	53
Figure 4.1 – Estimative of sediment volume decay along the Doce River basin .....	55
Figure 4.2 – Fundão Dam site before the collapse (Google, 2015) .....	57
Figure 4.3 – Fundão Dam site after the collapse (Google, 2015) .....	57
Figure 4.4 – Application of the analytical solution using the superposition principle .....	61
Figure 4.5 – Routing procedure result in the reaches: G6-G5 and G5-Baguari Reservoir .....	62
Figure 4.6 – Routing procedure result in the reaches: Baguari Reservoir-G4 and G4-G3 .....	62
Figure 4.7 – Routing procedure result in the reaches: G3-S4 and Aimorés Reservoir-S3 .....	62
Figure 4.8 – Routing procedure result in the reaches: Mascarenhas reservoir-S2 and S2-G2 ..	63

Figure 4.9 – Routing procedure result in the reaches: G2-G1 and G1-S1.....	63
Figure 4.10 – Comparison between the longitudinal dispersion coefficients presented in the literature and the Doce Rive data (McQuivey & Keefer, 1974; Fischer et al., 1979; Rutherford, 1994; Deng, Singh, & Bengtsson, 2001; Kashefipour & Falconer, 2002; Carr & Rehmann, 2007). .....	65
Figure 4.11 – Comparison between the longitudinal dispersion coefficients presented in the literature and the Doce Rive data with $W/h = 66$ .....	66
Figure 4.12 – Comparison between the longitudinal dispersion coefficients presented in the literature and the Doce Rive data with $W/h = 500$ .....	67
Figure 4.13 – Comparison of the particle size distribution of the material stored in the Fundão Dam reservoir and the particle size related with the settling rate observed in the Doce River and in the reservoirs .....	69
Figure 4.14 – Dimensionless settling parameter as function of the particle size .....	71
Figure 4.15 – Comparison between the total volume trapped in the Doce River reservoirs using two different procedures .....	73
Figure 4.16 – Comparison between the floodwave celerity and sediment velocity in Doce River .....	75
Figure 5.1 – Processes in the numerical simulation .....	77
Figure 5.2 – River reaches division for the numerical simulation.....	78
Figure 5.3 – Floodwave simulation at the Upper Reach .....	81
Figure 5.4 – Test of flood routing procedures, Reach A upstream (Candonga Dam – G6).....	84
Figure 5.5 – Test of flood routing procedures, Reach A downstream (G6 – G5).....	84
Figure 5.6 – Application of the new hydraulic diffusivity coefficient on the Doce River reach using the Crank Nicolson scheme (Candonga Dam – G6).....	91
Figure 5.7 – Application of the new hydraulic diffusivity coefficient on the Doce River reach using the QUICKEST scheme (Candonga Dam – G6).....	91

Figure 5.8 – Application of the new hydraulic diffusivity coefficient on the Doce River reach using the Crank Nicolson scheme (G6 – G5) .....	92
Figure 5.9 – Application of the new hydraulic diffusivity coefficient on the Doce River reach using QUICKEST scheme (G6 – G5) .....	92
Figure 5.10 – Variation of flow depth over distance during the numerical simulation (Reach A)	93
Figure 5.11 – Variation of energy slope during the numerical simulation (Reach A) .....	93
Figure 5.12 –Hydrograph at station G4 and G3.....	95
Figure 5.13 – Hydrograph and flood routing at Aimorés Dam .....	95
Figure 5.14 –Hydrographs at station S2 and G2 .....	96
Figure 5.15 – Space time diagram of the floodwave propagation along the Doce River after the Fundão Dam collapse .....	97
Figure 6.1 – Sediment concentration along the Doce River after the Fundão Dam collapse and the limit of operation of WTP .....	101
Figure 6.2 – Water treatment plant at Colatina Town at station G2, (Machado, 2015).....	102
Figure 6.3 – Sediment deposition at the Reach A .....	103
Figure 6.4 – Sediment deposition at the Reach B .....	103
Figure 6.5 – Space time diagram of the sediment concentration and floodwave propagation along the Doce River after the Fundão Dam collapse .....	104
Figure 6.6 – Analysis of the effects of the water temperature in the suspended sediment propagation .....	106
Figure 6.7 – Suspended sediment simulation considering the hypothesis of inexistence of the Doce River hydropower reservoirs.....	108
Figure 6.8 – Sediment deposition along the Doce River (starting at Candonga Dam) without the reservoirs .....	109
Figure 6.9 – Space time diagram of the suspended sediment propagation and the floodwave assuming the hypothesis of inexistence of the reservoirs.....	110

Figure 7.1 – Tailings Dams in the Doce River basin .....	112
Figure 7.2 – Reaches affected in the hypothesis of failure of other tailings dams in the Doce River basin .....	113
Figure 7.3 – Sketch of the sediment propagation after a hypothetical tailings dam failure .....	117
Figure 7.4 – Example of the affected population after a hypothetical tailings dam failure on the Doce River basin.....	117
Figure 7.5 – Propagation of the high sediment concentration due the collapse of tailings dams in the Doce River basin.....	118
Figure 7.6 – Mapping the tailings dam according the number of potentially affected people ...	119
Figure 7.7 Tailings dams in the Piracicaba River sub-basin classified according to the potentially affected people .....	120
Figure 7.8 – Rank of the potential impact of the tailings dams in the Doce River Basins. ....	120

## LIST OF SYMBOLS

$A$	Cross sectional flow area
$d$	Molecular diffusion coefficient
$d_s$	Sediment size
$d_*$	Dimensionless particle diameter
$DR$	Discrepancy ratio
$c$	Solitary wave celerity
$C$	Sediment concentration
$\dot{C}$	Rate of sediment reaction
$C_a$	Courant number (flood)
$C_d$	Diffusive Courant number (flood)
$C_{as}$	Courant number (sediment)
$C_{ds}$	Diffusive Courant number (sediment)
$C_e$	Floodwave celerity
$C_i$	Downstream sediment concentration
$C_{oi}$	Upstream sediment concentration
$C_v$	Volumetric sediment concentration
$D$	Hydraulic diffusivity coefficient
$D_M$	Modified hydraulic diffusivity coefficient
$erfc$	Complementary error function
$Fr$	Froude number
$g$	Gravitational acceleration
$G$	Specific gravity
$H$	Tailings dam height
$h$	Flow depth
$k$	Sediment settling rate
$K$	Channel convey coefficient
$K_d$	Longitudinal dispersion coefficient

$K_{dp}$	Predicted longitudinal dispersion coefficient
$K_{dm}$	Measured longitudinal dispersion coefficient
$L_S$	Suspended load
$MAPE$	Mean of absolute percent error
$ME$	Mean of absolute error
$n$	Manning roughness coefficient
$P_{\Delta}$	Peclet number
$q$	Unit discharge
$q_{tx}, q_{ty}, q_{tz}$	Sediment flux per unit area
$Q$	Discharge
$Q_S$	Total suspended sediment discharge
$R^2$	Determination coefficient
$R_h$	Hydraulic radius
$Ro$	Rouse number
$RMSE$	Root mean square error
$RPD$	Relative percent difference
$S_f$	Energy line slope
$S_o$	Bed channel slope
$t$	Time
$T_E$	Trap efficiency
$u_*$	Shear velocity
$U$	Depth averaged flow velocity
$v_x$	Flow velocity in x direction
$W$	Channel width
$WTP$	Water treatment plant
$Y$	Channel bankfull depth
$\Delta x$	Spatial discretization in the numerical grid
$\Delta t$	Temporal discretization in the numerical grid
$\varepsilon$	Turbulent mixing coefficient

$\theta$	Preissmann weight factor
$\kappa$	Von Karman constant
$\tau$	Spilling duration
$\nu_m$	Kinematic viscosity of a mixture
$\omega$	Fall velocity
$\forall_s$	Volume of solids
$\forall_t$	Total volume
$\Omega$	Floodwave diffusivity

## 1. INTRODUCTION

The frequent collapse of tailings dams around the world has caused severe environmental and socio-economic impacts (Ayala-Carcedo, 1998; Lucas, 2001; Azam & Li, 2010; Chambers & Higman, 2011; Kossoff et al., 2014; Fernandes et al., 2016). When compared to water retention dams, the consequences of tailings dam failures are far more significant due the presence of waste materials from mining activities in the flow, which can result in irreparable environmental damage (Kossoff et al., 2014). Herein, this research presents an assessment about the propagation of the tailings after the Fundão Dam failure in 2015. The dominant sediment transport mode is characterized by huge suspended sediment concentration along the Doce River. This event resulted in the destruction of the Bento Rodrigues Town and caused extensive socio-economic environmental damage in the Doce River basin, therefore it is considered the worst Brazilian environmental accident that ever occurred (Marta-Almeida et al., 2016; Carmo et al., 2017).

### 1.1 The Fundão Dam Collapse

Fundão Dam was a 120 m high tailings dam located in the town of Mariana, State of Minas Gerais, southeast region of Brazil. The dam collapse on 5 November of 2015 released 32 million cubic meters of tailings, which caused the overtopping of the adjacent Santarém tailings dam, the destruction of Bento Rodrigues Town and substantial damage in other towns downstream. The accident caused 19 deaths. Figure 1.1 illustrates the impact of the passage of the mud along the Doce River basin while Figure 1.2 shows a sketch of the floodwave propagation.



**Figure 1.1 – a) Bento Rodrigues Town b) Gesteira Town located 60 km downstream of the Fundão Dam, c) Candonga Dam spillway operation on November 6, d) Doce River at Governador Valadares City (station G4) on November 11, e) Aimorés Dam on November 16 and f) Arrival of the mud on the ocean on November 21 (Simon, 2015; Santos, 2015; Luz, 2015; Biló, 2015; Mesquita, 2015; Moraes, 2015)**

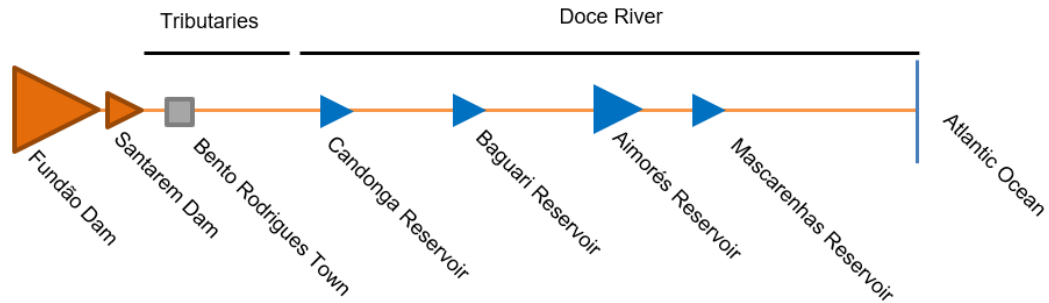


**Figure 1.2 – Sketch of floodwave propagation along the Doce River basin**

The resulting flood traveled a total distance of approximately 670 km, passing through four hydropower plant reservoirs. Although the spilled tailings were not toxic, the high sediment concentration caused the immediate death of nearly 3 tons of fish and the disruption of the water supply in 12 cities, affecting an estimated population of approximately 430,000 people (ANA, 2016a; IBAMA, 2016).

## 1.2 Data Availability

After the accident, the Geological Service of Brazil and the National Water Agency conducted several measurements in order to follow the floodwave and its high turbidity (CPRM & ANA, 2015a). These Brazilian agencies collected data of discharge, water level, temperature, dissolved oxygen, pH, turbidity, particle size and concentration of sediments in suspension. The main data used in this research are presented in Appendix A.

The availability of this type of data after a tailings dam collapse is uncommon in the literature (Rico et al., 2008). Therefore, this is a unique opportunity to analyze the transport of sediment (impounded tailings) in the water bodies after a tailings dam failure. Ultimately, the analysis and processing of the available measurements can be useful on the development of a sediment transport model, which is based on the observations of the river response after the abrupt pulse of large amount of suspended sediment under the unsteady or steady flow conditions.

### 1.3 Problem Statement and Opportunity

The Fundão Dam case highlights the devastating consequences of a tailings dam collapse. However, the mining activities have great economic importance to Brazil (and to several countries around the world as well) and the disposal of tailings in reservoirs is still the most commonly used method throughout the country.

To date, the literature indicates that most of the research about tailings dam failures is focused on defining the flood characteristics in the vicinity of the dam break only (Armanini et al., 2009; Kunkel, 2011; Lin & Li, 2012; Marsooli et al., 2013; Liu, 2018). Consequently, there is scarcity of publications with concerns about the transport of the impounded material in natural channels after this kind of event. In general, after a tailings dam failure or spill, the magnitude of high sediment concentration, the rate of deposition and its consequences along the river are essentially unknown.

Therefore, the development of a numerical model, which can be used to simulate other tailings dam failure and quantify the high concentrations into rivers, is needed. This effort could yield a new predictive methodology to evaluate the potential damage to living communities downstream.

### 1.4 Research Objectives

The purpose of this research is to use the information available from the Fundão Dam failure to advance the knowledge of the processes of sediment transport after tailings dam collapse or accidental spill. Thus, this research proposes a theoretical analysis and a one-dimensional numerical modeling of the flow conditions and sediment transport following the analysis based in the collected field data.

The specific objectives of this research are:

1. To analyze the data collected after the Fundão Dam failure in order to determine the proper equation and its parameters to model the suspended sediment transport (a) along the Doce River, and (b) into the hydropower reservoirs;
2. To develop a one-dimensional numerical model able to simulate (a) the observed floodwave propagation, and (b) the sediment transport and deposition along the Doce River and its reservoirs;
3. To use the calibrated model (a) for a parametric analysis of the most relevant variables, and (b) to simulate the hypothetical failure of other tailings dams within the Doce River basin to identify the dams with high damage potential in terms of water supply interruption in the towns located downstream.

## 2. LITERATURE REVIEW

### 2.1 Tailings Dam Failure

Tailings dam collapse causes the movement of the impounded material, which contains a dense mixture of solids, including heavy metals, and liquid. Thus, the spilled material flows under the force of gravity and the flood can travel at velocities of about 20 m/s (EPA, 2014).

Tailings dam failure has caused great distress worldwide. The earliest register of tailings dam collapse found in literature is the San Ildefonso Dam failure in Bolivia in 1626, where around 4,000 people were killed in the consequent flood (Kossoff et al., 2014). Recently, according with the ICOLD Committee on Tailings Dams and Waste Lagoons, by the date of publication there were 221 incidents registered around the world (ICOLD, 2001). In a more recent publication, Rico et al. (2008) mention the occurrence of 250 tailings dam failures. However, it is the consent among different researches that there is not a complete worldwide database of all the historical failures (Davies, 2002; Rico et al., 2008; Azam & Li, 2010). In addition, the frequency of incidents is worrisome. Davies et al. (2000) investigated the occurrences of collapses of tailings dams considering a 30 years database (1970-1999) concluding that in this period the rate was 2 to 5 major incidents per year. In all the years, there were at least two events. Moreover, Davies (2002) compared the occurrences of collapses of tailings dams with the conventional dams using the same 30 years database. The author concluded that the rate of tailings dam failure was approximately ten times higher than for water retention dams.

Azam and Li (2010) present a comprehensive statistical analysis of tailings dam failures around the world using a 100 years database (1910-2009). One of the main findings is that the frequency of incidence in the last decades (1990s and 2000s) is still 20 events per decade.

The authors stated that the frequency of the incidents changed geographically from the developed countries to the developing countries. Thus, according to Chambers and Higman (2011), after building tailings dams for about a century, the implication of storing a large amount of harmful waste in large impoundments is not still comprehended. The present-day events have showed that the nature of industrial hazards is not fully understood.

At present, tailings dams failures continue to occur worldwide at a disturbing rate (Azam & Li, 2010; Caldwell et al., 2015; WISE, 2019). To mention few: Kingston Fossil Plant 2008 (Tennessee – USA), Karamkem 2009 (Russia), Huancavelica 2010 (Peru), Mianyang City 2011 (China), Sotkamo 2012 (Finland), Obed Mountain Coal Mine 2013 (Canada), Dan River Steam Station 2014 (North Carolina – USA), Mount Polley 2014 (Canada), Buenavista 2014 (Mexico), Fundão 2015 (Brazil), Hpakant 2015 (Myanmar), Tonglvshan 2017 (China), Mishor Rotem 2017 (Israel), Huancapati 2018 (Peru), Cadia 2018 (Australia), Cieneguita 2018 (Mexico) and Brumadinho 2019 (Brazil).

Rico et al., (2008) points that the vulnerability of tailings dams compared with water storage dams is due some peculiar characteristics as: embankments built with residual material from mining activities, raising of the dam in multi-stages in order to increase storage capacity, lack of regulations on design criteria, the continuous necessity of monitoring in order to assure the dam stability and high cost of maintenance after the mine closure. The main recognized consequences of the collapse are: loss of life, environmental damage (as a massive discharge of tailings in a river system with a huge cleanup cost), social damage in downstream communities, infrastructure damage, extended production interruption, damage to company and industry image, economic consequences and legal responsibility for the company (Davies et al., 2000; Azam & Li, 2010; Chambers & Higman, 2011; Kossoff et al., 2014).

The discharge of tailings in river systems, which are often toxic, will potentially affect water sediment quality, aquatic and human life for hundreds of kilometers (Kossoff et al., 2014). An example of river contamination is the case of Baia Mare and Baia Borsa tailings dam in Romania, close to Ukrainian border. The spilled tailings, evaluated in 120 tons of cyanide, significant amount of lead, copper and zinc were released in the River Tisa, a major Danube tributary. The aftermath of this accident was tons of fish deaths in Romania, Hungary, Serbia and Bulgaria. The flow continued into the Danube River and eventually reached the Black Sea in a reach of 1,900 km (ICOLD, 2001; Kossoff et al., 2014).

Another remarkable point is that the most of incidents with tailings dams are unreported or misreported due to fears of bad publicity and legal ramifications, especially in developing countries (Davies, 2002; Rico et al., 2008). The lack of publication hinders the development of research related with this topic (EPA, 2014).

## 2.2 Tailings Dams in Brazil

The mining activities play a fundamental role in Brazil economy, because the country holds a large reserve of metallic and nonmetallic minerals (D'Agostino, 2008). As part of the process of mineral production, there is the production of tailings, which are mixtures of crushed rock and processing fluids from mills or concentrators that remain after the extraction of economic metals. The word 'tailings' is generic as it describes the by-product of several extractive industries, including those for aluminum, coal, oil sands, uranium, precious and base metals (Kossoff et al., 2014).

According to the Brazilian Institute for Applied Economic Research, between the years of 1996 to 2005 tailings generation in Brazil increased from 202 million tons to 290 million tons. The ore that contributed most to the generation of tailings in the period was iron. The quantities of tailings generated in the State of Minas Gerais State corresponded to 101 million tons and 123 million tons in 2008 and 2009, respectively (IPEA, 2012).

Regarding the future scenario of tailings generation, the Brazilian Institute for Applied Economic Research estimates that the annual quantity will almost double, from 348 million tons in 2010 to 684 million tons in 2030, being the iron then main waste-producing substance (IPEA, 2012).

The transport of several mining wastes to the disposal area occurs with high water content. The water that accompanies the tailings often contains dissolved salts, heavy metals and other chemical residues from the mineralogical process, and it can have significant environmental implications in the tailings dumping areas (IPEA, 2012).

The disposal of tailings in reservoirs created by dikes or dams is the most commonly method used in Brazil (IPEA, 2012) and around the world as well (Kossoff et al., 2014). The Dams Safety Report of the Brazilian National Water Agency (ANA, 2016b) indicates that by the year 2015 Brazil had 660 dams of mineral tailings and 286 dams of industrial waste. The State of Minas Gerais holds the largest number of tailings dams (315) and industrial waste retention dams (278). Figure 2.1 shows the location of the registered tailings dams in Brazil (DNPM, 2017).

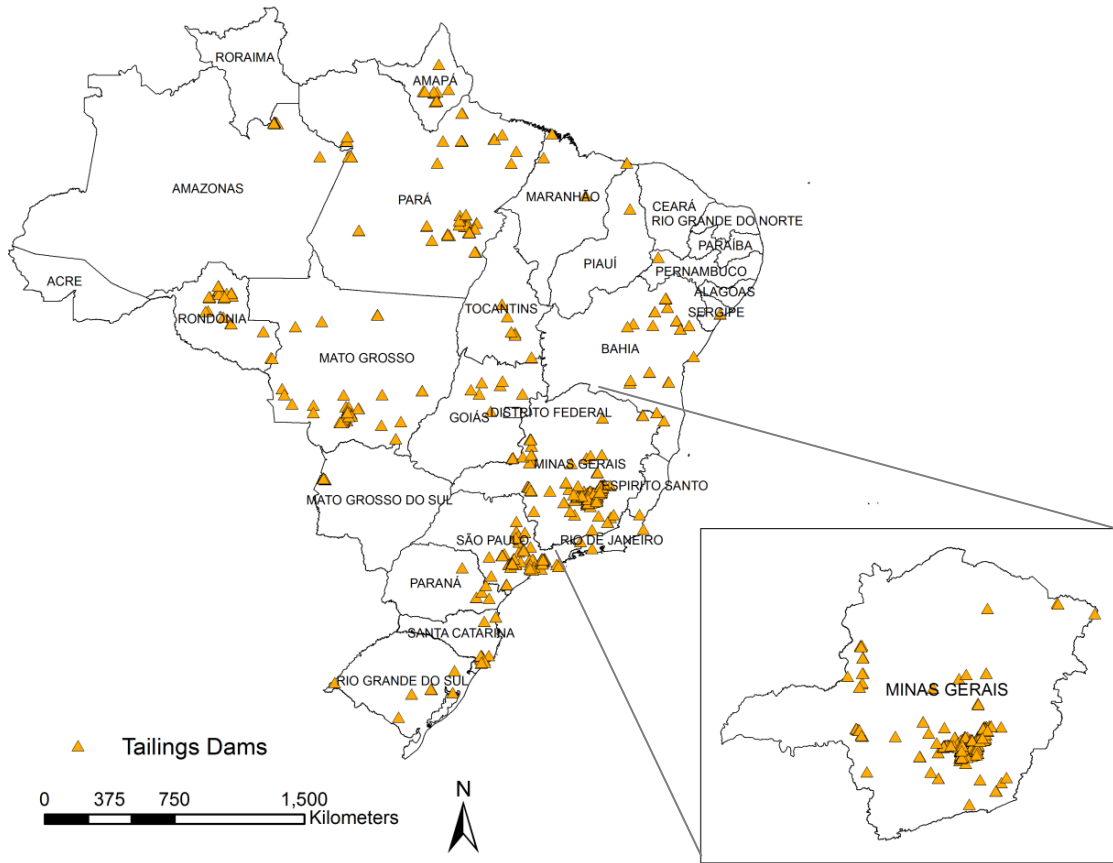


**Figure 2.1 – Location of the tailings dams in Brazil**

Accidents with tailings dams occur continually in Brazil with undesirable consequences for society, the environment and for the mining industry sector. There are also numerous cases not disclosed by the owners (CBDB, 2011). The state of Minas Gerais, where most of the tailings dam are located, is where most registered failures happened in Brazil. In addition, there are numerous cases where rupture does not occur, but there is spill of solids downstream with variable consequences (CBDB, 2011). Long rivers and well-drained basins (high drainage density) characterize the hydrography in Brazil, which are favorable factors for the propagation of pollutants for further downstream, as experienced by the country in past tailings dams failures.

Table 2.1 presents a compilation of tailings dam failures cases in Brazil reported by different authors (ICOLD, 2001; Melo, 2013; Rocha, 2016; Ávila, 2016; WISE, 2019).

**Table 2.1 – Tailings dams failures in Brazil**

Dam	Year	Dam Height (m)	Ore type	Storage Volume	Tailings Released	Tailings Travel (km)
Itabirito	1986	30	Iron	-	100,000 m <sup>3</sup>	12
Fernandinho	1986	40	Iron	-	350,000 m <sup>3</sup>	-
Pico Sao Luis	1986	20	-	-	-	10
Minera Serra Grande	1994	-	Gold	2.25 Mt	-	-
Rio Verde	2001	-	Iron	-	600,000 m <sup>3</sup>	8
Forquilha	2002	-	-	-	-	-
Cataguases	2003	-	-	-	1,400 Mm <sup>3</sup>	200
São Francisco	2006	34	Bauxite	3.7 Mm <sup>3</sup>	135,000 m <sup>3</sup>	-
São Francisco	2007	34	Bauxite	3.7 Mm <sup>3</sup>	3 Mm <sup>3</sup>	92
Herculano	2014	-	Iron	-	-	-
Fundão	2015	120	Iron ore	≈ 80 Mm <sup>3</sup>	32 Mm <sup>3</sup>	670
Brumadinho	2019	86	Iron ore	12 Mm <sup>3</sup>	-	-

Among the historic cases, it is remarkable the environmental tragedy due the Cataguases Dam collapse on 29 March of 2003. In this event about one billion and four hundred million liters of black lye, residue of cellulose production, contaminated the Paraíba do Sul River and nearby streams per 200 kilometers, reaching the interior of Rio de Janeiro State and leaving 600,000 people without water supply (Faria, 2015). Another noteworthy incident occurred in 2007, when the São Francisco tailings dam collapsed releasing 3 million of bauxite waste, flooding two towns downstream and dislodging 4,000 people (Faria, 2015; Rocha, 2016).

Despite the great damage caused by those accidents, none of them reached the proportion of the disaster in Mariana in 2015. Due the Fundão Dam height and its consequences, it is by far the worst environmental accident with tailings dam in Brazil, and one of the worst around the world (Marta-Almeida et al., 2016; Carmo et al., 2017). However, in terms of life loss the recent accident of Brumadinho Dam was the deadliest accident, resulting in 186 deaths, and up to date, 122 missing people (BBC, 2019) .

### 2.3 Modeling of Tailings Dam Failures

The modeling of the floods caused by tailings dam break is still a matter subject to research. Most of the numerical modeling for dam-break simulations have been developed for water storage dams (Rico et al., 2008). According to several authors the efforts to provide a reliable methodology to predict the effects caused by tailings dam collapse have been hindered by the lack of a worldwide database, scarcity of reliable historic data and incomplete documentation for known tailings dam failures (Davies, 2002; Rico et al., 2008; EPA, 2014).

Up to date, the literature indicates that the focus of the most of publications is to develop methodologies related only with the flood after failure. A widespread method is the application of the shallow water equation considering an additional friction term to take into account the resistance due the hyperconcentrated flow (Jeyapalan et al., 1983; Schamber & MacArthur, 1985; O'Brien et al., 1993; Jin & Fread, 1999; Rickenmann et al., 2006; Armanini et al., 2009; Kunkel, 2011; Lin & Li, 2012; Marsooli et al., 2013; Liu, 2018). Nevertheless, a popular approach currently applied in U.S. is still to model potential impacts downstream caused by the collapse of tailings dams assuming that the tailings behave like water, even though it is admittedly a conservative estimate (Clemente et al., 2013).

On the other hand, a simpler technique to estimate the flood hydrograph parameters after the dam break is the derivation of empirical relationships between dam parameters (as dam height and the reservoir volume for instance) and observed flood features (Lucia et al., 1981; Rico et al., 2008). Following this approach, Rico et al., (2008) present a study correlating several tailings dam parameters with the flood magnitude after the dam collapse. The authors attained a good agreement correlating the tailings storage volume and the spilled volume using data from 21 incidents around the world. Figure 2.2 shows the correlation obtained and the plot of the Fundão Dam data for comparison.

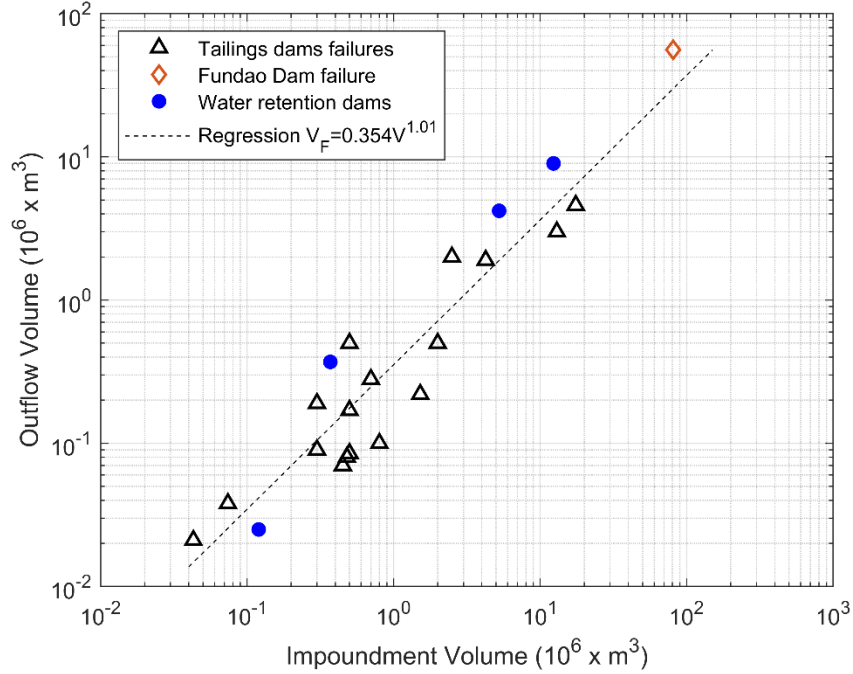


**Figure 2.2 – Relationship between Impoundment Volume and Outflow volume (Rico et al., 2008)**

According to the authors, the relationship between the waste outflow volume  $V_F$  (which includes tailings and water) and the impoundment volume  $V$  is equal to:

$$V_F = 0.354V^{1.01} \quad (2.1)$$

One can realize that in general approximately one-third of the impoundment volume (tailings and water) is released on the dam break. Another interesting relationship found by Rico et al., (2008) is the correlation between the resultant peak discharge and the dam factor, which is the product of the dam height  $H$  (m) and the impoundment volume  $V$  ( $10^6 \text{ m}^3$ ). An envelope estimate, which includes data from water retention, landslide and tailings dams is equal to:

$$Q_{max} = 325(HV)^{0.42} \quad (2.2)$$

The authors compared the data of several dam collapses (water retention and landslide dams) from Costa (1985) with the data of case of the Los Frailes Tailings Dam failure in Spain. They concluded that for a tailing dam failure a similar relationship between peak discharge and the dam factor is obtained taking into account only the spilled volume instead of the total volume. Figure 2.3 shows the plot of the data presented by the authors.

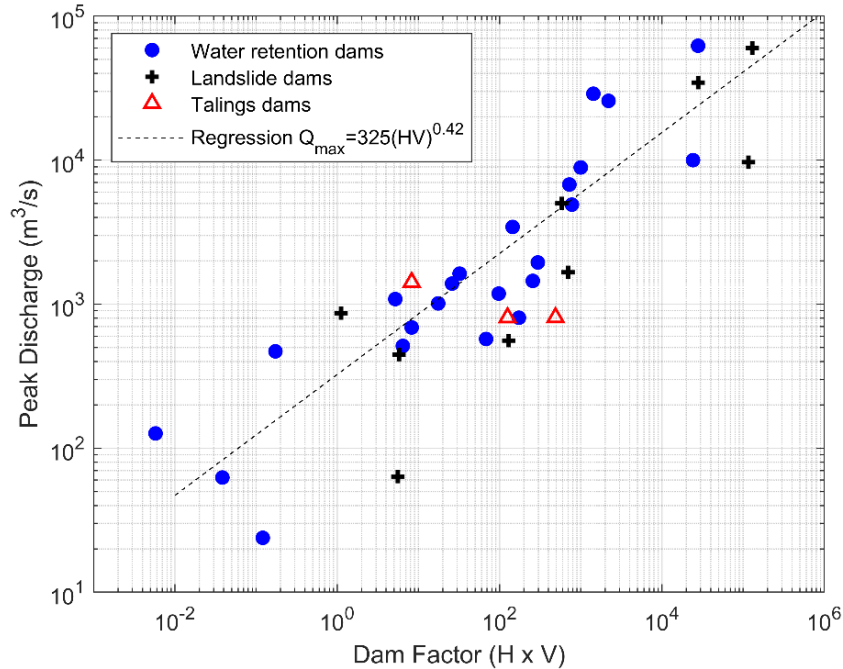


**Figure 2.3 – Relationship between peak discharge and dam factor (Rico et al., 2008)**

Rico et al., (2008) states that observed peak discharge from failure of tailings dams are extremely rare. There are register of only three cases: Buffalo Creek, McLauren Gold Mine (both in USA) and Los Frailes (Spain).

An examination in the literature also reveals that observed data of sediment transport in rivers after the tailings dam failure is a topic with scarcity of publications as well, even though it is remarkable that in some accidents the impact of the pollutant dispersion is severe as the flood. In addition, there are occurrences where the dam does not collapse, but there is spilling of mining waste in the water bodies. An example is the recent episode occurred on 5 August of 2015 in the Gold King Mine, located about 5 miles north of Silverton, Colorado, USA. In this event the spilling of 11,000 m<sup>3</sup> of acid mine water from mine workings resulted in the deposition of heavy metals along the Animas and San Juan Rivers, until the plume reached Lake Powell in Utah on August 14, 2015 (USBR, 2015).

## 2.4 Steady Flow in Channels

The water flow in open channels can be classified as steady or unsteady. Steady state of the flow refers to a constant condition over the time (Julien, 2018). Under the steady condition there is the gradually varied flow, which relates small variation of the flow depth with distance. Thus, considering the conservation of energy in a channel and assuming that the pressure is hydrostatic, the channel bed slope is small and there is no lateral inflow or outflow, Chaudhry (2007) demonstrates that:

$$\frac{\partial h}{\partial x} = \frac{S_o - S_f}{1 - Fr^2} \quad (2.3)$$

Where  $h$  is the flow depth,  $S_o$  is the bed slope,  $S_f$  is the energy line slope and  $Fr$  is the Froude number. The slope of the energy line can be calculated using the Manning's equation:

$$S_f = \left( \frac{Q \cdot n}{AR_h^{2/3}} \right)^2 \quad (2.4)$$

Where  $Q$  is the discharge,  $A$  is the cross-sectional flow area,  $n$  is the Manning's resistant coefficient and  $R_h$  is the hydraulic radius. Equation 2.3 describes the water surface elevation profile, what is generally referred as backwater curve. The solution of this equation can be achieved by the standard step approach, where the flow depth increment  $\Delta h$  can be calculated at fixed downstream distance increment  $\Delta x$  (Julien, 2010). Thus for a wide-rectangular channel ( $R_h \approx h$ ):

$$\Delta h \cong \Delta x S_o \left[ 1 - \left( \frac{h_n}{h_i} \right)^3 \right] / \left[ 1 - \left( \frac{h_c}{h_i} \right)^3 \right] \quad (2.5)$$

Where the normal depth  $h_n$  and the critical depth  $h_c$  are given by:

$$h_n = \left( \frac{q \cdot n}{S_o^{0.5}} \right)^{3/5} \quad (2.6)$$

$$h_c = \left( \frac{q^2}{g} \right)^{1/3} \quad (2.7)$$

Here  $q$  is the unit discharge. The above formulations are useful to determine the flow velocity and depth in natural channels, because these parameters are required for the calculation of advective transport and deposition of sediment or pollutants.

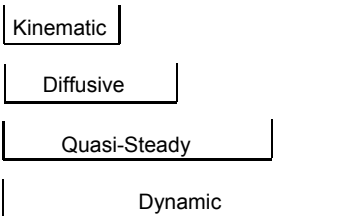
## 2.5 Unsteady Flow in Channels

### 2.5.1 Governing Equations

The mathematical treatment for unsteady flow in open channels involves the application of conservation of mass and conservation of momentum. Such equations are referred as the Saint Venant equations (Mahmood & Yevjevich, 1975; Cunge et al., 1980). Examination of the terms of the reduced form of the momentum equation elucidates the physical meaning of each term and the effect of neglecting some of them in order to ease the solution (Chow, 1988; Sturm, 2009; Julien, 2018).

$$S_f \cong S_o - \frac{\partial h}{\partial x} - \frac{U}{g} \frac{\partial U}{\partial x} - \frac{1}{g} \frac{\partial U}{\partial t} \quad (2.8)$$

(1)   (2)   (3)   (4)   (5)



The terms in Equation 2.8 represent slopes or gradients as described by Julien (2018): (1) is the friction slope of the EGL slope, (2) is the channel bed slope, (3) is the pressure gradient or downstream change in flow depth due to backwater, (4) is the velocity head gradient or downstream change in velocity head due to backwater and/or changes in channel width and (5) is the local-acceleration term. The full use of Equation 2.8 denotes the dynamic-wave equation approximation for the Saint Venant equation. Furthermore, Julien (2018), using equivalent terms, demonstrated that the Equation 2.8 can assume the following format:

$$S_f \cong S_o - [1 - (\beta - 1)^2 Fr^2] \frac{\partial h}{\partial x} \quad (2.9)$$

Where the term between the external brackets is the floodwave diffusivity, which depends on the value of  $\beta$  and the Froude number  $Fr$ . For instance, considering a turbulent flow with the constant Manning's  $n$  coefficient, the variable  $\beta$  results equal to 5/3. Consequently, the Froude number leads the signal of the floodwave diffusivity term, therefore for  $Fr < 1.5$  the floodwave diffusivity term is positive, otherwise for  $Fr > 1.5$  the term is negative. For rivers where the Froude number is low the floodwave diffusivity comes close to the unity (Julien, 2018).

The floodwave diffusivity plays a fundamental role in the modification of the floodwaves, which can be classified in three types:

- a) Dynamic wave when  $Fr > 1/(\beta - 1)$ ;
- b) Kinematic wave when  $Fr = 1/(\beta - 1)$ ;
- c) Diffusive wave when  $Fr < 1/(\beta - 1)$ .

Figure 2.4 illustrates the propagation of the dynamic, kinematic and diffusive waves. As an example, the dynamic wave can be applied on roll waves, which occurs in turbulent flows where there is a very steep smooth channel under supercritical flow. In this case, the floodwave amplification occurs, which means that the discharge peak downstream is greater than upstream. For the kinematic wave, the peak discharge remains the same as the floodwave moves forward. Finally, in most rivers where the flow is subcritical, the flood routing can be properly modeled by the diffusive wave approximation, where the floodwave attenuation takes place.

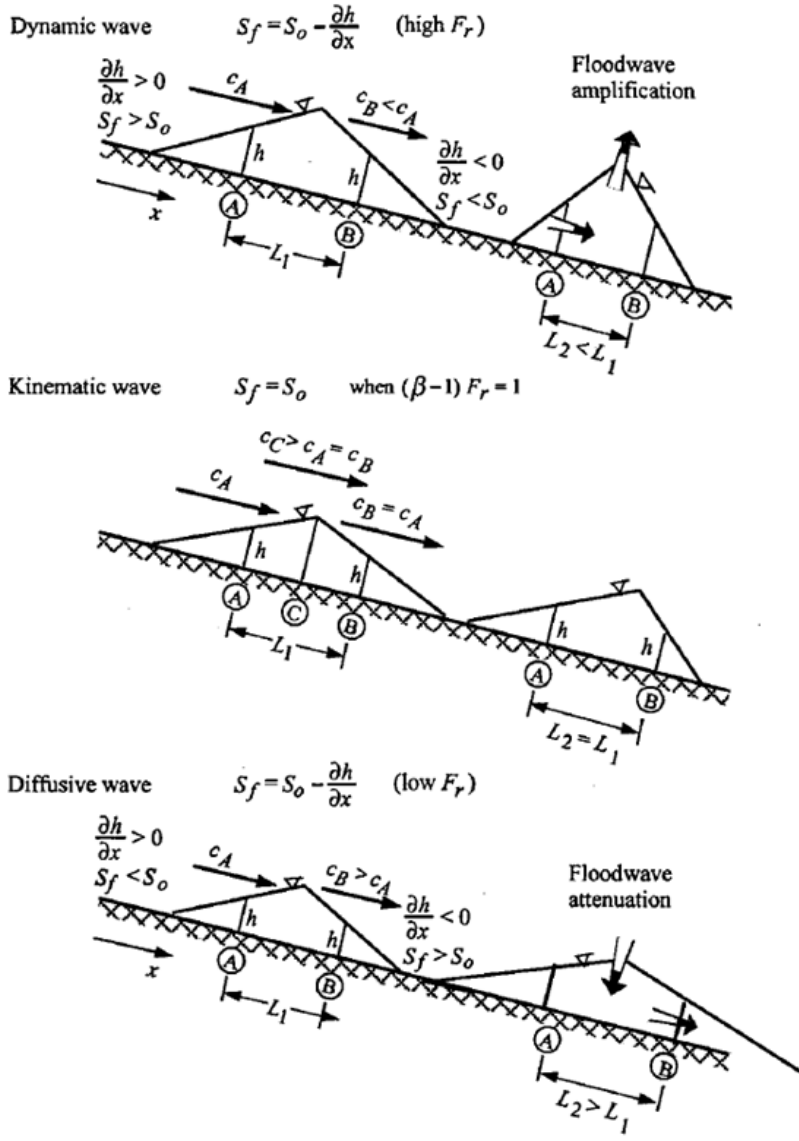


Figure 2.4 – Propagation of dynamic, kinematic and diffusive waves (Julien, 2018)

2.5.2 Full Dynamic Wave

In rivers, the full dynamic-wave propagation is calculated by the resolution of the conservation of momentum and the continuity equation, as given below:

$$\frac{\partial Q}{\partial t} + \frac{\partial}{\partial x} \left( \frac{Q^2}{A} \right) + gA \frac{\partial h}{\partial x} + gA(S_f - S_o) = 0 \tag{2.10}$$

$$\frac{\partial Q}{\partial x} + \frac{\partial A}{\partial t} = 0 \tag{2.11}$$

According to Cunge et al. (1980) the Saint-Venant equations assume that the river is sufficiently straight and uniform, so the flow can be represented by a one-dimensional model. Furthermore, the average channel bed slope is small, thus the cosine of the angle it makes with the horizontal may be replaced by unity. The velocity is considered uniform over the cross section and the water level across the section is horizontal. In addition, the streamline curvature is small and vertical accelerations are negligible, therefore the pressure is hydrostatic. Lastly, the effects of boundary friction and turbulence can be accounted through resistance laws. Due to its complexity, the solution of Equations 2.10 and 2.11 requires the application of numerical schemes. However, the suppression of some terms of the Saint Venant equations can lead to simpler format with satisfactory accuracy, as presented in the next section.

### 2.5.3 Diffusive Wave Approximation

The diffusive wave approximation describes the behavior of the floodwave propagation in most rivers using a simplified version of the Saint-Venant equations. This approach considers that velocity head gradient and the local-acceleration terms are negligible when compared with the bed slope and the pressure gradient. Thus, the simplified momentum equation reduces to:

$$S_f = S_o - \frac{\partial h}{\partial x} \quad (2.12)$$

Considering the flow resistance and the continuity, Equation 2.12 can assume the advection-dispersion format (the derivation of this expression is presented on the Appendix B):

$$\frac{\partial Q}{\partial t} + C_e \frac{\partial Q}{\partial x} - D \frac{\partial^2 Q}{\partial x^2} = 0 \quad (2.13)$$

Equation 2.13 is the linear diffusive wave model in the form of the advection-dispersion transport equation, in which  $C_e$  is the floodwave celerity (wave propagation speed) and  $D$  is the coefficient of hydraulic diffusivity (Hayami, 1951; Chanson, 2004; Cappelaere, 1997; Yang et al., 2016; Battjes & Labeur, 2017). The floodwave celerity can be expressed as function of flow velocity as (Julien, 2018):

$$C_e = \beta U \quad (2.14)$$

Where  $U$  is the mean flow velocity and  $\beta$  is a parameter dependent on the coefficient of resistant adopted and the channel shape. One should make distinction between the floodwave celerity  $C_e$  and the solitary wave celerity  $c$ , which describes the propagation of a small perturbation in a frictionless flow. This last one defines the Froude number  $Fr = U/c$ .

The relationship between the floodwave celerity and the mean flow velocity presents different values according to the format of the channel cross section and the coefficient of roughness chosen (Manning, Darcy Welsbach or Chezy). For instance, for a wide rectangular channel considering the Manning's equation, the floodwave celerity assumes the following format given in Equation 2.15 (Singh, 1996):

$$C_e = \frac{5}{3} U \quad (2.15)$$

Independently of the adopted roughness coefficient the floodwave celerity is always faster than the flow velocity. Therefore, according to the theoretical perspective the suspended sediment (carried by the flow velocity) and the floodwave propagation are expected to travel at the different velocities. Alternatively, the floodwave celerity can also be estimate by the Kleitz-Seddon law, first used for the Mississippi River (Chanson, 2004; Julien, 2018).

$$C_e = \frac{\partial Q}{\partial A} \quad (2.16)$$

The second parameter required in Equation 2.13 is the coefficient of hydraulic diffusivity  $D$ , which is responsible for the floodwave attenuation. This coefficient considers the energy slope equal to the bed slope and it is commonly presented in literature as (Cunge et al., 1980; Singh, 1996; Roberson et al., 1998; Jain, 2001; Sturm, 2009; Yang et al., 2016):

$$D = \frac{K}{2W\sqrt{S_f}} = \frac{Q}{2WS_o} \quad (2.17)$$

Where  $K$  is the channel conveyance coefficient ( $K = Q/\sqrt{S_o}$ ) and  $Q$  is a reference discharge, because the coefficient  $D$  remains constant along the channel in the linear simulation. Even though this is an expression easily found on literature, the discharge value is not clearly defined and values for the hydraulic diffusivity  $D$  for manmade or natural channels are rarely found.

#### 2.5.4 Numerical Methods

The solution of the Saint-Venant equations can be addressed by different numerical approaches as the method of characteristics, finite difference method, finite volume method and the finite element method (Szymkiewicz, 2010; Wu et al., 2011). However, due its simplicity and the one-dimensional character of most open channel flow problems, the use of the finite difference methods predominates. The concept of the finite difference method is to replace the derivatives in the ordinary or partial difference equations by finite difference formulas derived from the Taylor series expansions (Moin, 2010). The accuracy of a numerical scheme is related with the reduction in the error with the decreasing of the spatial mesh size and time step (Abbott & Basco, 1990; Wu, 2007; Moin, 2010).

The literature presents several finite difference schemes for the solution of the Saint-Venant equations as the implicit schemes of Preissmann Scheme and Crank Nicolson and the QUICKEST explicit scheme (Mahmood & Yevjevich, 1975; Leonard, 1979; Cunge et al., 1980; Abbott & Basco, 1990; Akan, 2006; Chaudhry, 2007). Alternatively, there are simplified methods based on the continuity equation, often called hydrologic routing or lumped models. Among these methods there is the Muskingum Cunge and the Modified Puls (Chow, 1988; Chaudhry, 2007; McCuen, 2016). Table 2.2 summarizes the main characteristics of the above-mentioned methods including the methods used in the well-known software HEC-RAS (USACE, 2016). The numerical solution of these methods is presented in Appendix C.

**Table 2.2 – Summary of characteristics of widespread methods to calculate flood routing (Leonard, 1979; Abbott & Basco, 1990; Chapra, 2008; Price, 2009; Moin, 2010; Fenton, 2011; McCuen, 2016; USACE, 2016; Julien, 2018)**

Method	Features
Preissmann	Solves the momentum (full dynamic-wave) and the continuity equation. It is implicit, first order accurate, unconditionally stable and presents numerical dissipation (numerical diffusion) for $0.5 \leq \theta \leq 1$ . Can result in unphysical smoothing when sharp gradients occur on the solution.
Crank Nicolson	Solves the simplified form of momentum equation in the format of advection-dispersion equation, neglecting the acceleration terms (diffusive-wave). The scheme is implicit, second order accurate, non-diffusive and unconditionally stable. It can present oscillations on the solution depending on the mesh size. The hydraulic diffusivity coefficient must be known in advance and an additional method to calculate the continuity equation is required.
QUICKEST	Solves the simplified form of momentum equation in the format of advection-dispersion equation, neglecting the acceleration terms (diffusive-wave). The scheme is explicit, third order accurate, non-diffusive and conditionally stable (time step restrictive). The hydraulic diffusivity coefficient must be known in advance and an additional method to calculate the continuity equation is required.
Modified Puls	Solves the continuity equation only. The method is explicit, first order accurate and unconditionally stable. Requires the definition of a storage-outflow discharge function.
Muskingum-Cunge	Solves the continuity equation, however takes into account the diffusive-wave approximation in its derivation. It is explicit, first order accurate and unconditionally stable. It loses accuracy as the river bed slope become milder. Requires an additional method or function to calculate the water level.
HEC-RAS	Solves the one-dimensional unsteady flow using two methods: full dynamic-wave routing using the box scheme [aka Preissmann (Chanson, 2004)] or the Modified Puls routing.

The quantitative evaluation of the results provided by the numerical schemes and the observed hydrographs can be made by the relative percent difference (RPD) applied on the peak discharge, the Root Mean Square Error (RMSE):

$$RMSE = \left[ \sum_{i=1}^N (Q_{oi} - Q_{ci})^2 / N \right]^{1/2} \quad (2.18)$$

And by the Mean Absolute Percent Error (MAPE):

$$MAPE = \frac{1}{N} \left[ \sum_{i=1}^N \text{abs}(Q_{oi} - Q_{ci}) / Q_{oi} \right] \quad (2.19)$$

Where  $Q_{oi}$  and  $Q_{ci}$  are the observed and the calculated discharge respectively and  $N$  is the number of observations.

## 2.6 Flood Routing in Reservoirs

The Level Pool Routing is a common approach to calculate the outflow hydrograph in a reservoir given its hydrograph and the storage-outflow characteristics (Chow, 1988). Initially, the continuity equation can be written as the storage differential equation:

$$\frac{dS}{dt} = I(t) - O(t) \quad (2.20)$$

Where  $S$  is the reservoir storage,  $I(t)$  is the inflow and  $O(t)$  is the outflow (all the variables are functions of the time). The solution of Equation 2.20 is given by the integration and rearrangement of its terms in order to place all unknown variable on the left-hand side of the equation. Thus, the storage-indication routing equation becomes Equation 2.21 (Chow, 1988):

$$\frac{2S(t_{i+1})}{\Delta t} + O(t_{i+1}) = [I(t_{i+1}) + I(t_i)] + \left[ \frac{2S(t_i)}{\Delta t} - O(t_i) \right] \quad (2.21)$$

The level pool routing approach assumes that the storage and the outflow are function of the water level elevation only. In general, the storage-elevation curve is a common data of reservoirs and the outflow-elevation relationship depends on the type of hydraulic structure (e.g. spillways, etc.) and its operation. The solution for the level pool routing is given by the development of a function  $2S/\Delta t + O = f(O)$  and then proceeding with the routing of the inflow hydrograph. The outflow is obtained applying this procedure for every time step sequentially (Ramirez, 2015).

## 2.7 Sediment Transport in Rivers

### 2.7.1 Classification

According to Julien (2010) the total sediment load in a stream is divided in: type of movement (bed load and suspended load), method of measurement (measured and unmeasured load) and the source of sediment (bed material load or washed load).

In order to apply a proper method to evaluate the sediment transport, the first step is to identify the primary mode of sediment transport. Table 2.3 presents the modes of sediment transport as function of the Rouse number, shear and fall velocities after Julien (2010):

**Table 2.3 – Mode of sediment transport as function of shear and fall velocities**

$Ro$	$u_*/\omega$	Mode of sediment transport
$>12.5$	$<0.2$	no motion
$\approx 12.5$	$\approx 0.2$	incipient motion
12.5-5	0.2-0.5	bedload
5-1.25	0.5-2	mixed load
1.25-0.5	2-5	suspension
$<0.5$	$>5$	suspension

The shear velocity is:

$$u_* = \sqrt{gR_h S_f} \quad (2.22)$$

Where  $g$  is the gravitational acceleration. Additionally, the fall velocity is calculated as:

$$\omega = \frac{8v_m}{d_s} ((1 + 0.0139d_*^3)^{0.5} - 1) \quad (2.23)$$

Where  $v_m$  is the kinematic viscosity of a mixture,  $d_s$  is the particle diameter and  $d_*$  is the dimensionless particle diameter, given by:

$$d_* = d_s \left[ \frac{(G-1)g}{v_m^2} \right]^{1/3} \quad (2.24)$$

The specific gravity  $G$  is the ratio between the specific weight of a solid particle and the specific weight of fluid at a standard reference temperature. Considering the water at 4°C as reference, the specific gravity of quartz particle is equal to 2.65 (Julien, 2010). Finally, the Rouse number  $Ro$  is given by:

$$Ro = \frac{\omega}{\kappa u_*} \quad (2.25)$$

Where  $\kappa$  is the von Karman constant, approximately equal to  $\kappa \cong 0.4$ .

Single inputs of sediment excess can be referred in literature as sediment “pulse” (Gran & Czuba, 2017). For instance, these inputs can be the result of a landslide, however it can be manmade generated, as a tailings dam spill or collapse. Some authors described the downstream migration of a sediment pulse, including hydraulic mining debris, as “sediment waves” due to the wavelike movement of sediment during the transport (Gilbert, 1917; Reid et al., 1985; Iseya & Ikeda, 1987; Cui & Parker, 2005). Moreover, for the case of mining sediment migration downstream, as the case of Kwareong River in Papua New Guinea, it was observed occurrence of substantial dispersion (Pickup et al., 1983). Thus, next section presents the governing equations for suspended sediment transport for further modeling.

### 2.7.2 Suspended Load

The transport of the suspended load occurs as the hydraulic forces promote the suspension of the sediment finer particles and it is held in suspension by the turbulent velocity fluctuations, keeping the particles out of recurrent bed contact (Julien, 2010). The governing equations of this type of transport is obtained through the application of conservation of sediment mass applied into a small cubic control volume, as presented by Julien (2010):

$$\frac{\partial C}{\partial t} + \frac{\partial q_{tx}}{\partial x} + \frac{\partial q_{ty}}{\partial y} + \frac{\partial q_{tz}}{\partial z} = \dot{C} \quad (2.26)$$

Where  $C$  is the volume-average sediment concentration inside the infinitesimal control volume,  $q_{tx}, q_{ty}, q_{tz}$  are the sediment fluxes per unit area through the faces of the control volume and  $\dot{C}$  is the rate of sediment reaction per unit volume.

There are four main types of mass fluxes per unit area across the faces of the control volume, which are: advective, diffusive, mixing and dispersive fluxes (Julien, 2010). The next expression exemplifies the sediment flux in the  $x$  direction:

$$\hat{q}_{tx} = v_x C - (d + \varepsilon_x) \frac{\partial C}{\partial x} \quad (2.27)$$

The advective flux refers to the transport of sediment conveyed by the flow velocity. Thus, the rate of mass transport per unit area carried by advection is obtained by the product of sediment concentration and the velocity component in the  $x, y$  and  $z$  directions. The variable  $d$  is the molecular diffusion coefficient and it describes the spreading of sediment particles by random molecular motion. Finally, the turbulent mixing coefficient  $\varepsilon$  describes the process of turbulent diffusion (Julien, 2010).

### 2.7.3 One-Dimensional Advection-Dispersion Equation for Sediment Transport

The substitution of Equation 2.27 into Equation 2.26 leads to the general relationship of the conservation of sediment mass for incompressible dilute suspension subject to diffusion, mixing, dispersion and advection. Considering the sediment transport only in  $x$  direction the general equation becomes:

$$\frac{\partial C}{\partial t} + v_x \frac{\partial C}{\partial x} = \dot{C} + (d + \varepsilon_x) \frac{\partial^2 C}{\partial x^2} \quad (2.28)$$

Equation 2.28 is called advection-dispersion, advection-diffusion or the diffusion-dispersion equation and it is applied on the evaluation of transport of suspended load and contaminant transport in open channels (Fischer et al., 1979; Rutherford, 1994; Chanson, 2004; Chapra, 2008; Julien, 2010).

In laminar flows, the turbulent mixing and dispersive coefficients disappear ( $\varepsilon = 0$ ). However, in turbulent flows the molecular diffusion is negligible compared to the turbulent mixing and dispersion coefficient ( $d \ll \varepsilon$ ). For practical purposes, as the application of the accidental spill of a pollutant in a river, the one-dimensional advection-dispersion assumes the following format (Chanson, 2004; Julien, 2018):

$$\frac{\partial C}{\partial t} + U \frac{\partial C}{\partial x} = K_d \frac{\partial^2 C}{\partial x^2} - kC \quad (2.29)$$

Where  $K_d$  is the longitudinal dispersion coefficient in natural streams and  $k$  is the settling rate given by Equation 2.30:

$$k = \frac{\omega_i}{h} \quad (2.30)$$

Where  $\omega_i$  is the fall velocity for the sediment fraction  $i$ .

#### 2.7.4 Solutions for the One-Dimensional Advection-Dispersion Equation

For the particular case where the spill concentration is held constant for a finite time interval, the analytical solution for Equation 2.29 can be obtained by following expression (Chapra, 2008):

$$C(x, t) = \frac{C_0}{2} \left\{ \begin{aligned} & e^{\frac{Ux}{2K_d}(1-\Gamma)} \left[ \operatorname{erfc} \left( \frac{x - Ut\Gamma}{2\sqrt{K_d t}} \right) - \operatorname{erfc} \left( \frac{x - U(t - \tau)\Gamma}{2\sqrt{K_d(t - \tau)}} \right) \right] \\ & + e^{\frac{Ux}{2K_d}(1+\Gamma)} \left[ \operatorname{erfc} \left( \frac{x + Ut\Gamma}{2\sqrt{K_d t}} \right) - \operatorname{erfc} \left( \frac{x + U(t - \tau)\Gamma}{2\sqrt{K_d(t - \tau)}} \right) \right] \end{aligned} \right\} \quad (2.31)$$

Where  $C_0$  is the initial concentration and  $\tau$  is the spilling duration time, furthermore:

$$\Gamma = \sqrt{1 + 4\eta} \rightarrow \eta = \frac{kK_d}{U^2} \quad (2.32)$$

The complementary error function is evaluated from the following integral:

$$\operatorname{erfc}(b) = 1 - \frac{2}{\sqrt{\pi}} \int_0^b e^{-\zeta^2} d\zeta \quad (2.33)$$

Where  $\zeta$  is a dummy variable. The error function is available in different sources as: standard software's libraries (International Math and Statistics Library (IMSL)), Numerical Recipes (Press et al., 2007) and as function on some software package as the Microsoft Excel for instance (Chapra, 2008).

However, this analytical solution has a numerical restriction due the second term in the right-hand side of the equation, because the exponential function can tend to infinity blowing up the solution for large river reaches. Thus, the maximum length  $L_{max}$  where Equation 2.31 is applicable is given by:

$$L_{max} \leq 700 \frac{K_d}{U} \quad (2.34)$$

An alternative way to solve the one-dimensional advection-dispersion equation is by the numerical approach, using Crank Nicolson finite difference scheme (Chapra, 2008; Szymkiewicz, 2010). However, this scheme must consider the settling rate (differently from the algorithm applied to floodwave propagation). Details about this numerical scheme are given in Appendix D.

### 2.7.5 Computation of the Longitudinal Dispersion Coefficient in Rivers

In order to solve practical problems involving the one-dimensional advection-dispersion equation in rivers several researchers have developed empirical equations to estimate the longitudinal dispersion coefficient  $K_d$  as functions of hydraulic and river-geometry parameters (Kashefipour & Falconer, 2002). As pointed by Noori et al., (2017) most of equations follow the format:

$$\frac{K_d}{hu_*} = a \left( \frac{U}{u_*} \right)^b \left( \frac{W}{h} \right)^c \quad (2.35)$$

Table 2.4 presents a compilation of the most commonly used empirical equations for the prediction of longitudinal dispersion coefficient.

**Table 2.4 – Empirical equations for the estimative of the longitudinal dispersion coefficient**

ID	Empirical equation	Author
1	$K_d = 5.93hu_*$	(Elder, 1959)
2	$K_d = 0.011U^2W^2/hu_*$	(Fischer et al., 1979)
3	$K_d = 0.18(U/u_*)^{0.5}(W/h)^2hu_*$	(Liu, 1977)
4	$K_d = 0.6(W/h)^2 hu_*$	(Koussis & Rodríguez, 1998)
5	$K_d = 2.0(W/h)^{1.5} hu_*$	(Iwasa & Aya, 1991)
6	$K_d = 0.2(U/u_*)^{1.2}(W/h)^{1.3}hu_*$	(Li et al., 1998)
7	$K_d = 5.92(U/u_*)^{1.43}(W/h)^{0.62}hu_*$	(Seo & Cheong, 1998)
8	$K_d = 10.612(U/u_*)hU$	(Kashefipour & Falconer, 2002)
9	$K_d = [7.428 + 1.775(W/h)^{0.62}(U/u_*)^{0.572}](U/u_*)hU$	(Kashefipour & Falconer, 2002)
10	$K_d = 250hu_*$	(Julien, 2010)
11	$K_d = 5.4(U/u_*)^{0.13}(W/h)^{0.7}hU$	(Zeng & Huai, 2014)

The discrepancy ratio  $DR$  is a common way to evaluate the precision of the empirical equations (Kashefipour & Falconer, 2002; Tayfur & Singh, 2005; Zeng & Huai, 2014). This ratio is given by:

$$DR = \log \left( \frac{K_{dp}}{K_{dm}} \right) \quad (2.36)$$

Where  $K_{dp}$  is the predicted longitudinal dispersion coefficient and  $K_{dm}$  is the measured one. Therefore if  $DR = 0$ , then it is an exact calculation, otherwise it can be overestimated ( $DR > 0$  or  $K_{dp} > K_{dm}$ ) or an underestimation ( $DR < 0$  or  $K_{dp} < K_{dm}$ ). To define a total discrepancy ratio for a set of experiments  $N$ , one can use the following expression (Zeng & Huai, 2014):

$$DR_s = \frac{1}{N} \sum_{i=1}^N \left[ \log \left( \frac{K_{dpt}}{K_{dmi}} \right) \right] \quad (2.37)$$

Thus, the mean of the absolute error (ME) can be applied (Kashefipour & Falconer, 2002):

$$ME = \frac{1}{N} \sum_{i=1}^N |DR_i| \quad (2.38)$$

Similarly, the root mean square error (RMSE) can be used, which is written as (Kashefipour & Falconer, 2002):

$$RMSE = \frac{1}{N} \sqrt{\sum_{i=1}^N (DR_i)^2} \quad (2.39)$$

### 2.7.6 Changes in River Bed Elevation

Application of the sediment continuity relationship in vertical direction for a determined size fraction  $i$  can predict changes in the bed surface elevation. This effect is described by the Exner expression:

$$\frac{\partial z_j}{\partial t} = - \frac{T_{Ei}}{(1 - p_o)} \frac{\partial q_{sj}}{\partial x} \quad (2.40)$$

Where  $z_j$  is the bed surface elevation,  $p_o$  is the porosity and  $q_{sj}$  is the unit sediment discharge. For suspended load,  $q_{sj}$  is given by:

$$q_{sj} = \frac{10^{-6} C_{mg/l} q_j}{G} \quad (2.41)$$

Where  $C_{mg/l}$  is the sediment concentration in mg/l and  $q_j$  is the unit discharge. In addition,  $T_{Ei} \cong 1$ , since the grid spacing is sufficiently long (Julien, 2018). The numerical solution for the Exner equation can be achieved using the forward difference in time and central difference scheme in space (Wu, 2007).

$$z_j^{n+1} = z_j^n - \frac{1}{2(1-p_o)} \frac{\Delta t}{\Delta x} (q_{sj+1}^n - q_{sj-1}^n) \quad (2.42)$$

## 2.8 Suspended Sediment Transport in Reservoirs

Decay of sediment concentration due to settling in a reservoir is given by (Julien, 2010):

$$C_i = C_{oi} e^{-\frac{X\omega_i}{hU}} \quad (2.43)$$

Where  $C_i$  and  $C_{oi}$  are the downstream and the upstream concentration respectively and  $X$  is a horizontal distance. According to Julien (2010), Equation 2.43 presents good agreement with measurements carried out by Çeçen (1969) and the relationship of Borland (Shen, 1971). Considering the time elapsed for the suspended sediment cross the reservoir  $t = X/U$  and the settling rate  $k$  [Equation 2.30], Equation 2.43 becomes:

$$C_i = C_{oi} e^{-kt} \quad (2.44)$$

The percentage of the sediment fraction  $i$  that deposits in a reservoir defines the trap efficiency  $T_{Ei}$ , which can be written as function of t reservoir area  $A_R$  and discharge  $Q$ :

$$T_{Ei} = 1 - e^{-\frac{A_R \omega_i}{Q}} \quad (2.45)$$

Equation 2.45 can be applied in different sediment fractions for a given particle size distribution. Thus, one can obtain the total amount of sediment deposited in a reservoir applying the trap efficiency by particle size and then summing the retained volume referent to each sediment fraction (Kim, 2016):

$$\forall_{trap} = \sum_i \Delta p_i T_{Ei} Q_{si} \quad (2.46)$$

Where  $\forall_{trap}$  is the sediment volume trapped in the reservoir,  $\Delta p_i$  is the sediment fraction and  $Q_{si}$  is the sediment discharge for a fraction  $i$ .

## 2.9 Hyperconcentrated Flows

The flood resultant from a tailings dam break is a subject bounded to the hyperconcentration analysis. Hyperconcentration is related to flows with a heavy sediment load in which the presence of fine sediment can affect the fluid properties and the bed material transport (O'Brien & Julien, 1985; Julien, 2010). Furthermore, the hyperconcentration classification is given by the volumetric sediment concentration  $C_v$  of the mixture, which is equal to:

$$C_v = \frac{\forall_s}{\forall_t} \quad (2.47)$$

Where  $\forall_s$  is the volume of solids and  $\forall_t$  is the total volume. In general, the hyperconcentration refers to flows where the volumetric sediment concentration ranges from 5% to 60% (Julien, 2010). Therefore, according to the experiments carried out by O'Brien and Julien (1985), the high sediment laden flow can be classified as: Landslides ( $0.5 < C_v < 0.9$ ), Mud Flows ( $0.45 < C_v < 0.5$ ), Mud Flood ( $0.2 < C_v < 0.45$ ) and Water Flood ( $C_v < 0.2$ ). Flow characteristics evolve from failure by block sliding (Landslide) to plastic deformation (Mud Flows) then appearance of some turbulence (Mud Flood) until water flood, where water flow and sediment transport occurs distinctly (O'Brien & Julien, 1985).

### 3. DATA COLLECTION

#### 3.1 The Doce River Basin

The Fundão Dam is located in the Doce River basin, in the southeast region of Brazil. This basin has a drainage area of 82,600 km<sup>2</sup>, with most of its area located in the State of Minas Gerais (86%), while the remaining area is in the State of Espírito Santo. The main stream is the Doce River, which originates from the confluence of tributaries Carmo River and Piranga River, extends over 570 km and flows to the Atlantic Ocean. Figure 3.1 shows the Doce River basin.



Figure 3.1 – The Doce River basin

There are twelve hydropower plants in this basin, with four located in the Doce River. The Doce River reservoirs characteristics are given in Table 3.1 (Barbosa, 2010; Cortez, 2013; Consórcio UHE Baguari, 2018; Consórcio Candonga, 2018)

**Table 3.1 – Doce River reservoir data**

Name	Reservoir Area (km <sup>2</sup> )	Volume (Mm <sup>3</sup> )	Extension (km)
Candonga	2.86	42.2	8.5
Baguari	16.0	38.1	22
Aimorés	31.3	249.2	32
Mascarenhas	4.1	23.9	10

Figure 3.2 shows the aerial images of the Doce River hydropower reservoirs after the Fundão Dam collapse.



**Figure 3.2 – The Doce River Hydropower reservoirs: a) Candonga Dam; b) Baguari Dam; c) Aimorés Dam and d) Mascarenhas Dam (Pimentel, 2016; Roberto, 2016; Mesquita, 2015; UOL, 2015)**

From the pictures shown in Figure 3.2 it is noticeable the occurrence of density currents in the Aimorés Dam reservoir after the arrival of the mud (Figure 3.2-c). The difference of color of the reservoir and the flow passing through the spillway can be justified by movement of the sediment through the reservoir caused by the density difference between the sediment-laden water (reservoir bottom) from the clear water (on reservoir surface).

In addition to electric power generation, the water resources of the Doce River basin play a fundamental role in the local economy, because they provide the necessary water for domestic, agricultural and industrial uses, among others. There are 209 towns within Doce River basin, which corresponds to a population of approximately 3.6 million of inhabitants (IBGE, 2010) as illustrated in Figure 3.3.

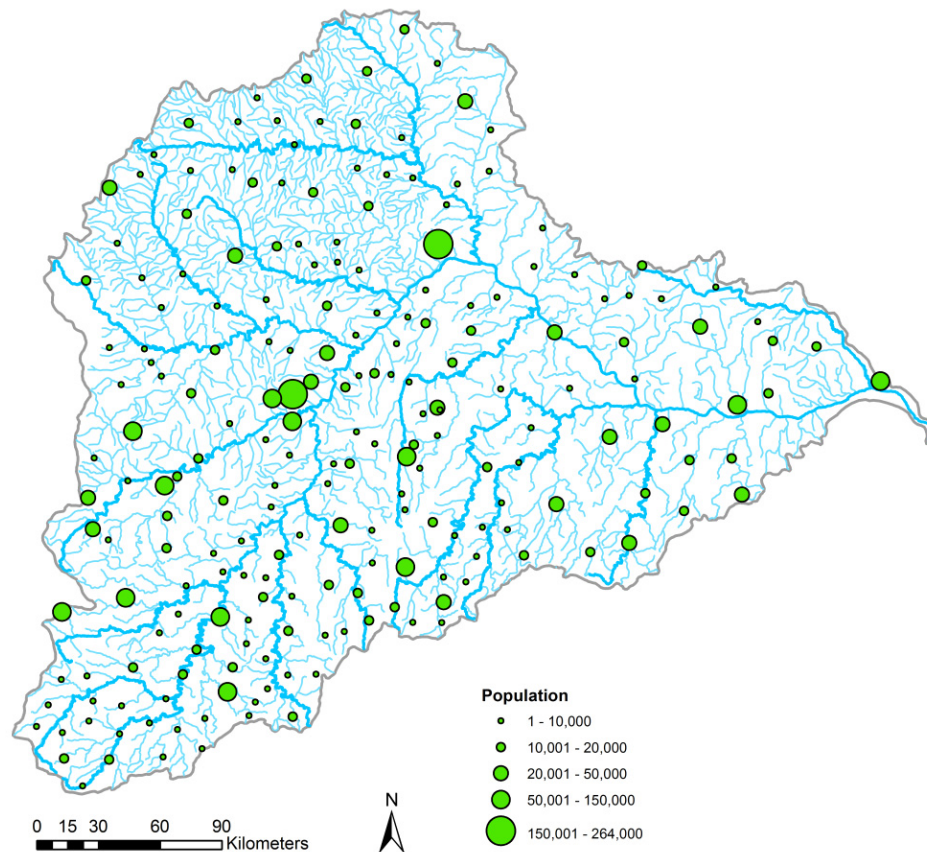


**Figure 3.3 – Population in the Doce River basin**

### 3.2 The Fundão Dam

The Fundão Dam was a tailings dam 120 m high designed to store tailings from the local iron mining activities, located in the town of Mariana, State of Minas Gerais. The tailings resultant of the production of iron ore are: sand tailings, composed of both sand and silt size particles and slimes, which are fine grained and clayey (Morgenstern et al., 2016). Sandy and slime tailings were stored physically separated in two specific reservoirs, with sand dumped behind the Dike 1 and slimes behind the Dike 2.

The project considered that Dike 1 would be an earth fill structure with the crest at elevation 830 (masl) with a later upstream heightening with sand tailings at the elevation 920 (masl), resulting in a total high of 120 m (Rezende, 2013; Morgenstern et al., 2016). This dam started to operate in April 2010 (Rezende, 2013; Morgenstern et al., 2016). Figure 3.4 shows an aerial view of the Fundão Dam (before the collapse) with the location of the Dike 1 and the approximate position of Dike 2 (dashed line), which is not visible since it is covered by tailings (Morgenstern et al., 2016). Figure 3.5 presents the Fundão Dam profile adapted from Rezende (2013).



Figure 3.4 – The Fundão Dam (Morgenstern et al, 2016)

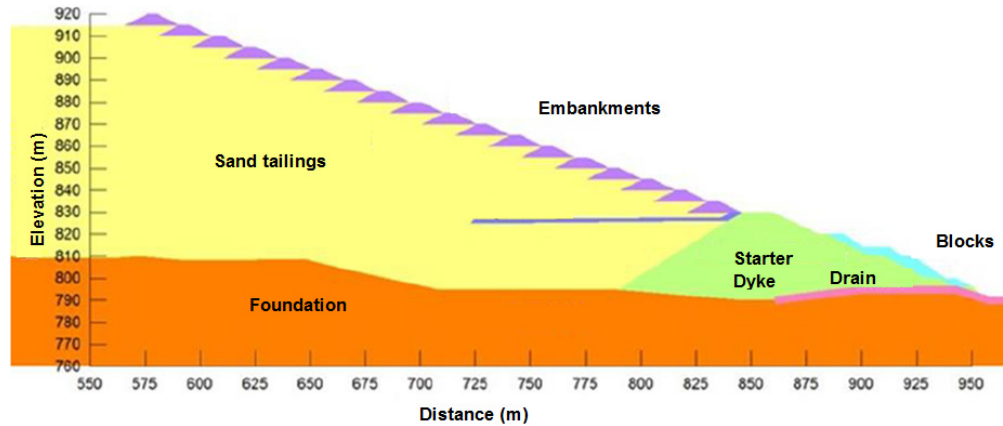


**Figure 3.5 – The Fundão Dam profile (Rezende, 2013)**

On 5 November of 2015 the Fundão Dam collapsed. According to Morgenstern et al., (2016), the accident occurred at 3:45 PM (local time) being caused by liquefaction and flow sliding of the sand stored in the reservoir. The dam crest was approximately in the elevation 900 (masl) in the days preceding the failure, which corresponds to a stored volume of approximately 77 Mm<sup>3</sup> (Machado, 2017).

The authors described the employees report moments before the accident: *“At 3:45 PM shouts came over radio that the dam was collapsing. A cloud of dust had formed over the left abutment, and those closest to the area designated the “setback” could see cracks forming at the recently constructed drainage blanket. The slope above them was beginning to undulate “like a wave” as if it were “melting,” bringing the dam crest down after it. The tailings that had been solid ground just minutes before transformed into a roiling river...”*. Figure 3.6 shows the dam and the reservoir before and after the collapse.



**Figure 3.6 – Fundão Dam before (a) and after failure (b) (Morgenstern et al., 2016)**

The Fundão Dam failure released 32 million cubic meters of tailings, not considering water (IBAMA, 2016). After the collapse, the floodwave overtopped the Santarém tailings dam, located immediately downstream of the Fundão Dam. The town of Bento Rodrigues with 600 inhabitants located about 5 km downstream was covered by the mud and debris, resulting in 19 deaths (ANA, 2016a). Machado (2017), based on testimony of eye-witness, reports that the elapsed time between the dam collapse and the arrival in Bento Rodrigues Town was approximately 30 to 40 min.

Downstream of the dams, the floodwave went over the flood plains of the Santarém creek, then to Gualaxo do Norte River and to Carmo River carrying the riverine vegetation and part of the soil, affecting an area of 15 km<sup>2</sup>. The floodwave traveled 70 km in the Gualaxo do Norte River plus 25 km in the Carmo River until the Doce River. Through the Doce River it ran for approximately 570 km passing through four hydropower plants reservoirs and finally reaching the ocean (ANA, 2016a). Figure 3.7 shows the location of the Fundão Dam and the mud flood path.



**Figure 3.7 – Fundão Dam location and the mud flood path**

According to Samarco (IBAMA, 2016) approximately 90% of the spilled material settled between the Fundão Dam and the Candonga Dam, over 118 km. However, the remaining material that reached the Doce River downstream of Candonga Dam resulted in a high concentration of solids in suspension, causing a massive environmental damage. Although the field survey showed that the mud was not toxic (CPRM & ANA, 2015b), nearly 3 tons of fish were killed and the high turbidity caused disruption of the water supply in 12 cities, affecting an estimated population of 424,000 (ANA, 2016a; IBAMA, 2016). The expected clean up and restoration costs is approximately US\$54 billion (Garcia et al., 2017; Burritt & Christ, 2018).

### 3.3 Available Data in the Doce River

After the accident, the Geological Service of Brazil and the National Water Agency conducted several measurements at 10 spots along the Doce River in order to follow the floodwave and the high turbidity (CPRM & ANA, 2015a). The first survey occurred during the period of 7 to 23 November of 2015, where the Brazilian agencies collected data of discharge, water level, temperature, dissolved oxygen, pH, turbidity, particle size and concentration of sediments in suspension. Figure 3.8 presents the location of the data collection sites, being 7 gaging stations and 4 additional measurement sites. Table 3.2 provides a description about the type of data of interest collected on each location.



**Figure 3.8 – Location of the data collection sites**

**Table 3.2 – Summary of collected data on the first survey**

ID	Station Name	NWA Code	Data Available
G7	Fazenda Cachoeira D'Antas	56425000	Cross section, stage-discharge curve
G6	Cachoeira dos Óculos	56539000	Discharge each 15 minutes, turbidity, suspended sediment concentration, particle size, cross section and stage-discharge curve
G5	Belo Oriente	56719998	Discharge each 1 hour, turbidity, suspended sediment concentration, particle size, water temperature, cross section and stage-discharge curve
G4	Governador Valadares	56850000	Discharge each 1 hour, turbidity, suspended sediment concentration, particle size, water temperature, cross section and stage-discharge curve
G3	Tumiritinga	56920000	Discharge with 2 measurements per day, turbidity, suspended sediment concentration, particle size, water temperature, cross section and stage-discharge curve
S4	Resplendor	-	Turbidity, suspended sediment concentration, particle size and water temperature
S3	Baixo Guandu	-	Turbidity, suspended sediment concentration, particle size and water temperature
S2	Ponte Fontinelli/ Mascarenhas Jusante	56992480	Discharge each 1 hour with several gaps, turbidity, suspended sediment concentration, particle size and water temperature
G2	Colatina	56994500	Discharge each 15 minutes, suspended sediment concentration, particle size, cross section, stage-discharge curve and water temperature
G1	Linhares	56998200	Discharge with 2 measurements per day, turbidity, suspended sediment concentration, particle size, water temperature and cross section
S1	Povoação	-	Turbidity, suspended sediment concentration, particle size and water temperature

The availability of sediment and discharge data along the Doce River during the transit of the floodwave after the dam break provides a unique opportunity to investigate the sediment transport along the river. However, the floodwave propagation and the existence of hydropower plants reservoirs add more complexity to the analysis. The next sections present the processing and analysis of the collected data.

### 3.3.1 Hydraulic Geometry and Bed Material

Knowledge about the river hydraulic geometry is a requirement to investigate the flow and sediment transport features. Table 3.3 shows the result of processing data from the National Water Agency and for the National Electrical System Operator from Brazil (ANA, 2017; ONS, 2017). Bed material data are provided by the Brazilian agencies (CPRM & ANA, 2016a). The distance presented is determined from the Fundão Dam location and the river slope is obtained from a digital elevation model of the Doce River basin, with a spatial resolution of 10 m (Geonetwork, 2007). Bankfull discharge refers to a flood with 1.5 year as period of return (Wohl, 2014).

**Table 3.3 – Doce River features**

Location	Distance (Km)	Catchment Area (km <sup>2</sup> )	Bankfull Discharge (m <sup>3</sup> /s)	Channel Width (m)	Slope (m/m)	Bed Material $d_{50}$ (mm)
Candongá Dam	118.3	9,007	535	130	0.0005	-
G7	176.7	10,100	596	140	0.0005	0.50
G6	213.1	15,836	842	150	0.0005	0.62
G5	286.7	24,204	1,312	240	0.0005	0.50
Baguari Dam	343.6	38,311	2,130	280	0.0005	-
G4	368.9	39,828	2,180	320	0.0005	0.70
G3	412.3	54,900	2,397	400	0.0005	0.62
S4	476.3	61,200	2,944	470	0.0005	-
Aimorés Dam	503.6	62,167	3,055	480	0.0005	-
S3	515.1	71,640	3,390	590	0.0008	-
Mascarenhas Dam	525.5	73,700	3,477	620	0.0008	-
S2	532.2	74,146	3,483	625	0.0008	-
G2	559.7	75,800	3,524	630	0.0002	0.58
G1	624.4	82,100	3,741	810	0.0002	0.57
S1	663.4	82,647	3,837	820	0.0002	-

### 3.3.2 Cross Section Survey

Bathymetric data on the stations along the Doce River were collected by acoustic equipment Sontek-M9, while the dry part of the profile was surveyed using the total station Leica-CT407 (CPRM & ANA, 2016a). Evaluation of the alterations in the rivers' main channel is made by the comparison of the surveyed cross section before and after the dam collapse. Figure 3.9 up to Figure 3.11 provides a comparison of the cross sections before and after the dam break.

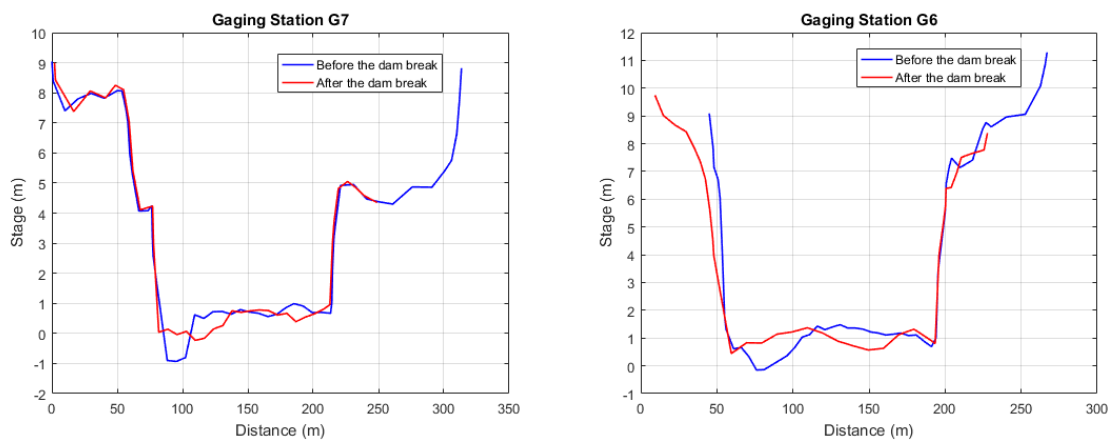


**Figure 3.9 – Cross section survey in the Doce River at stations G7 and G6**

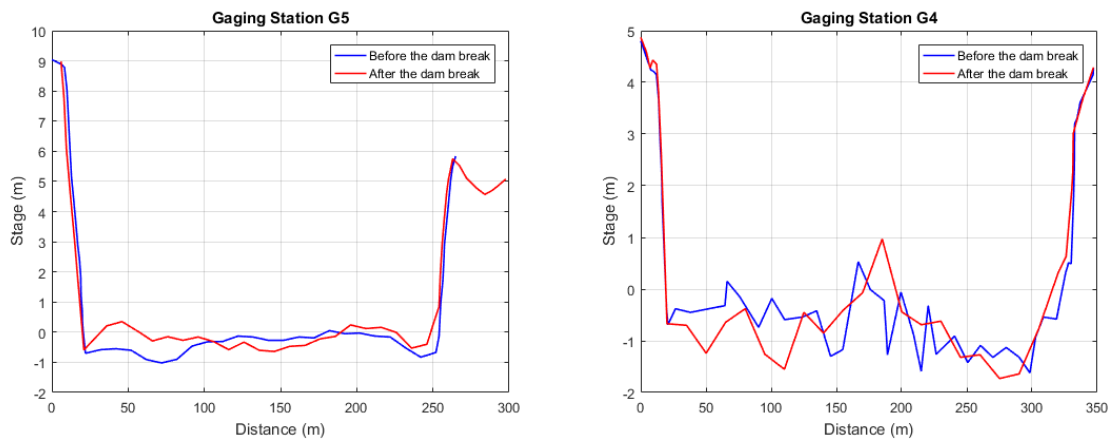


**Figure 3.10 – Cross section survey in the Doce River at stations G5 and G4**

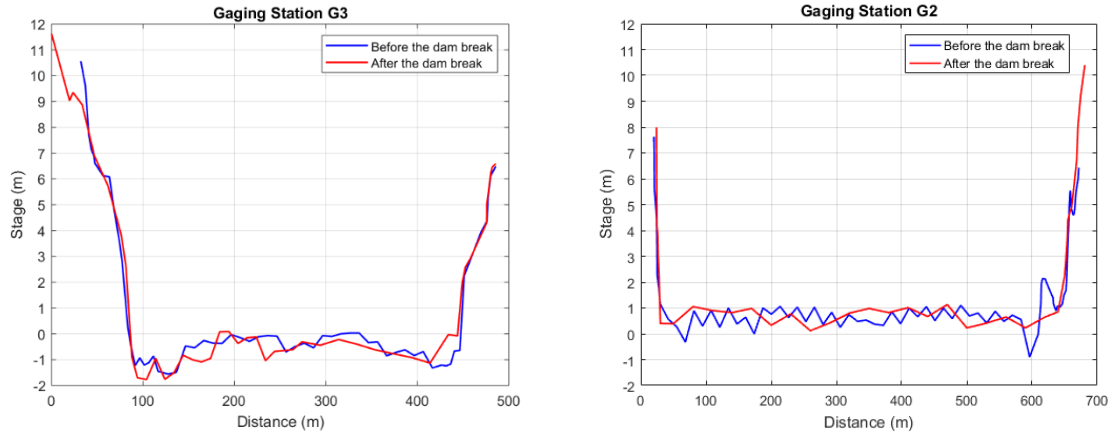


**Figure 3.11 – Cross section survey in the Doce River at stations G3 and G2**

Table 3.4 presents the survey data, the area of the main channel and a comparison before and after the dam break.

**Table 3.4 – Date of survey before and after the dam break**

Gaging Station	Before dam break		After dam break		Area Difference
	Survey Date	Area (m <sup>2</sup> )	Survey Date	Area (m <sup>2</sup> )	
G7	08/19/2014	670	12/12/2015	652	2.7%
G6	05/12/2015	950	11/12/2015	975	-2.6%
G5	08/25/2014	1483	12/09/2015	1461	1.5%
G4	06/17/2012	1573	12/05/2015	1581	-0.5%
G3	12/03/2014	2718	12/06/2015	2744	-1.0%
G2	08/24/2015	4677	12/07/2015	4622	1.2%

The comparison of the cross-section areas shows that there were no major changes in the river geometry along the Doce River after the Fundão Dam collapse.

### 3.3.3 Stage Discharge Curves

Figure 3.12 to Figure 3.14 present the stage discharge curves (ANA, 2017) along the Doce River gaging stations. According to the Geological Service of Brazil, the survey carried out after the dam collapse showed that the event did not result in changes for the stage discharge relationship in any gaging station (CPRM & ANA, 2016a).

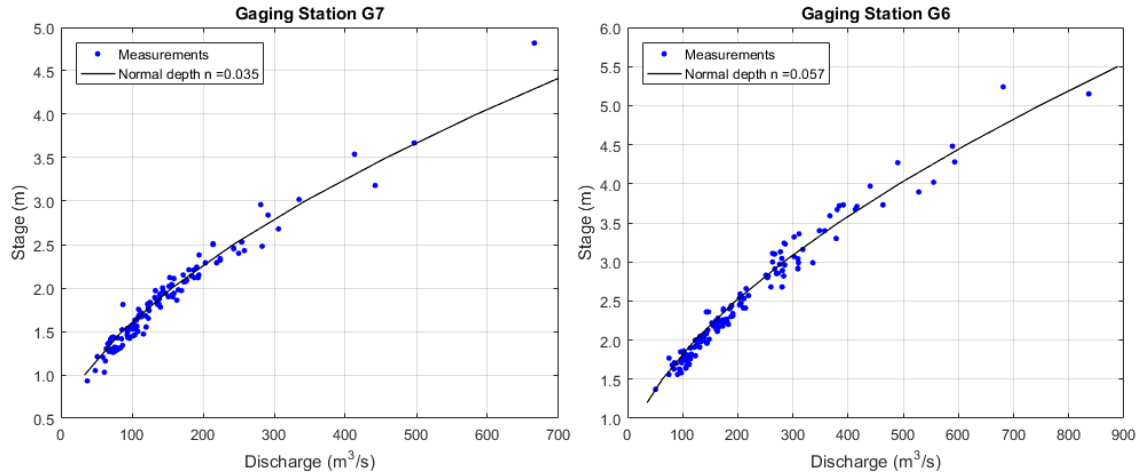


**Figure 3.12 – Stage-discharge curves at stations G7 and G6**

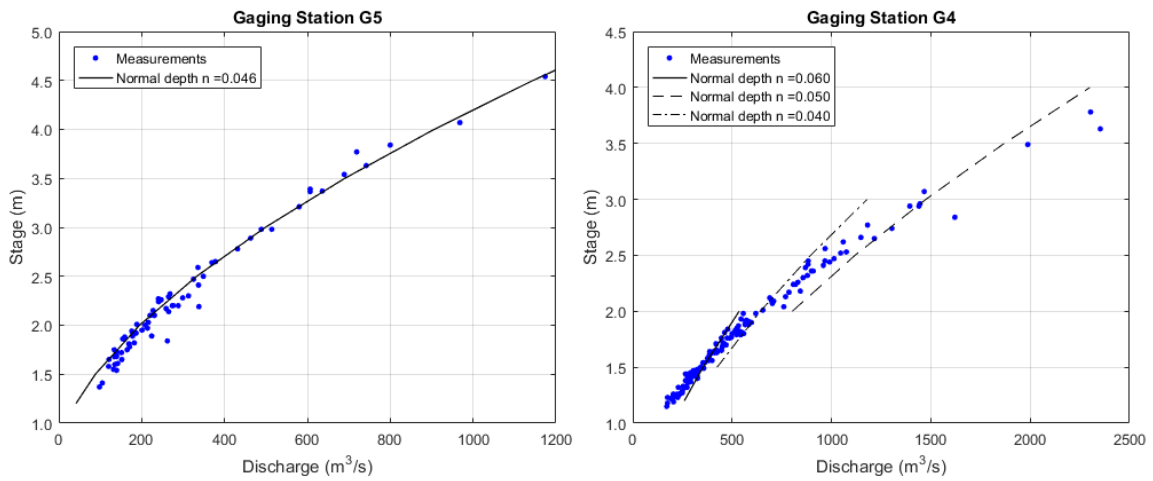


**Figure 3.13 – Stage-discharge curves at stations G5 and G4**

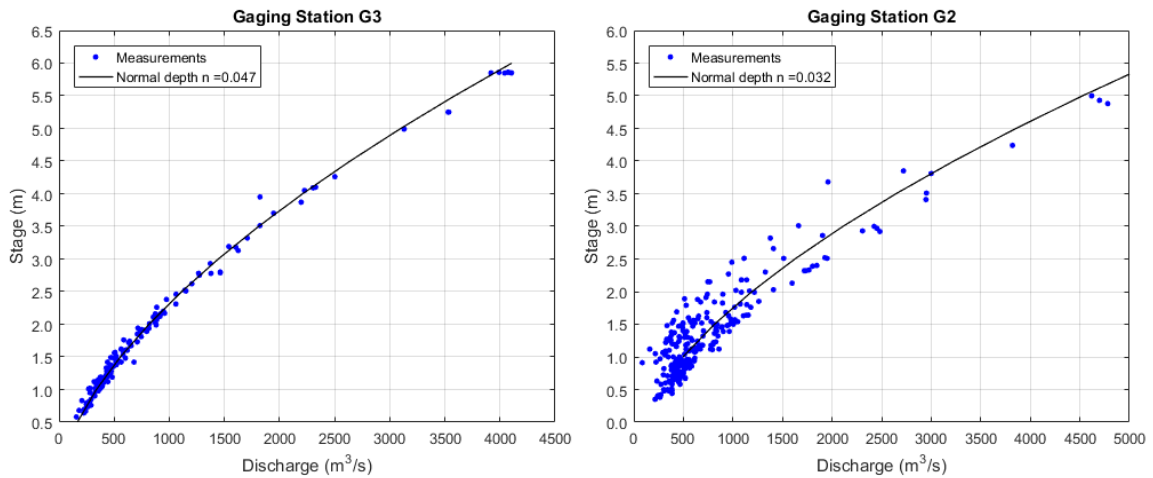


**Figure 3.14 – Stage-discharge curves at stations G3 and G2**

Table 3.5 summarizes the bed slope and the Manning roughness coefficient  $n$  for each gaging station under the normal depth assumption.

**Table 3.5 – Manning’s  $n$  coefficient in the Doce River gaging stations**

Station	So	Manning $n$
G7	0.0005	0.035
G6	0.0005	0.057
G5	0.0005	0.046
G4	0.0005	0.050
G3	0.0005	0.047
G2	0.0002	0.032

According to the data presented in Table 3.5, the average value of the Manning’s  $n$  coefficient along Doce River is 0.045. However, due to river features such as bed rock in some reaches and islands, as illustrated in Figure 3.15 and Figure 3.16, the roughness can increase significantly for low flow conditions.



**Figure 3.15 – Doce River, 55 km downstream of station G3 in 05/03/2005,  $Q \approx 1,000 \text{ m}^3/\text{s}$  (Google, 2018)**



**Figure 3.16 – Doce River, 55 km downstream of station G3 in 08/09/2017,  $Q \approx 130 \text{ m}^3/\text{s}$  (Google, 2018)**

#### 3.3.4 Hydrographs

The floodwave originated by the Fundão Dam collapse traveled for approximately 670 km along the Doce River basin streams. According to the Brazilian agencies (ANA, 2016a) and aerial images (Google, 2015), the flood spread along the floodplains in the upstream region of the basin until the Candonga Dam reservoir (Figure 3.8). From this location to downstream, the floodwave traveled in the river's main channel.

The passage of the quick rising flood hydrograph was recorded by the gaging stations along the Doce River as described previously in Table 3.2. These stations are part of the Alert System of Critical Events of the Geological Survey of Brazil and National Water Agency. The system was originally designated to warn the riverine towns around the Doce River about flood risk during the rainy season (CPRM & ANA, 2016a). Figure 3.17 shows the hydrographs registered at the gaging stations in the following days after the failure.

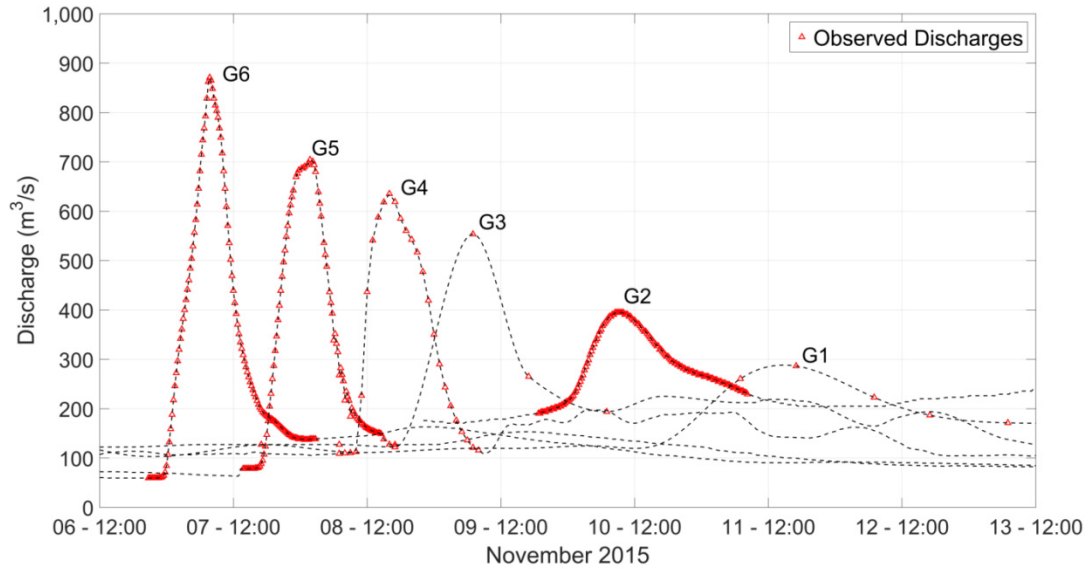


**Figure 3.17 – Observed hydrographs after the Fundão Dam failure**

Besides the gaging stations records, there is a register of the peak discharge at Candonga dam of about 1,900 m<sup>3</sup>/s on 11/06/2015 at 10:00h (Martins, 2015). There are also discharge data in Aimorés Dam and downstream of Mascarenhas Dam, however with gaps (ANA, 2017). Table 3.6 presents the data of the hydrograph peak and the distance of each measurement site. According to the observed hydrographs, the average floodwave celerity along the Doce River was approximately equal to 1.2 m/s.

**Table 3.6 – Discharge peak observed along Doce River after the Fundão Dam collapse**

Location	Distance (km)	Date and Local Time	Elapsed Time (h)	Maximum Discharge Observed (m <sup>3</sup> /s)
Fundão Tailings Dam	0	11/05/2015 15:45	0.0	?
Candonga Dam	118.3	11/06/2015 10:00	18.2	1900
G6	213.1	11/07/2015 7:45	40.0	871
G5	286.7	11/08/2015 1:45	58.0	704
G4	368.9	11/08/2015 16:00	72.2	635
G3	412.3	11/09/2015 7:00	87.2	554
G2	559.7	11/10/2015 8:30	112.7	394
G1	624.4	11/11/2015 17:00	145.3	286

The quantification of flashiness (rate of flow change) of the hydrograph after the dam collapse is made by the Richard-Baker Flashiness Index (Baker et al., 2004), as shown in Equation 3.1.

$$R - B \text{ Index} = \frac{\sum_{i=1}^N |Q_i - Q_{i-1}|}{\sum_{i=1}^N Q_i} \quad (3.1)$$

In order to compare the flashiness of a natural condition in the Doce River, this index is also applied to a natural flood, which occurred between December 2016 and January 2017 and lasted for approximately 30 days (ANA, 2017). Table 3.7 shows the Richard-Baker Flashiness Index considering an hourly discharge variation. As one can conclude, the flashiness index for the hydrograph after the dam break is up to 15 times higher than for natural floods in the same river.

**Table 3.7 – Analysis of hydrograph flashiness**

Station	Flashiness Index	
	Dam Break	Natural Flood (2016-2017)
G6	0.17	0.011
G5	0.14	0.011
G4	0.11	0.019

### 3.3.5 Turbidity

Turbidity is the measure of relative clarity of a liquid and it expresses the amount of light that is scattered by material in the water when light is shined through the water sample. Therefore, the higher the intensity of scattered light, the higher the turbidity. It is measured in nephelometric turbidity units (NTU) (USGS, 2019). The turbidity of the Doce River waters after the dam collapse was measured at each station at the same time as the sediment concentration using a portable turbidimeter PoliControl-2000 (CPRM & ANA, 2015a). The relationship obtained between the suspended sediment concentration in mg/l and the turbidity in NTU is presented in Figure 3.18. Accordingly, in the Doce River the concentration of suspended sediment (SS) and the turbidity (NTU) was  $SS/NTU \approx 0.5$ .

The relationship between suspended sediment and turbidity is fundamental for the evaluation of the impact of the tailings spill on the water supply along the basin. According to Chang and Liao (2012), turbidity levels higher than 5,000 NTU hinder conventional water treatment. Such turbidity level corresponds to a sediment concentration of ~2,500 mg/l in the Doce River.

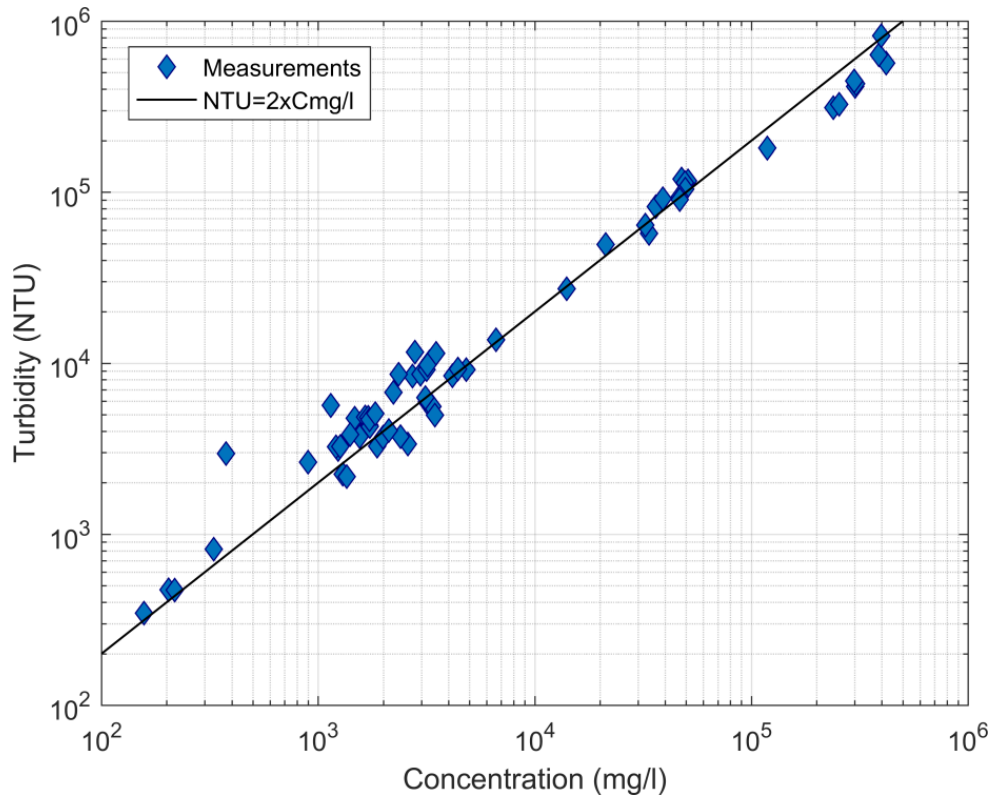


**Figure 3.18 – Relationship of turbidity and suspended sediment concentration measured in the Doce River after the Fundão Dam collapse**

### 3.3.6 Suspended Sediment Concentration

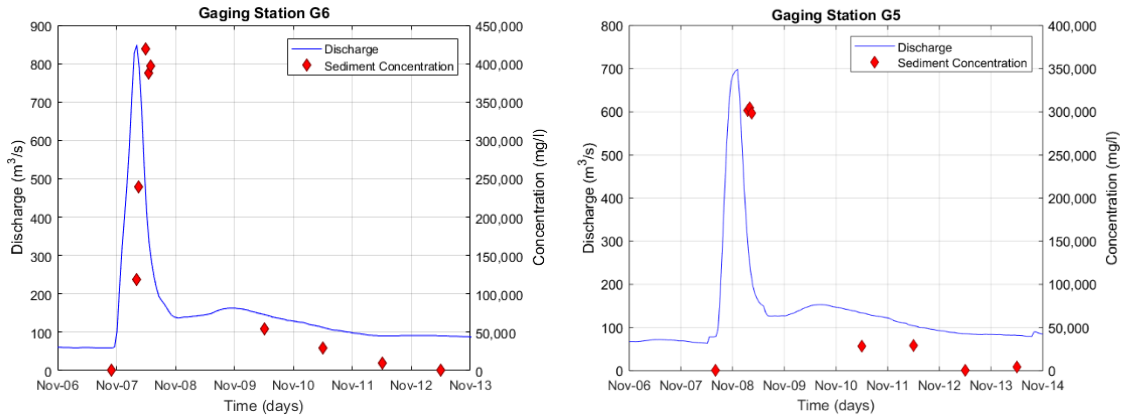
Sediment concentration data were collected using 400 ml instantaneous samplers near the banks, positioned 30 cm deep from the surface. After that, the collected material was preserved in refrigeration until the moment of the analysis. Concentration was determined by gravimetry/evaporation while the particle size was measured by laser scattering, using the Laser Granulometer Malvern 2000. Both procedures were carried out in the labs LAMINBH and GEOSOL in Brazil (CPRM & ANA, 2016b).

Table 3.8 summarizes the maximum observed value of concentration measured along Doce River. One should note that these maximum values do not necessarily represent the peak of sediment concentration, since the measurements were irregularly spaced.

**Table 3.8 – Maximum concentration observed in Doce River after the Fundão Dam collapse**

Location	Accumulated Distance (km)	Number of Measurements	Maximum Concentration Observed (mg/l)	Date for Maximum
Fundão Tailings Dam	0	-	?	
Candongá Dam	118.3	-	-	-
G6	213.1	10	418,848	11/7/2015 12:00
G5	286.7	10	304,594	11/8/2015 8:00
Baguari Dam	343.6	-	-	
G4	368.9	13	50,942	11/10/2015 12:00
G3	412.3	14	31,056	11/12/2015 11:00
S4	476.3	10	7,706	11/15/2015 11:00
Aimorés Dam	503.6	-	-	
S3	515.1	9	3,508	11/17/2015 20:30
Mascarenhas Dam	525.5	-	-	
S2	532.2	7	2,358	11/19/2015 8:30
G2	559.7	11	2,226	11/20/2015 8:00
G1	624.4	6	1,530	11/21/2015 20:00
S1	663.4	4	252	11/21/2015 16:30

Later, during the fourth survey (November 27 to December 19 of 2015), the Brazilian Agencies carried out simultaneously the instantaneous and depth-integrated procedures in all gaging stations to check the accuracy of the data collected using the instantaneous samplers on the first survey (just after the dam collapse). The depth-integrated procedure was done in the same stations using 5 verticals along the river cross sections using a DH-2 sampler. For each vertical, a volume of approximately 1 liter was collected. The instantaneous samples were collected on the banks, as it was in the first survey. The result of this analysis showed that there was no significant difference between the two methodologies (CPRM & ANA, 2016a). Figure 3.19 up to Figure 3.21 show the plots of the timing between the floodwave and sediment concentration peak after the dam collapse.



**Figure 3.19 – Hydrograph and suspended sediment concentration at gaging stations G6 and G5**

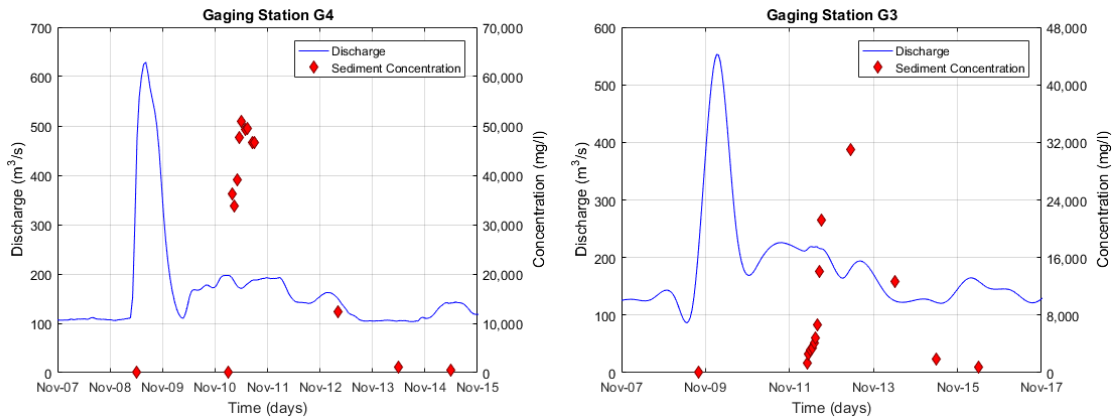


**Figure 3.20 – Hydrograph and suspended sediment concentration at gaging stations G4 and G3**

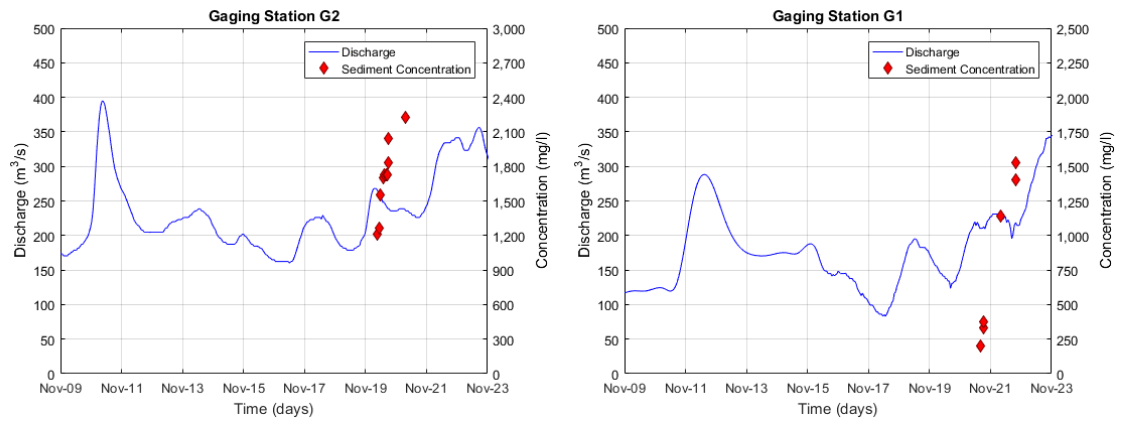


**Figure 3.21 – Hydrograph and suspended sediment concentration at gaging stations G2 and G1**

As observed in the previous figures, there is lag between the floodwave propagation and the suspended sediment transport. This effect is even more pronounced in the downstream gaging stations, where the difference is up to ten days. The occurrence of such physical phenomena can be attributed to the retarding effect of the reservoirs over the sediment and the difference between celerity and flow velocity.

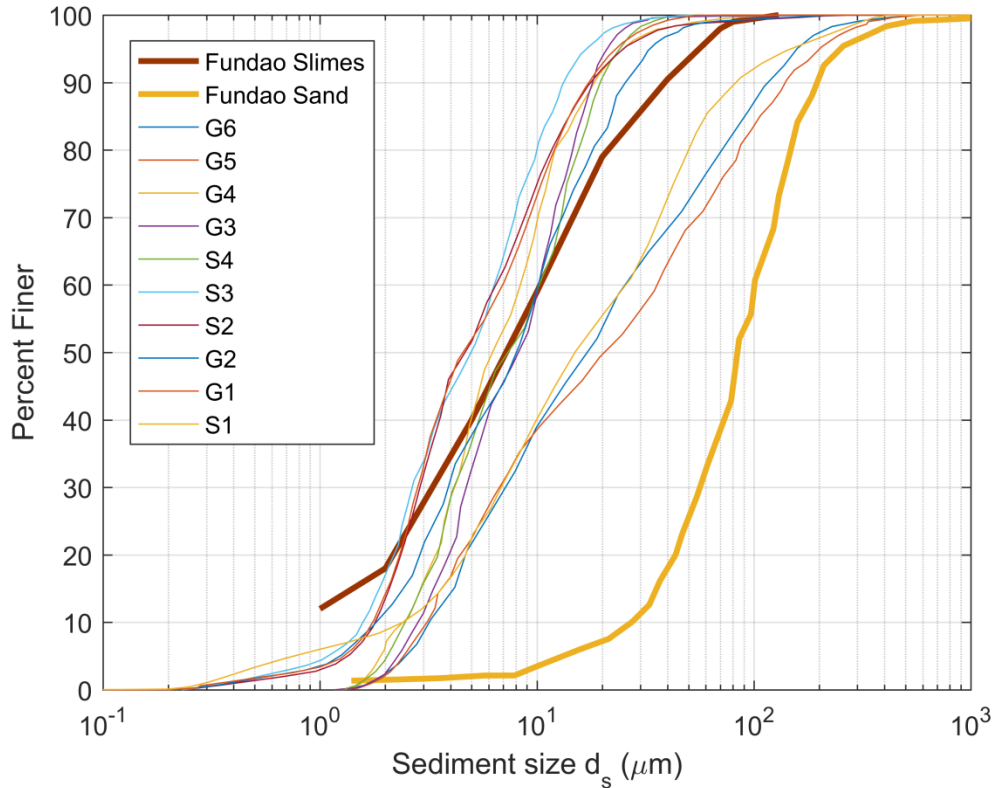
### 3.3.7 Particle Size Distribution

Table 3.9 provides a comparison between the particle size distribution of the material impounded in the Fundão Dam (Morgenstern et al., 2016) and the suspended sediment collected along the Doce River stations after the dam collapse (CPRM & ANA, 2015a).

**Table 3.9 – Particle size of the stored material in the Fundão Dam reservoir and collected along the Doce River**

Location	$d_{10}(\mu m)$	$d_{50}(\mu m)$	$d_{90}(\mu m)$
Fundão Sand	23.7	84	196
Fundão Slimes	≈1.0	7.5	40
G6	3.7	18.1	106.8
G5	3.7	17.9	109.6
G4	2.7	6.6	21.6
G3	3.0	7.7	19.0
S4	2.9	7.4	17.4
S3	1.0	3.8	12.5
S2	1.5	5.4	19.2
G2	1.5	5.9	21.9
G1	1.6	6.0	20.2
S1	1.3	15.5	102.9

Figure 3.22 shows the plot of the particle distribution of both materials.



**Figure 3.22 – Particle size distribution of the Fundão Dam impounded material and observed along the Doce River**

Following the sediment grade scale given by Julien (2010), one can conclude that the coarser material in the Fundão Dam is medium silt to fine sand, while the finer material is medium clay to coarse silt. It is noticeable that most of the sand impounded in the Fundão reservoir was deposited in the upstream region of the basin. Furthermore, the particle size distribution in the gaging G6, G5 and G4 shows that the material in suspension approximates to the combined distribution of the material stored in the dam (sand and slimes). For the stations located further downstream the particle sizes are closer to the impounded slimes (fine material), since the coarser material has already been deposited. This fine material remains in suspension, passing through almost the whole river and the four reservoirs without depositing and arriving in the ocean approximately two weeks after the collapse.

## 4. DATA ANALYSIS

### 4.1 Spilled Volume Balance

The spilled volume of tailings (without water) immediately after the Fundão Dam collapse was estimated at 32 Mm<sup>3</sup> (IBAMA, 2016; Morgenstern et al., 2016). In addition, the water volume released is calculated at 24 Mm<sup>3</sup>, being approximately the volume of the observed hydrographs in the first two gaging stations in the Doce River (G6 and G5). Thus, the total volume spilled during the Fundão Dam accident is computed as 56 Mm<sup>3</sup>, which is in good agreement with some records in the literature (Antunes, 2015; Burritt & Christ, 2018). The volume of tailings that remained in the reservoir after the accident was approximately 24 Mm<sup>3</sup> (IBAMA, 2016), resulting in a total stored volume before the accident of approximately 80 Mm<sup>3</sup>.

According to Morgenstern et al., (2016), in the days preceding the failure the dam crest was approximately at the elevation 900 (masl), what corresponds to a stored volume of approximately 77 Mm<sup>3</sup> (Machado, 2017), which shows a satisfactory agreement with the volume balance. However, as mentioned by the Brazilian Institute of Environment and Renewable Natural Resources (IBAMA, 2016), in the months following the collapse (November 2015 to February 2016) the heavy rain in the region resulted in a progressive release of 11 Mm<sup>3</sup> of additional stored tailings from the Fundão Dam. Ultimately, the total sediment volume released in the Fundão Dam accident was approximately 43 Mm<sup>3</sup> (IBAMA, 2016; Renova, 2018).

An important environmental concern about tailings dam failures is the destination of the spilled tailings because it contaminates the floodplains, water and bed sediment along the river. Moreover, the deposited sediment can be resuspended during flood events, what results in high turbidity, affecting the aquatic life and the water treatment systems. Thus, Figure 4.1 shows an estimate of the volume of sediment transported immediately after the Fundão Dam collapse based on the field survey carried out by the Brazilian agencies (CPRM & ANA, 2015a; IBAMA, 2016).

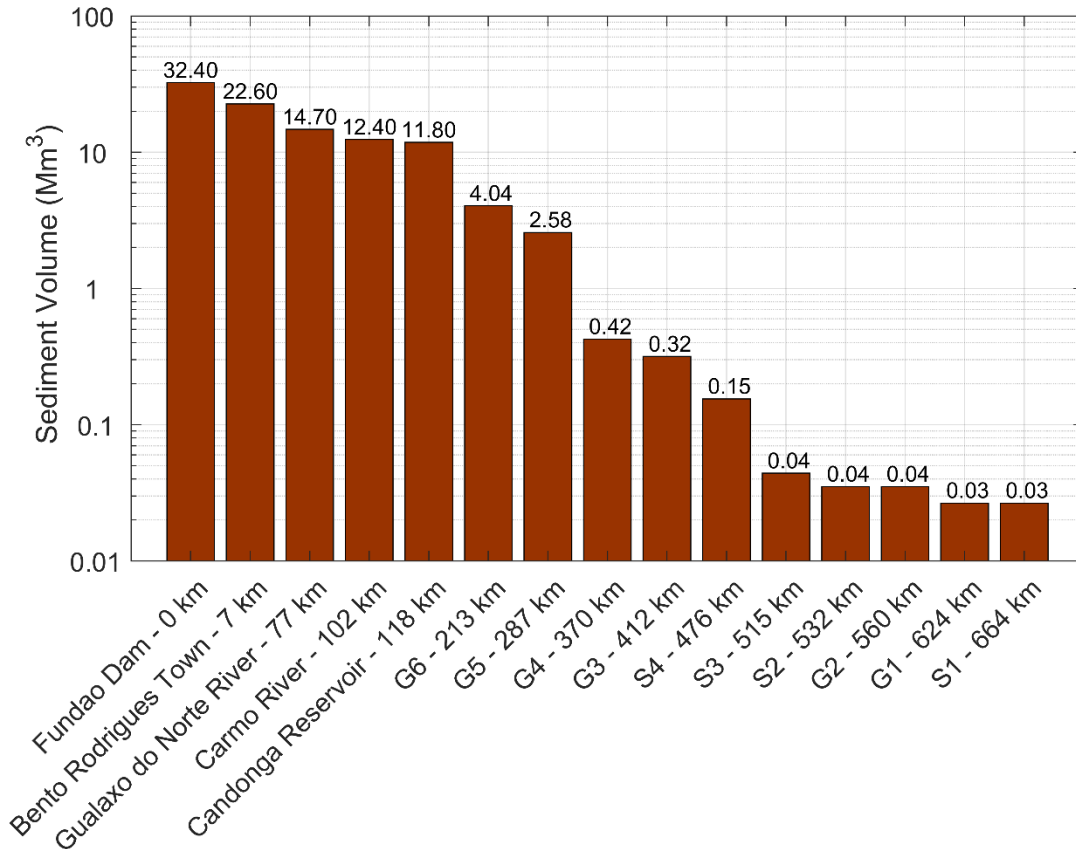


**Figure 4.1 – Estimative of sediment volume decay along the Doce River basin**

While the volume indicated upstream of the gaging station G6 is based on the field survey (IBAMA, 2016), the volume of the suspended load downstream from this gaging station is estimated by the product of the measured suspended sediment concentration by the discharge on the stations along the Doce River, as shown in Equation 4.1.

$$L_S = \int Q_S dt \quad (4.1)$$

Where  $L_S$  is the suspended load and  $Q_S$  is the total suspended sediment discharge. Figure 4.1 shows an exponential decay in the sediment amount as the flood moves forward.

A large volume of tailings (approximately 86% of the spilled volume) deposited in the upstream region of the Doce River Basin (118 km downstream of the dam). Settling occurred more specifically in the Bento Rodrigues Town, in the floodplains and along the bed of the Gualaxo do Norte and Carmo Rivers. In order to illustrate the tailings deposition, Figure 4.2 shows the Fundão Dam site before the collapse (aerial image from Google Earth at date of 07/20/2015) while Figure 4.3 shows the same site after the collapse (aerial image from Google Earth at date of 11/11/2015). Furthermore, immediately after the accident, the Candonga Dam reservoir trapped 7 million cubic meters of sediment (IBAMA, 2016). By the end of February of 2016, sediment carried by rain increased the volume trapped in this reservoir to 9.5 million cubic meters (IBAMA, 2016).

Finally, as a comparison, in the Doce River basin the estimated annual sediment flux into the ocean is approximately 10 million tons per year (Milliman & Farnsworth, 2013), which corresponds to a volume of  $3.8 \text{ Mm}^3/\text{year}$  and an annual sediment yield of  $120 \text{ t/km}^2/\text{year}$ . Therefore, the volume of sediment (tailings) released immediately after the Fundão Dam collapse ( $32 \text{ Mm}^3$ ) was equivalent to more than 8 years of sediment yield in the Doce River basin. However, due the sediment deposition along the river and in the hydropower reservoirs, the amount that arrived in the ocean ( $\approx 0.03 \text{ Mm}^3$ ) represents only 0.8% of the annual sediment flux.



**Figure 4.2 – Fundão Dam site before the collapse (Google, 2015)**

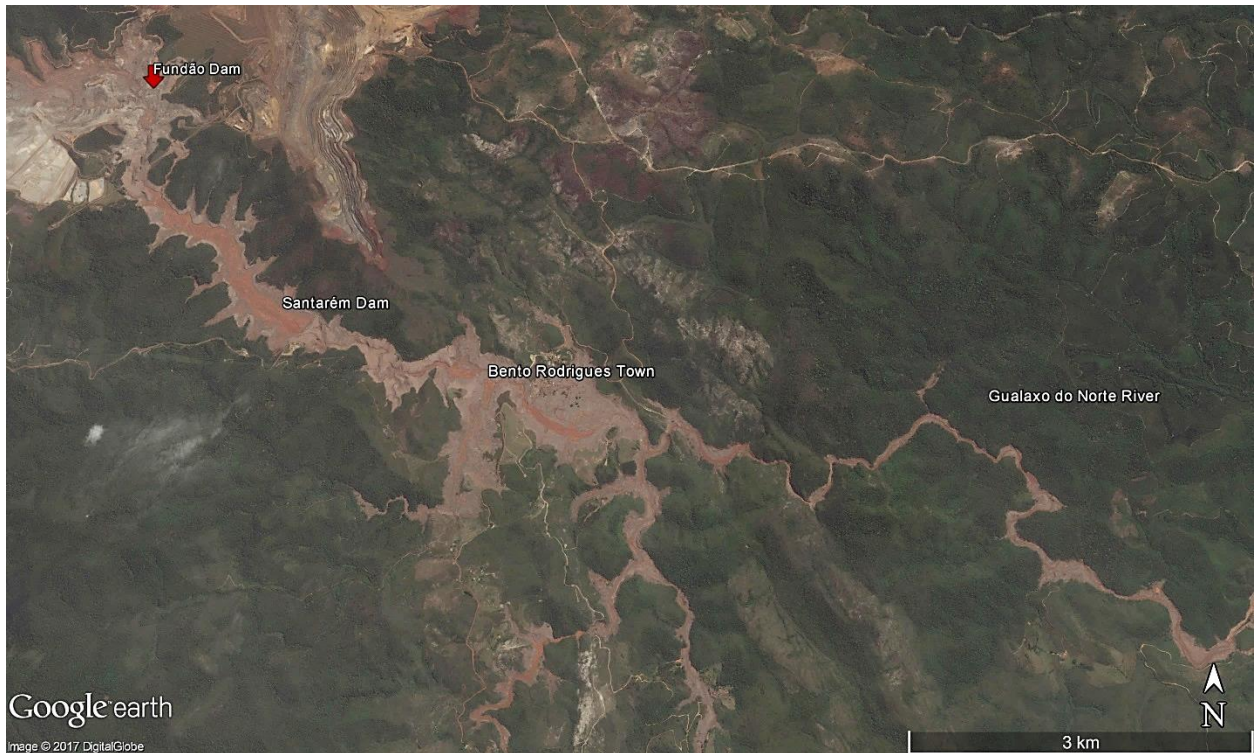


**Figure 4.3 – Fundão Dam site after the collapse (Google, 2015)**

## 4.2 Hyperconcentrated Flow Analysis

An approximation for the volumetric concentration in the sites upstream of the Candonga Dam can be obtained from the application of Equation 2.47, being the volume of the water equal to the hydrograph volume in the Doce River. For the downstream sites, the volumetric concentration is estimated from the observed concentrations, calculated using expression (4.2) (Julien, 2010):

$$C_v = \frac{C_{mg/l}}{10^6 G} \quad (4.2)$$

Where  $C_v$  is the volumetric sediment concentration,  $C_{mg/l}$  is the concentration of the suspended sediment in mg/l and  $G$  is the specific gravity of the sediment. Table 4.1 summarizes the estimate volumetric concentration and the hyperconcentrated flow classification.

**Table 4.1 – Hyperconcentration analysis**

Location	Distance (Km)	Sediment Volume (Mm <sup>3</sup> )	Volumetric Concentration $C_v$	Classification
Fundão Dam	0.0	32.40	57.45%	Landslide
Bento Rodrigues Town	6.5	22.60	48.50%	Mud Flow
Gualaxo River	77.3	14.70	37.98%	Mud Flood
Carmo River	102.1	12.40	34.07%	Mud Flood
Candonga Reservoir	118.3	11.80	32.96%	Mud Flood
G6	213.1	4.04	15.81%	Water Flood
G5	286.7	2.58	11.76%	Water Flood
G4	368.9	0.42	1.95%	Water Flood
G3	412.3	0.32	1.37%	Water Flood
S4	476.3	0.15	0.82%	Water Flood
S3	515.1	0.04	0.14%	Water Flood
S2	532.2	0.04	0.11%	Water Flood
G2	559.7	0.04	0.10%	Water Flood
G1	624.4	0.03	0.07%	Water Flood
S1	663.5	0.03	0.06%	Water Flood

Following the hyperconcentrated flow characteristic given by O'Brien and Julien (1985), the sediment deposition along the flow path caused a progressive change in the behavior of the hyperconcentrated flow along the Doce River basin.

Due to amount of sediment trapped in the upstream region of the basin and in the Candonga Dam reservoir, the flow in the Doce River has the behavior of “Water Flood”. Therefore, it was considered that the methods used for fluvial hydraulics would apply downstream of Candonga Dam.

#### 4.3 Mode of Sediment Transport along the Doce River

The determination of the mode of sediment transport along Doce River after the Fundão Dam collapse is carried out taking into account the observed discharge, the sediment size and the river features, as presented in Table 4.2.

**Table 4.2 – Mode of sediment transport in Doce River after the Fundão Dam failure**

Station	$Q$ ( $m^3/s$ )	$S_o$	$T$ ( $^{\circ}C$ )	$h$ ( $m$ )	$u_*$ ( $m$ )	$d_{50}$ ( $\mu m$ )	$d_*$	$\omega$ ( $mm/s$ )	$\frac{u_*}{\omega}$	$Ro$	Mode of Sediment Transport
G6	150	0.0005	30	0.89	0.07	18.1	0.53	0.37	180	0.014	suspension
G5	130	0.0005	27	0.48	0.05	17.9	0.50	0.34	145	0.017	suspension
G4	141	0.0005	30	1.26	0.08	6.6	0.19	0.05	1601	0.002	suspension
G3	182	0.0005	30	1.23	0.08	7.7	0.23	0.07	1165	0.002	suspension
G2	309	0.0002	29	1.37	0.05	5.9	0.17	0.04	1358	0.002	suspension
G1	350	0.0002	29	0.86	0.04	6.0	0.17	0.04	1043	0.002	suspension

Parameters in Table 4.2 were calculated using Equations 2.22 to 2.25, considering the observed water temperature. The low Rouse number  $Ro$  indicates a uniform sediment distribution along the flow depth, moreover the analysis shows that the predominant mode of sediment transport is suspension in the whole extension of the Doce River. Therefore, the advection-dispersion equation should provide a proper approach to calculate the sediment transport.

#### 4.4 Longitudinal Dispersion Coefficient along the Doce River

According to Fischer et al. (1979), the routing procedure can be employed to determine the longitudinal dispersion coefficient  $K_d$  in natural streams. Such procedure is originally given by the solution to Equation 2.29 to match an observed downstream tracer cloud based on an upstream observation, however not considering the settling. The value of  $K_d$  is varied until the best fit between the observed and predicted values downstream, being this value regarded as the observed longitudinal dispersion coefficient (Fischer et al., 1979). This procedure is originally applied on conservative substances, however, herein the sediment settling rate  $k$  was taken into account by the application of the analytical solution, given by the Equations 2.31 to 2.33.

The analytical solution requires the discretization of the time-varying suspended sediment concentration series in short time blocks (equivalent to spilling duration  $\tau$ ) with the application of the superposition principle, as illustrated in Figure 4.4. This adapted routing method was applied in the Doce River after the Fundão Dam collapse in reaches with measured sediment concentrations. There was no substantial improvement on the calculations for the blocks with time duration shorter than 1 hour, therefore this was the duration chosen for each block. The methodology considers that the longitudinal dispersion coefficient and the settling rate are constant along each reach. Finally, one should note that the application of the analytical solution can avoid numerical errors on the solution of the advection-dispersion equation.

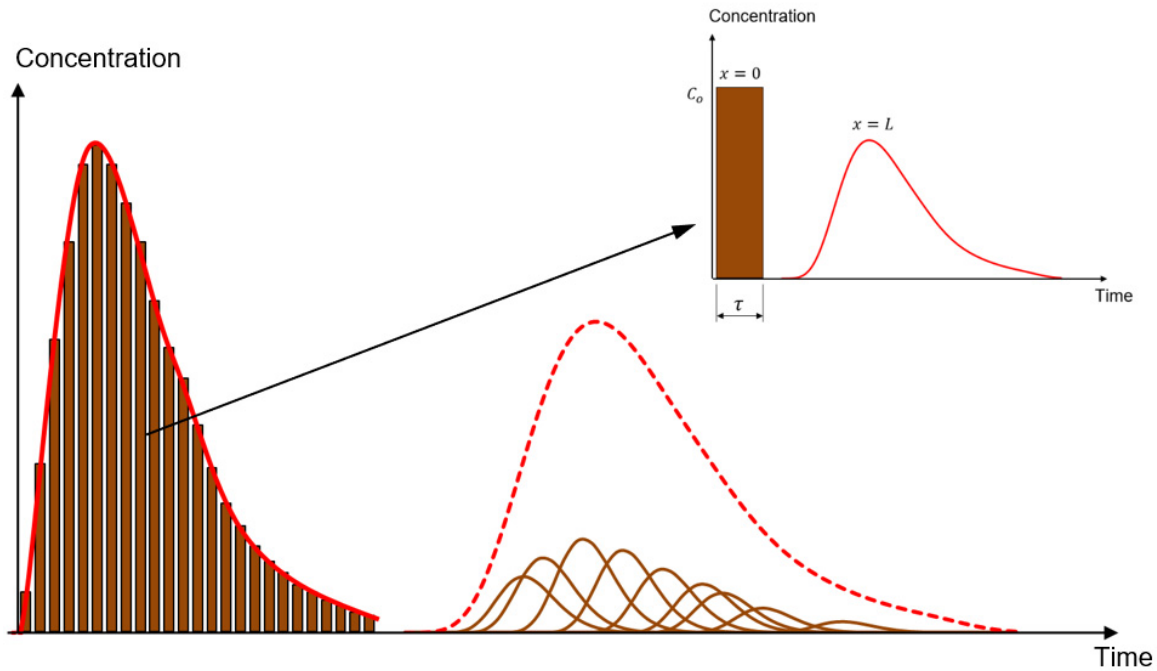


**Figure 4.4 – Application of the analytical solution using the superposition principle**

At gaging station G6 a concentration curve was linearly interpolated using the observed concentration. For the subsequent reaches, the calculated concentration in the downstream station served as input for the following river reach. The adjustment of parameters of flow velocity, longitudinal dispersion coefficient and the sediment settling rate targeted the best fit with the observed data, using the determination coefficient  $R^2$  as the objective function.

$$R^2 = \left( \frac{\sum_{i=1}^n (X_i - \bar{X})(Y_i - \bar{Y})}{\sqrt{\sum_{i=1}^n (X_i - \bar{X})^2 \sum_{i=1}^n (Y_i - \bar{Y})^2}} \right)^2 \quad (4.3)$$

Where  $\bar{X}$  is the average of the measurements and  $\bar{Y}$  the average of the calculated values. For reaches with reservoirs between the observed concentrations, Equation 2.44 was applied. In this case, the calibrated variables were the settling rate and the time needed for the sediment to cross the reservoir. Figure 4.5 to Figure 4.9 shows the results for each river reach and a comparison between the calculated and the measured concentration.

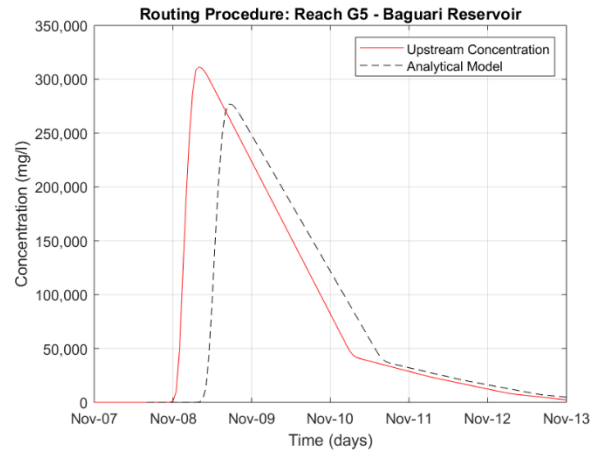
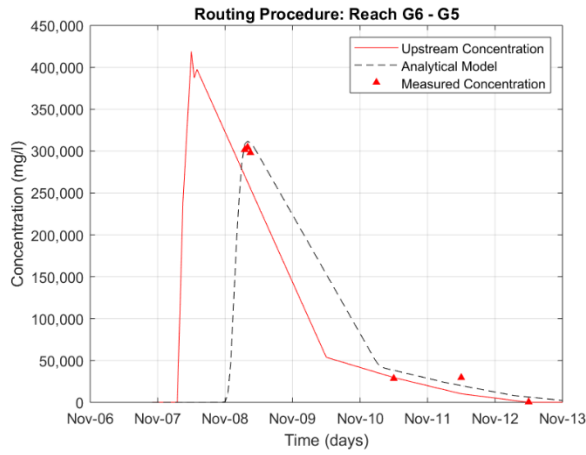


**Figure 4.5 – Routing procedure result in the reaches: G6-G5 and G5-Baguari Reservoir**

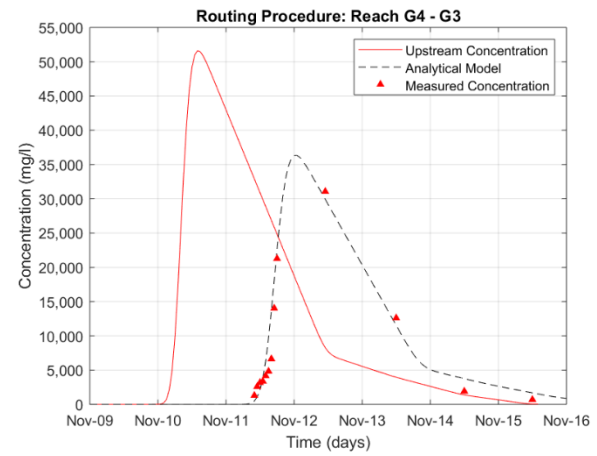
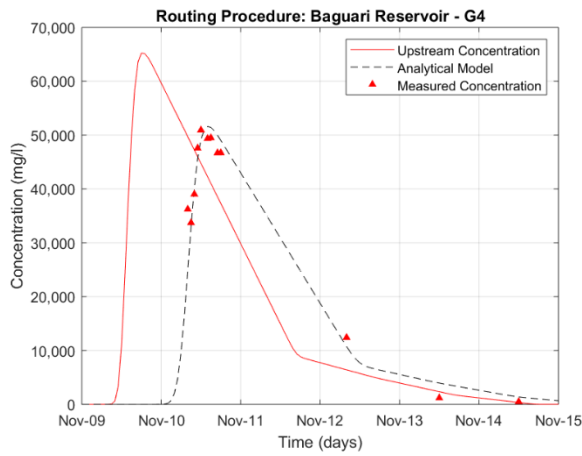


**Figure 4.6 – Routing procedure result in the reaches: Baguari Reservoir-G4 and G4-G3**

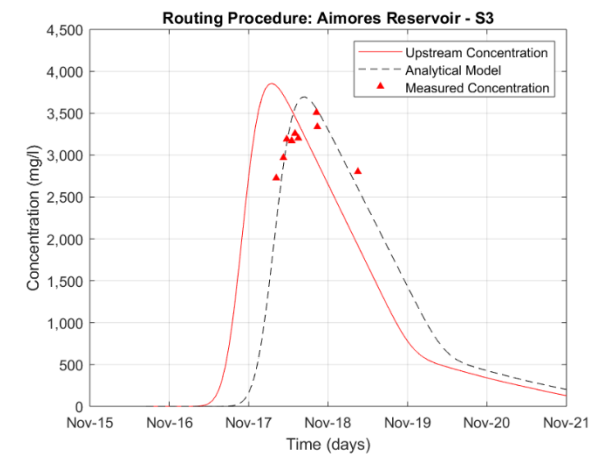
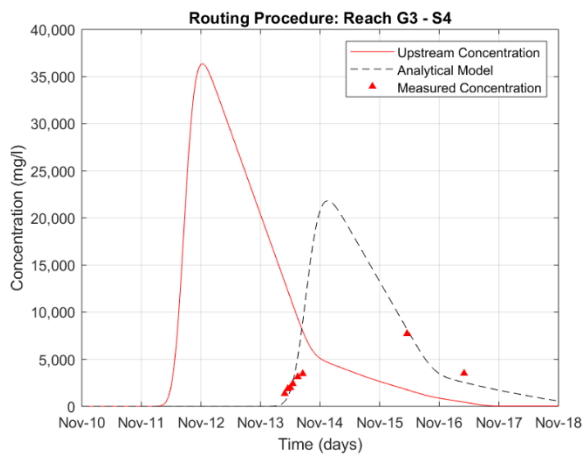


**Figure 4.7 – Routing procedure result in the reaches: G3-S4 and Aimorés Reservoir-S3**

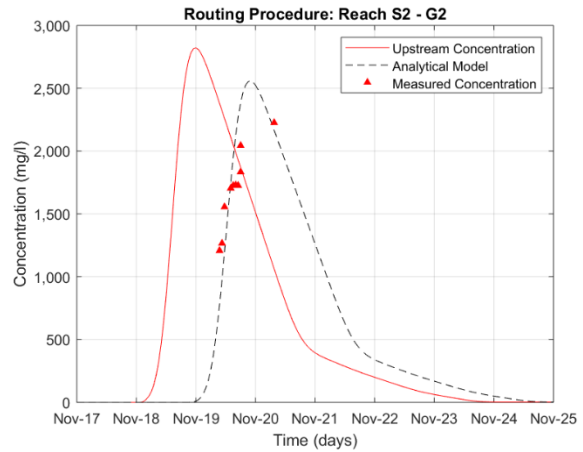
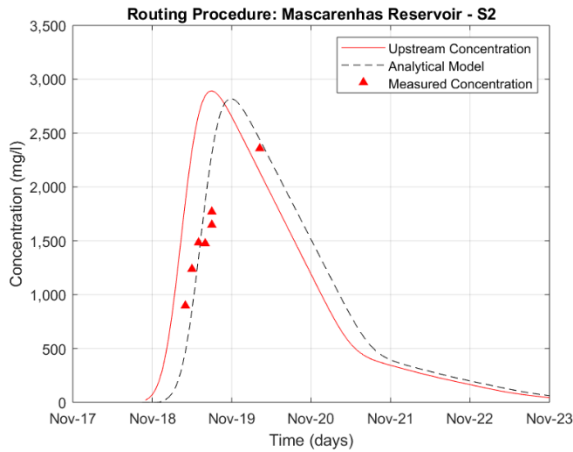


**Figure 4.8 – Routing procedure result in the reaches: Mascarenhas reservoir-S2 and S2-G2**

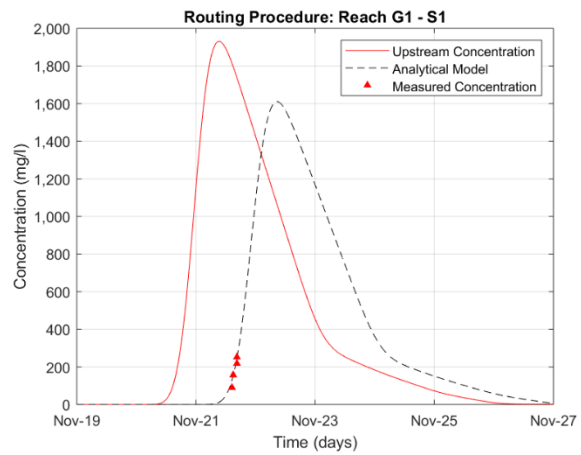
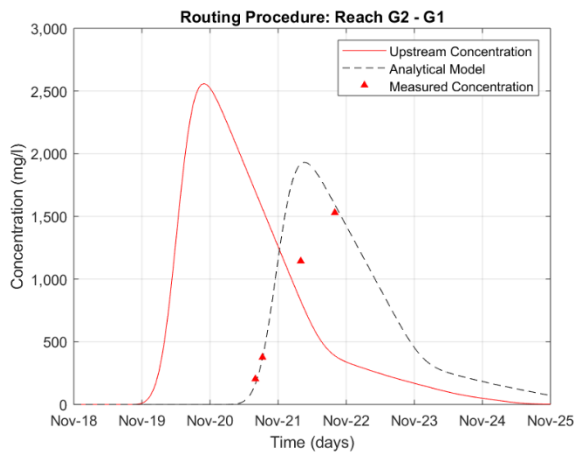


**Figure 4.9 – Routing procedure result in the reaches: G2-G1 and G1-S1**

Table 4.3 presents a summary for the parameters of the Doce River reaches and the values of  $K_d$  obtained.

**Table 4.3 – Longitudinal dispersion coefficient evaluation along the Doce River**

Reach	Distance (km)	$S_o$	$W$ (m)	$U$ (m/s)	$h$ (m)	$u_*$ (m/s)	$K_d$ ( $m^2/s$ )	$R^2$
G6-G5	73.6	0.00050	195	1.12	0.69	0.06	120	0.99
G5-Reservoir	34.9	0.00050	260	1.12	0.45	0.05	120	-
Reservoir-G4	25.3	0.00050	303	0.35	1.33	0.08	35	0.96
G4-G3	43.4	0.00050	360	0.37	1.37	0.08	40	0.92
G3-S4	64.0	0.00050	434	0.37	1.15	0.08	40	0.85
Reservoir-S3	11.5	0.00080	536	0.35	1.08	0.09	30	0.82
Reservoir-S2	6.7	0.00080	622	0.35	1.07	0.09	30	0.78
S2-G2	27.5	0.00080	627	0.36	1.37	0.10	30	0.75
G2-G1	64.7	0.00020	720	0.52	0.94	0.04	50	0.84
G1-S1	39.0	0.00020	815	0.48	0.90	0.04	50	0.96

Results obtained showed that, despite the Doce River width (varying approximately from 200 m to 800 m), the analytical solution presented strong agreement with the observed concentrations at all stations, indicating that the one-dimensional modeling can be used on similar cases of suspended sediment propagation. Nevertheless, the satisfactory performance of the one-dimensional model is related with the massive amount of sediment spilled in the river after the dam collapse and the effect of the spillways jet, which promoted the vertical and lateral mixing in the river reaches.

To check the significance of the calibration parameters determined in the Doce River after the dam collapse, Table 4.4 presents the dimensionless parameters  $K_d/hu_*$  and  $U/u_*$  for the Doce River. In addition, Figure 4.10 shows the plot of the values found in the Doce River and the literature data, which considers 138 points from 50 rivers in U.S., U.K. and New Zealand (McQuivey & Keefer, 1974; Fischer et al., 1979; Rutherford, 1994; Deng et al., 2001; Kashefipour & Falconer, 2002; Carr & Rehmann, 2007). These literature data are presented in Appendix A.

**Table 4.4 – Doce River hydraulic parameters**

Reach	$K_d/hu_*$	$U/u_*$
G6-G5	3010	19.3
G5-Reservoir	5744	23.9
Reservoir-G4	327	4.3
G4-G3	358	4.5
G3-S4	464	4.9
Reservoir-S3	301	3.8
Reservoir-S2	306	3.8
S2-G2	212	3.5
G2-G1	1247	12.1
G1-S1	1332	11.5

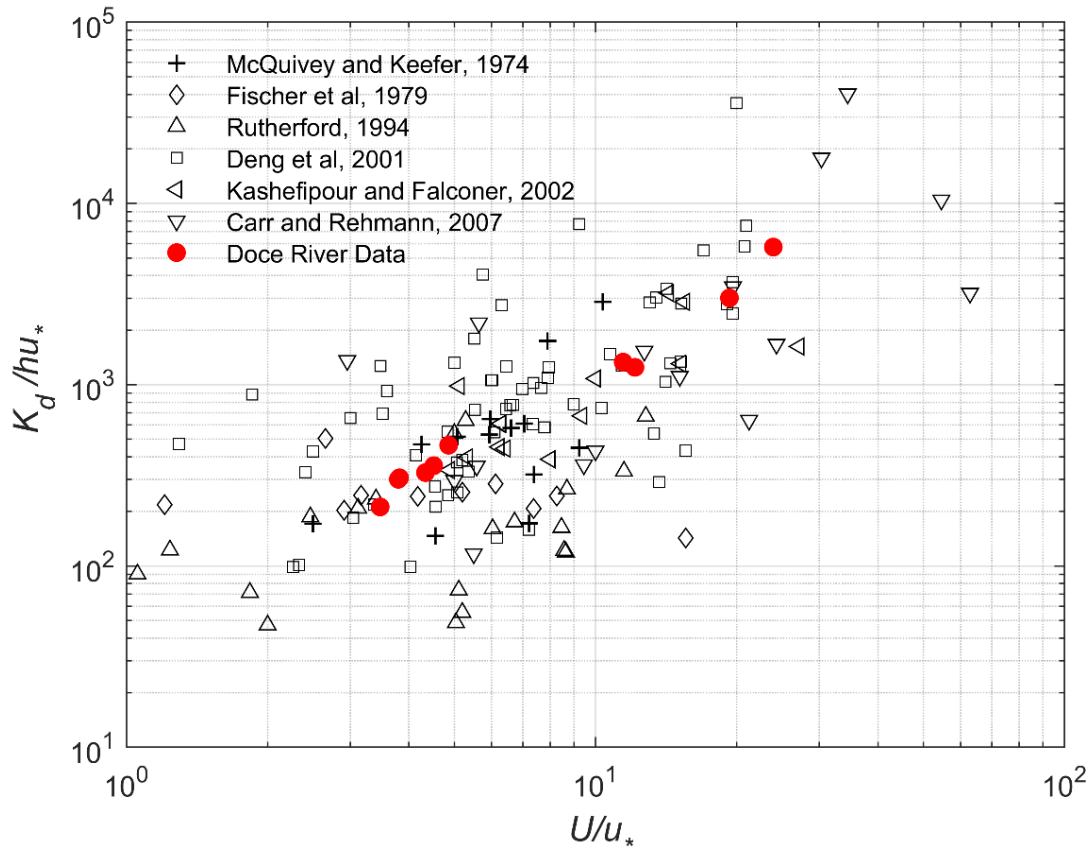


**Figure 4.10 – Comparison between the longitudinal dispersion coefficients presented in the literature and the Doce River data (McQuivey & Keefer, 1974; Fischer et al., 1979; Rutherford, 1994; Deng, Singh, & Bengtsson, 2001; Kashefipour & Falconer, 2002; Carr & Rehmann, 2007).**

The observed values of  $K_d$  in the Doce River varied from 30 m<sup>2</sup>/s to 120 m<sup>2</sup>/s showing the same trend and presenting good agreement with the data in the literature.

To define the most representative empirical expression for the modeling of longitudinal dispersion coefficient, each expression presented previously in Table 2.4 was tested using the Doce River and the literature data. As presented in Equation 2.35, most of the empirical expressions are functions of the dimensionless parameters: longitudinal dispersion coefficient over the product of flow depth and shear velocity ( $K_d/hu_*$ ), mean flow velocity over shear velocity ( $U/u_*$ ) and the river width over flow depth ( $W/h$ ). Thus, Figure 4.11 shows the plot of all the empirical equations as function of these parameters considering  $W/h \cong 66$ , which is the average of the literature data. Figure 4.12 presents the same plot taking into account the Doce River average value of  $W/h \cong 500$ . Finally, Table 4.5 presents the result of comparison of all expressions with the Doce River and literature data applying the statistical methods presented in Section 2.7.5.

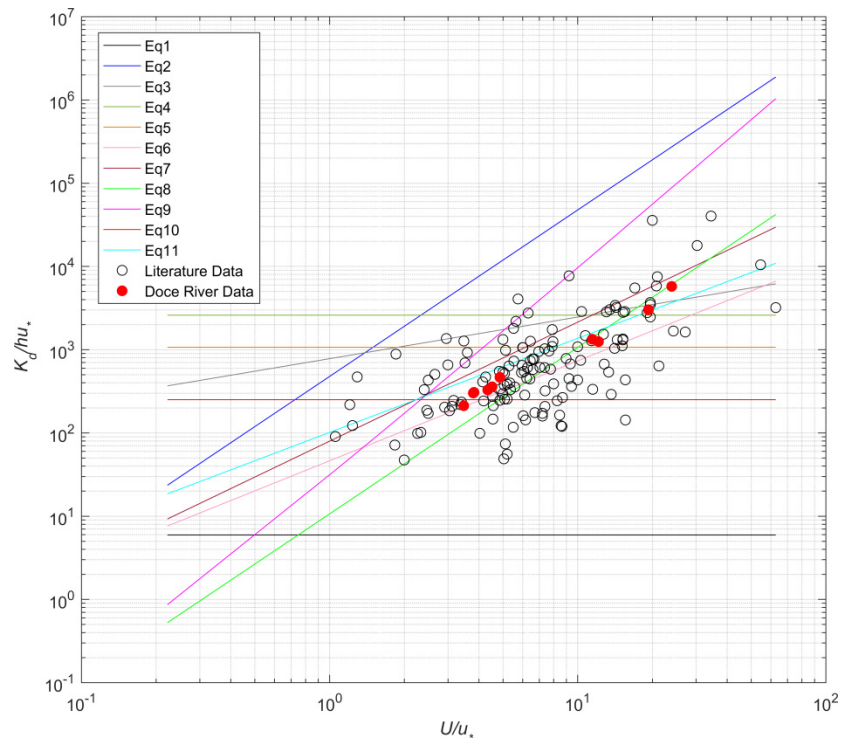


**Figure 4.11 – Comparison between the longitudinal dispersion coefficients presented in the literature and the Doce River data with  $W/h = 66$ .**

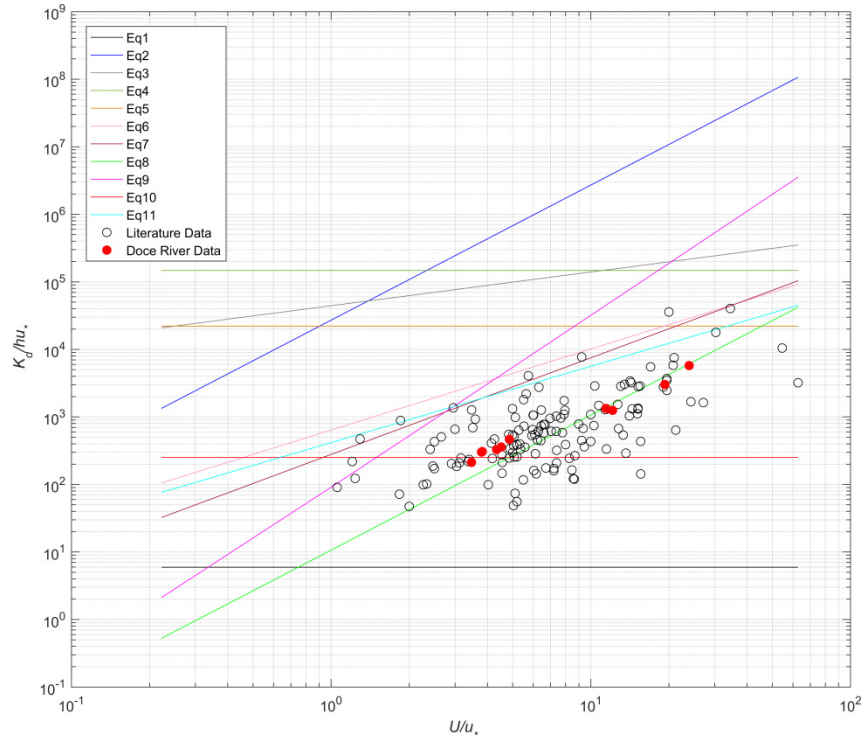


Figure 4.12 – Comparison between the longitudinal dispersion coefficients presented in the literature and the Doce Rive data with  $W/h = 500$ .

Table 4.5 – Evaluation of the empirical expressions for the longitudinal dispersion coefficient

ID	Equation	$W/h \cong 500$			
		DR <sub>s</sub>	R <sup>2</sup>	ME	RMSE
1	$K_d = 5.93hu_*$	-2.03	0.05	125	0.17
2	$K_d = 0.011U^2W^2/hu_*$	3.41	0.46	382868	0.28
3	$K_d = 0.18(U/u_*)^{0.5}(W/h)^2hu_*$	2.35	0.23	16456	0.20
4	$K_d = 0.6(W/h)^2 hu_*$	2.46	0.05	21743	0.21
5	$K_d = 2.0(W/h)^{1.5} hu_*$	1.62	0.05	3139	0.14
6	$K_d = 0.2(U/u_*)^{1.2}(W/h)^{1.3}hu_*$	1.07	0.39	1030	0.09
7	$K_d = 5.92(U/u_*)^{1.43}(W/h)^{0.62}hu_*$	0.89	0.42	757	0.08
<b>8</b>	<b><math>K_d = 10.612(U/u_*)hU</math></b>	<b>-0.08</b>	<b>0.46</b>	<b>91</b>	<b>0.04</b>
9	$K_d = [7.428 + 1.775(W/h)^{0.62}(U/u_*)^{0.572}](U/u_*)hU$	1.34	0.44	5722	0.12
10	$K_d = 250hu_*$	-0.37	0.05	108	0.06
11	$K_d = 5.4(U/u_*)^{0.13}(W/h)^{0.7}hU$	0.81	0.38	513	0.08

From the observation of Figure 4.11 and Figure 4.12 it is noticeable that when the ratio  $W/h$  is increased above the average of the literature data, several expression result in overestimation of  $K_d$ .

Nevertheless, the result of the statistical methods presented in Table 4.5 shows that the empirical expressions derived by Kashefipour and Falconer (2002) best fitted the literature and the Doce River data. This expression is given by Equation 4.4.

$$K_d = 10.612(U/u_*)hU \quad (4.4)$$

Equation 4.4 will be retained for further modeling of the suspended sediment propagation.

#### 4.5 Sediment Settling Rate

The settling rate is a relatively new parameter on literature, depending on the fall velocity of a specific particle size. The determination of the representative diameter for the settling rate observed in the Doce River was evaluated by the application of Equation 2.30, considering the average flow depth. The result is shown in Table 4.6.

**Table 4.6 – Settling rate evaluation from the Doce River measurements**

Reach	Observed Water Temperature (°C)	Fall Velocity $\omega$ (mm/s)	Settling Rate $k$ (day <sup>-1</sup> )	Dimensionless Diameter $d_*$	Particle Size $d_s$ (μm)
G6-G5	30	0.0026	0.33	0.04	1.5
G5-Reservoir	27	0.0017	0.33	0.03	1.3
Reservoir-G4	30	0.0045	0.29	0.06	2.0
G4-G3	30	0.0044	0.28	0.06	2.0
G3-S4	31	0.0037	0.28	0.05	1.8
Reservoir-S3	29	0.0014	0.11	0.03	1.1
Reservoir-S2	29	0.0014	0.11	0.03	1.1
S2-G2	29	0.0018	0.11	0.04	1.3
G2-G1	29	0.0022	0.21	0.04	1.4
G1-S1	29	0.0021	0.21	0.04	1.4

According to the analysis, the representative diameters of the settling rate varied from 1.1 to 2 μm, which classifies the sediment as medium clay. This result is remarkably consistent along Doce River reaches and denotes that the observed sediment settling rates are clearly associated with the slimes (finer stored tailings) of the Fundão Dam, which remained in suspension and sustained high turbidity levels in the river. One should note that the fall velocity of fine material is substantially affected by the temperature (Julien, 2010).

Figure 4.14 illustrates the particle diameter correspondent to the settling rate in the Doce River stations compared with the particle size distribution of the material stored at Fundão Dam. By this comparison one can conclude that the sediment settling rate observed in the Doce River corresponds approximately to  $d_{15}$  of the slimes ( $1.5 \mu\text{m}$ ) stored at the Fundão Dam.

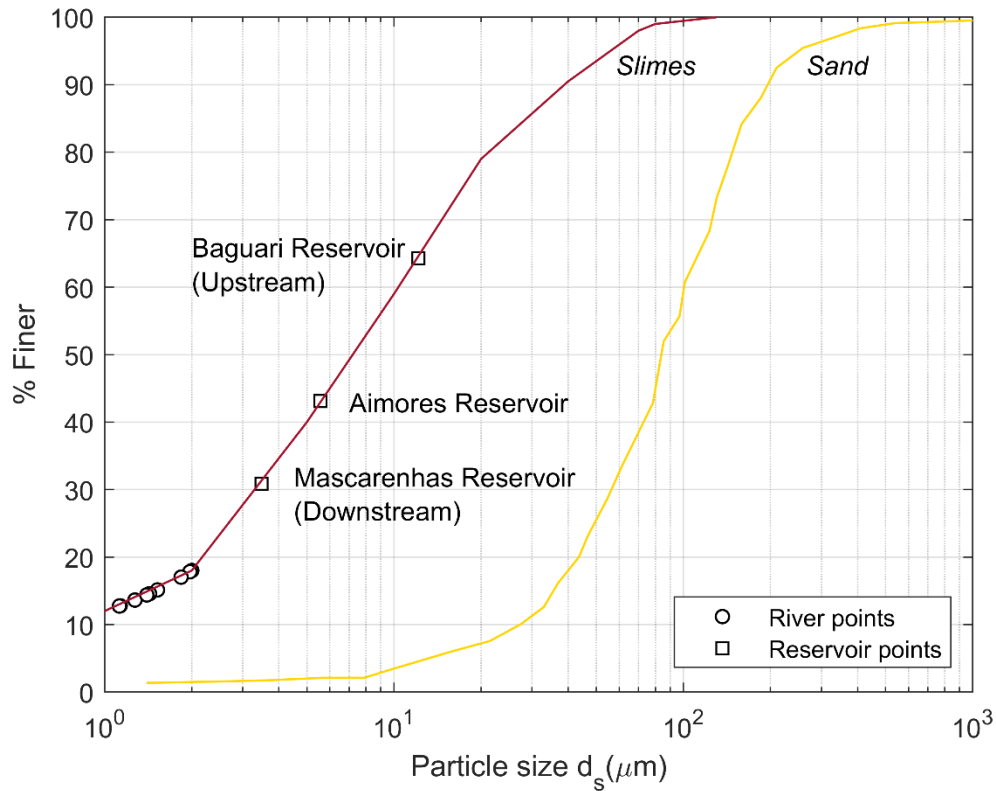


**Figure 4.13 – Comparison of the particle size distribution of the material stored in the Fundão Dam reservoir and the particle size related with the settling rate observed in the Doce River and in the reservoirs**

In the Doce River hydropower reservoirs the determination of the representative settling rate particle size is carried out applying Equation 2.44. This calculation takes into account the observed sediment concentration data upstream and downstream of the reservoirs and assumes that the water temperature is equal to the mean temperature observed on river reaches upstream and downstream of the reservoirs.

Table 4.7 presents a summary of the parameters for the sediment routing in the reservoirs, including the settling rate and the representative particle size  $d_s$ . The last column presents the  $d_{50}$  of the particle size distribution curve observed in the station upstream of each reservoir.

**Table 4.7 – Settling rate and representative particle size in the Doce River reservoirs**

Reservoir	Extension ( <i>km</i> )	$U$ ( <i>m/s</i> )	Depth ( <i>m</i> )	$T$ (°C)	$\omega$ ( <i>mm/s</i> )	$k$ ( <i>day</i> <sup>-1</sup> )	Representative size $d_s$ ( $\mu$ <i>m</i> )	$d_{50}$ Observed upstream ( $\mu$ <i>m</i> )
Baguari	22	0.25	10.0	28.5	0.16	1.39	12.1	17.9
Aimorés	32	0.10	5.5	30	0.04	0.55	5.6	7.4
Mascarenhas	10	0.11	5.0	29	0.01	0.23	3.5	4.0

The representative settling rate observed in the reservoirs relates with particle diameter slightly finer to  $d_{50}$  of the observed particles upstream of each reservoir. Furthermore, one can realize that the particle size decreased from Baguari Dam (upstream) to Mascarenhas Dam (downstream).

Since the same settling rate is applicable in the river and in the reservoirs, it is possible to define the settling rate as function of the dimensionless parameter  $kh/U$ , as presented in Table 4.8. Additionally, Figure 4.14 illustrates the relationship between the particle size and the dimensionless parameter obtained for the Doce River reaches and for the reservoirs.

**Table 4.8 – Dimensionless parameter and particle size observed in the Doce River and in the reservoirs**

River Reach	$k$ ( $day^{-1}$ )	Particle Size $d_s$ ( $\mu m$ )	$10^6 \frac{kh}{U}$
G6-G5	0.33	1.5	2.3
G5-Reservoir	0.33	1.3	1.5
Reservoir-G4	0.29	2.0	12.9
G4-G3	0.28	2.0	11.8
G3-S4	0.28	1.8	10.1
Reservoir-S3	0.11	1.1	4.0
Reservoir-S2	0.11	1.1	4.0
S2-G2	0.11	1.3	4.9
G2-G1	0.21	1.4	4.3
G1-S1	0.21	1.4	4.5
<b>Reservoirs</b>			
Baguari	1.39	12.1	651.2
Aimorés	0.55	5.6	348.6
Mascarenhas	0.23	3.5	115.7

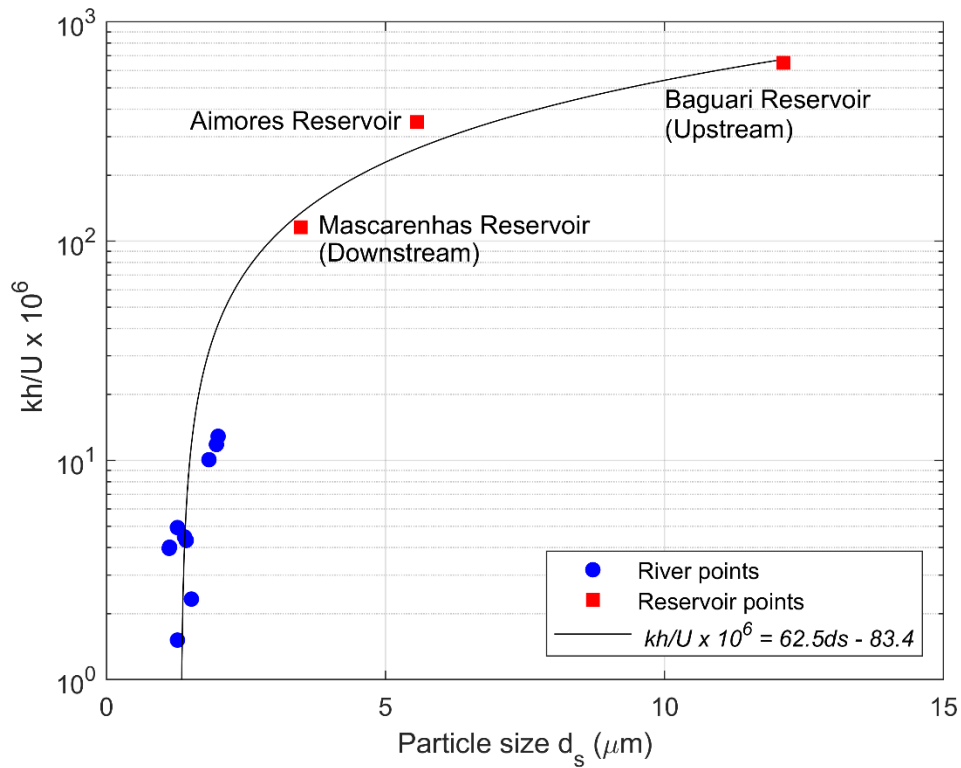


**Figure 4.14 – Dimensionless settling parameter as function of the particle size**

According to the measurements in the Doce River, the relationship between the dimensionless parameter  $kh/U$  and the representative particle size  $d_s$  in  $\mu m$  is expressed as Equation 4.5:

$$10^6 \frac{kh}{U} = 62.5d_s - 83.4 \quad (4.5)$$

One should note that the Equation 4.5 fits the data for particle size ranging from 1.1  $\mu m$  to 12.1  $\mu m$

#### 4.6 Volume of Sediment Trapped in the Doce River Reservoirs

Table 4.9 presents the reservoir operation data from the Reservoir Monitoring System from the National Water Agency (ANA, 2016c), the sediment inflow volume in the Candonga Dam reservoir estimated by the Brazilian agencies (IBAMA, 2016) and the calculated sediment inflow for the other three reservoirs estimated from the observed sediment concentration in the Doce River.

**Table 4.9 – Doce River reservoirs data and trap efficiency after the Fundão Dam collapse**

Reservoir	Mean Discharge (m <sup>3</sup> /s)	Water Level (masl)	Reservoir Area (km <sup>2</sup> )	Inflow Volume of Sediment (Mm <sup>3</sup> )	Outflow Volume of Sediment (Mm <sup>3</sup> )	Trap Efficiency (%)
Candonga	800	325.00	2.49	11.80	4.80	≈60
Baguari	215	184.68	3.40	2.47	0.55	≈80
Aimorés	196	89.61	31.57	0.15	0.04	≈70
Mascarenhas	236	59.60	3.90	0.04	0.03	≈20

Analysis of the trapped volume in the reservoirs was verified using two different approaches: the volume calculation using the observed data upstream and downstream of the reservoirs (sediment concentration and water discharge) and the calculation by size fraction, as described in Section 2.8. For this last procedure, the observed particle size distribution in the upstream stations was used.

For the specific case of the Candonga Dam, a combined particle size distribution of the material stored in Fundão Dam (Figure 3.22) is employed, this distribution is composed by 50% of sand and 50% of slimes. The comparative result for the two methodologies is presented in Table 4.10 and in Figure 4.15.

**Table 4.10 – Calculation of the trapped sediment in the Doce River reservoirs**

Reservoir	Volume of Sediment Trapped (Mm <sup>3</sup> )	
	Based on field measurements	Calculation by size fraction
Candonga	7.00	7.95
Baguari	1.92	1.83
Aimorés	0.11	0.14
Mascarenhas	0.01	0.02

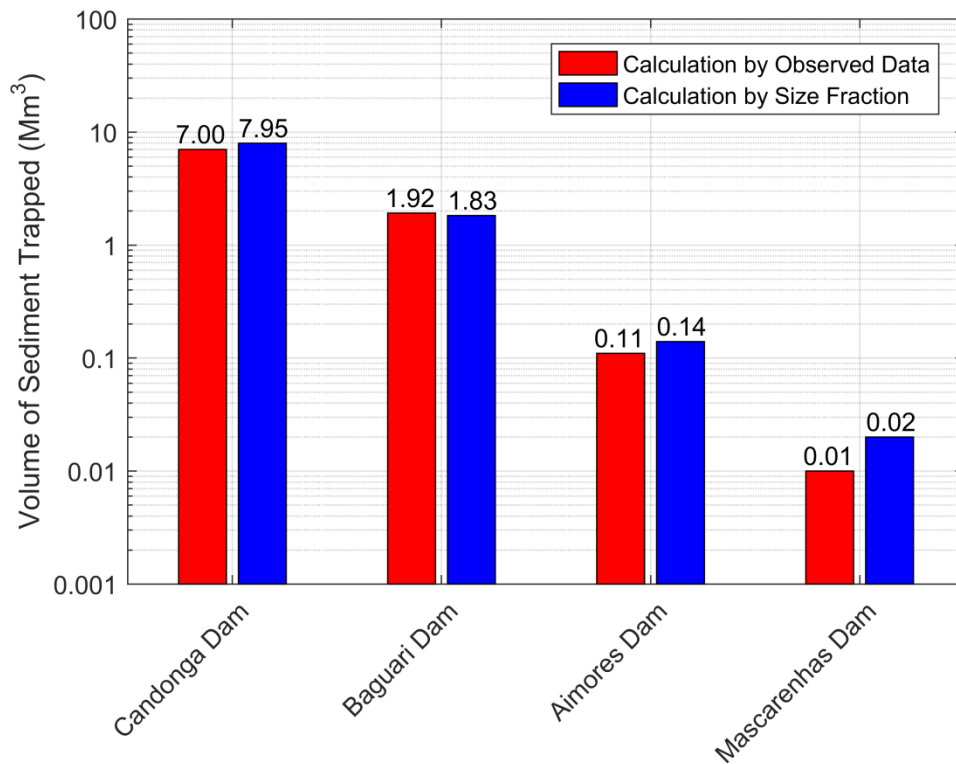


**Figure 4.15 – Comparison between the total volume trapped in the Doce River reservoirs using two different procedures**

Overall, there was good agreement between the two procedures. The biggest difference is in the Mascarenhas Dam, where only the finer sediment arrived ( $d_{50} = 5 \mu m$ ). Thus, in this specific case the calculation by size fraction resulted in an overestimation of the trapped sediment. Lastly, Table 4.11 presents the estimated reservoir volume loss after the Fundão Dam collapse.

**Table 4.11 – Estimate of reservoir volume loss after the Fundão Dam collapse.**

Reservoirs	Total Volume (Mm <sup>3</sup> )	Volume Loss
Candonga	42.2	17%
Baguari	38.1	5%
Aimorés	249.2	0.04%
Mascarenhas	23.9	0.04%

According to Table 4.11, the volume loss in Candonga Dam reservoir immediately after the Fundão Dam failure was 17%. However, as registered by the Brazilian Institute of Environment and Renewable Natural Resources, at the end of February due to rains in the region, the total sediment trapped in the Candonga Reservoir was 9.5 Mm<sup>3</sup>, increasing the volume loss to 22.5%. Remarkably, the event of the Fundão Dam collapse resulted in substantial volume loss in the Candonga Dam, because almost one quarter of the reservoir volume was consumed. At present, efforts have been made to dredge 2 Mm<sup>3</sup> and recover part of the reservoir volume. The restart of the hydropower operation is expected only to 2020 (Renova, 2018).

#### 4.7 Observed Difference between the Floodwave and Sediment Transport Propagation

As registered by the Brazilian agencies, during the field survey a lag between the flood and the sediment peak concentration was detected. Figure 4.16 presents the plot of the peak discharges and the peak of sediment concentration as function of distance and time, using the Fundão Dam site and the time of failure as the origin of the coordinates.

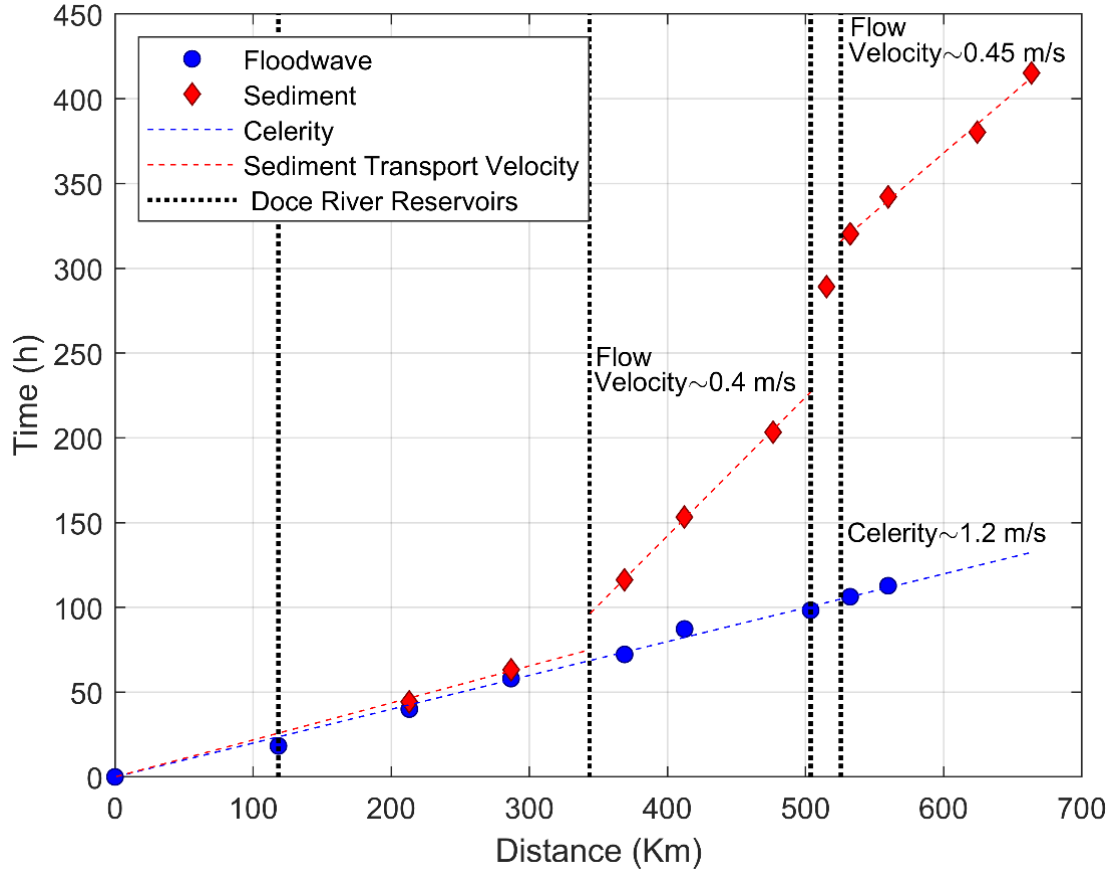


**Figure 4.16 – Comparison between the floodwave celerity and sediment velocity in Doce River**

The lag between the flood and sediment concentration has its origin at the first reservoir of Doce River (Candongia Dam), which delayed the sediment propagation. Furthermore, the same situation occurred in the river reaches downstream, where the interruption in the vertical dashed line indicates the time spent by the sediment to cross the reservoirs. Another effect observed was the difference between the floodwave celerity and the flow velocity, as explained in Equation 2.15. Ultimately, the sediment arrived in the sea approximately 13 days after the floodwave.

#### 4.8 Conclusions

The collapse of Fundão Dam spilled 32 Mm<sup>3</sup> of tailings in the Doce River basin, however approximately 90% of this material was trapped up to 118 km downstream of the dam, upstream of the Candonga hydropower reservoir. Nevertheless, the remaining material that arrived in the Doce River resulted in high concentration (maximum measured approximately 400,000 mg/l), with suspension as the primary mode of sediment transport.

The result of application of the analytical solution for the one-dimensional advection-dispersion equation using the complementary error function agrees with the observed sediment concentration. This procedure enabled the calibration of the equation parameters, i.e., the longitudinal dispersion coefficient and the sediment settling rate. The values determined for the longitudinal dispersion coefficient ranged from 30 to 120 m<sup>2</sup>/s, fitting the literature data. Among the existent empirical expressions for the calculation of this coefficient the equation developed by Kashefipour and Falconer (2002) presented the best agreement with both the literature and the Doce River data. In addition, the sediment settling rate observed along the whole river could be related with the finer material stored in Fundão Dam, where the particle size ranged from 1.1 to 2  $\mu\text{m}$ .

The data analysis carried out also indicated that immediately after the Fundão Dam collapse the Candonga hydropower reservoir lost approximately 17% of its volume, while the Baguari Dam (second reservoir in the Doce River) lost approximately 5% of its volume. The volume loss in the other two reservoirs was insignificant. Finally, the observed lag between the sediment transport (finer tailings) and the floodwave propagation along the Doce River could be primarily attributed to the interference of the hydropower reservoirs.

## 5. FLOOD ROUTING MODEL

### 5.1 Introduction

A numerical simulation of the physical processes in the Doce River and reservoirs after the Fundão Dam collapse requires the subdivision of fluvial reaches and reservoirs, as illustrated in Figure 5.1.

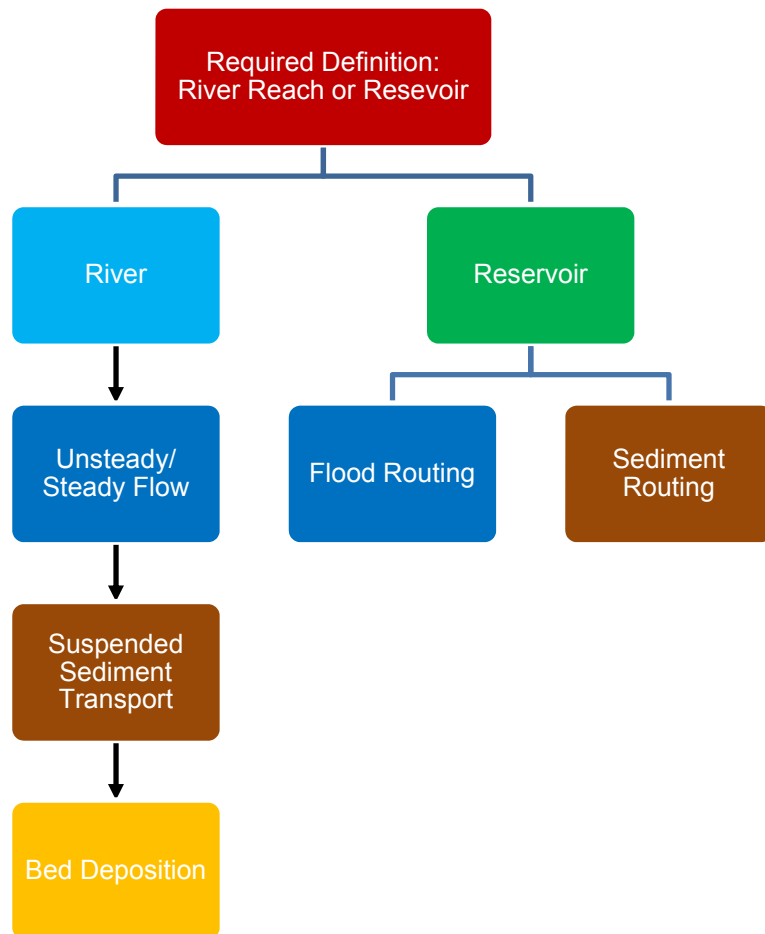


**Figure 5.1 – Processes in the numerical simulation**

Thus, a hydrodynamic one-dimensional numerical model is proposed to simulate both the unsteady and steady state flow regimes along the Doce River and its reservoirs.

The objective of this model is to provide the flow conditions for a later simulation of sediment transport. Table 5.1 presents the physical processes to simulate the flow and the corresponding equations or methods used, presented earlier in Chapter 2.

**Table 5.1 – Physical process and equations applied on the flow simulation along the Doce River**

Physical Process	Equation/Method
Dam Break Hydrograph	Envelope Curve (Rico et al., 2007)
Unsteady Flow	Momentum
	Continuity
Steady Flow	Standard Step Method
Reservoir Routing	Level Pool Routing

To simplify the simulation, the path of the floodwave and sediment transport was divided in five reaches, with four of them in the Doce River as presented in Figure 5.2.

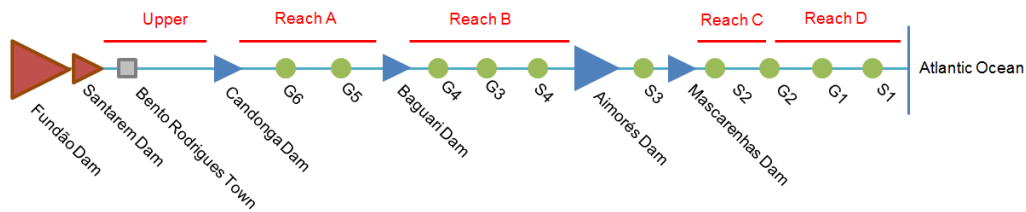


**Figure 5.2 – River reaches division for the numerical simulation**

The Upper Reach relates to the Gualaxo do Norte and Carmo Rivers, located upstream of the Candonga Dam, while the Reaches A, B, C and D correspond to the Doce River. Table 5.2 shows the length, average slope and average width of each reach.

**Table 5.2 – River reaches**

Reach	Length (km)	Slope	Width (m)
Upper	110	0.005	30
A	204	0.0005	200
B	128	0.0005	380
C	34	0.0008	620
D	108	0.0002	730

The next sections present the assumptions, the numerical methods applied, the calibrated parameters and the results of the numerical simulation.

## 5.2 Upper Reach Simulation

This research is focused on the floodwave and sediment propagation along the Doce River following the accident with the Fundão Dam. However, the Upper Reach simulation is needed to provide the upstream boundary conditions (hydrograph and sediment concentration) at the Candonga Dam for a subsequent simulation of the Doce River flow.

Initially, the discharge peak after the dam collapse can be estimated using Equation 2.20. Thus, considering the total released volume of  $56 \text{ Mm}^3$  (tailings plus water) and the dam high equal to 120 m, one can obtain:

$$Q_{max} = 325(56 \times 120)^{0.42} \cong 13,000 \text{ m}^3/\text{s} \quad (5.1)$$

The dam break hydrograph is assumed to have a triangular shape, therefore the base time of the hydrograph is equal to 2.4 hours. Moreover, the flood simulation downstream of Fundão Dam must consider the resistance effects of the hyperconcentrated flow, in which the water and sediment travel together. One should also consider that sediment deposition on the bed and floodplain along the Gualaxo do Norte and Carmo Rivers results in the reduction of the hydrograph volume as it moves forward.

A simplified model of the unsteady flow resultant of the dam collapse can be made using the diffusive wave format of the Saint Venant equations without any substantial loss of accuracy (O'Brien et al., 1993). Furthermore, a settling term can be added to simulate the reduction of the hydrograph volume due the sediment deposition. Thus, the diffusive wave equation becomes Equation 5.2:

$$\frac{\partial Q}{\partial t} + C_e \frac{\partial Q}{\partial x} = D \frac{\partial^2 Q}{\partial x^2} - k_* Q \quad (5.2)$$

Where  $k_*$  is the settling rate applied on the propagation of the hyperconcentrated flow. Due to transport format, Equation 5.2 can be solved using the Crank Nicolson scheme. This simplified equation incorporates the additional flow resistance of the hyperconcentrated flow through the celerity  $C_e$  and the hydraulic diffusivity  $D$ .

The settling rate was calibrated to reduce the dam break hydrograph ( $56 \text{ Mm}^3$ ) to the same volume as observed in the Doce River ( $24 \text{ Mm}^3$ ). Moreover, the floodwave attenuation (hydraulic diffusivity  $D$ ) and the floodwave speed  $C_e$  were calibrated to match the observed time of arrival and discharge peak at Candonga Dam (CPRM & ANA, 2015a; Tschiedel, 2016). Thus, considering the difference between the time of the collapse and the time of the arrival of the floodwave in Candonga Dam (07:00 on 11/06/2015), the average floodwave celerity on the upper reach after the Fundão Dam collapse resulted approximately 1.8 m/s. This value has the same magnitude of the celerity observed ( $\approx 2\text{m/s}$ ) after the collapse of the Los Frailes Tailings Dam in Spain, as registered in a gaging station located 11 km downstream of that dam (Ayala-Carcedo, 1998). This is one of the few celerity data registered in the literature after a tailings dam failure.

For the numerical simulation, the spatial discretization and the time steps adopted were respectively  $\Delta x = 250 \text{ m}$  and  $\Delta t = 300 \text{ s}$ . A check of grid dependence i.e., a successive refinement of an initial coarse grid (Versteeg & Malalasekera, 2007), showed that there was no improvement in the results for a refined mesh but considerable increase in the processing time. The result of the calibration is presented in Table 5.3

**Table 5.3 – Floodwave simulation parameters**

Reach	Length (km)	$\Delta x$ (m)	$\Delta t$ (s)	$C_e$ (m/s)	$D$ ( $\text{m}^2/\text{s}$ )	$k_*$ ( $\text{day}^{-1}$ )	$C_a$	$C_d$	$P_\Delta$
Upper	110	250	300	1.78	600	1.26	2.13	2.88	0.74

Figure 5.3 shows the calculated propagation of the floodwave in the Upper Reach of the Doce River basin.

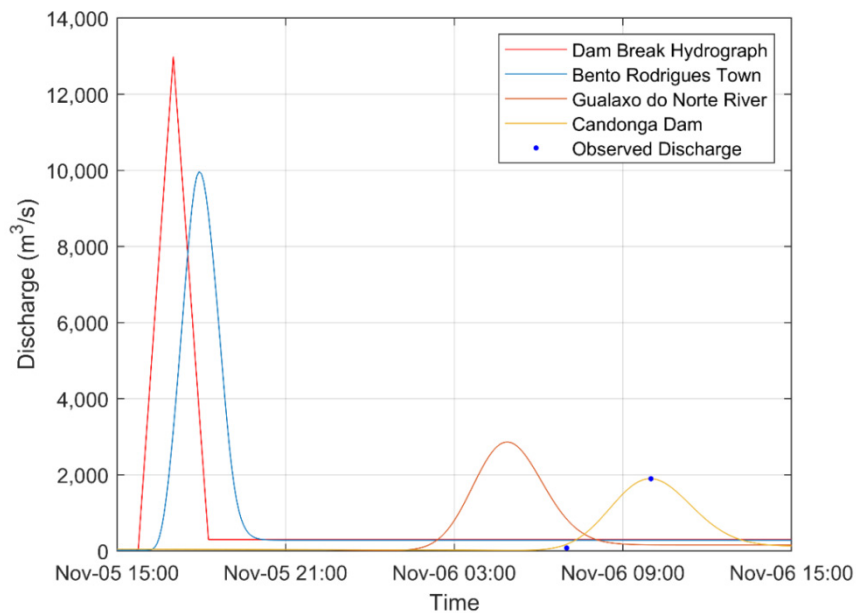


**Figure 5.3 – Floodwave simulation at the Upper Reach**

One should note that the hydrograph obtained at Candonga Dam has an hourly Richard-Baker Flashiness Index equal to 0.47, which is approximately 25 times higher than for natural floods in the same river. This hydrograph will be the upstream boundary conditions at the Doce River, as presented in the next section.

### 5.3 Evaluation of Flood Routing Methods on the Doce River

The flood routing methods presented in Table 2.2 were tested along the Doce River using the calculated hydrograph at Candonga Dam as upstream boundary condition. The objective was to reproduce the flow conditions for a further simulation of the sediment transport. The methods were tested in the first Doce River reach (Reach A) between Candonga and the station G6 (upstream) and between the station G6 and the Baguari reservoir (downstream). In this reach, the average river width is 200 m and the bed slope is 0.0005. The simulations carried out were:

- A. Modified Puls in HEC-RAS\* - hydrologic routing;
- B. Muskingum-Cunge - hydrologic routing coded in Matlab\*\*;
- C. Preissmann scheme - full dynamic wave routing (non-linear equation solved using the Newton-Raphson method), coded in Matlab\*\*;
- D. HEC-RAS\* - full dynamic wave routing (Preissmann scheme solved through linear equations);
- E. Crank Nicolson scheme - diffusive wave routing coded in Matlab\*\*;
- F. QUICKEST scheme - diffusive wave routing coded in Matlab\*\*;

\*The HEC-RAS version 5.0.6 was used.

\*\*The Matlab version R2018a was used.

The initial estimate of the cross section distance  $\Delta x$  followed the empirical expressions provided in the HEC-RAS Reference Manual (USACE, 2016). Accordingly, it should be smaller than:

$$\Delta x \leq \frac{0.15Y}{S_o} \quad (5.3)$$

Where  $Y$  is the average main channel bankfull depth in m. A second equation to estimate  $\Delta x$  is:

$$\Delta x \leq \frac{C_e T_r}{20} \quad (5.4)$$

Where  $C_e$  is the celerity in m/s and  $T_r$  is hydrograph rising time (from low flow to peak) in seconds. The most restrictive value is then determined as the minimum distance  $\Delta x$ . Additionally, an initial guess to wave celerity can be done by the Kleitz-Seddon [Equation 2.16].

$$C_e = \frac{\partial Q}{\partial A} \approx \frac{\Delta Q}{\Delta A} \quad (2.16)$$

Moreover, a practical time step  $\Delta t$  for medium to large rivers is given by Equation 5.5 (USACE, 2016):

$$\Delta t \leq \frac{T_r}{20} \quad (5.5)$$

The expressions presented above can be used as an initial mesh size, however, it does not replace the check of the effects of the refinement of the grid on the solution. Thus, the initial definition of the mesh size followed the recommendations presented in the HEC-RAS User's Manual. Nevertheless, the final mesh size selected for all schemes was  $\Delta x = 250$  m and  $\Delta t = 300$  s, since no improvements were observed with more refinements. The Manning's roughness coefficient was calibrated to fit the observed hydrograph downstream. Table 5.4 presents the simulation parameters while Figure 5.4 and Figure 5.5 shows the results of the flood routing simulations.

**Table 5.4 – Summary of parameters applied on the flood routing simulations on Reach A**

Parameter	Reach A	
	Upstream	Downstream
$L$ (km)	95	109
$n$	0.05	0.048
$Y$ (m)	6	6.5
$Tr$ (h)	3	8.5
$C_e$ (m/s) – initial guess	2	1.3
$\theta$ – Preissmann	1	1
Diffusive wave models		
$Q_{ref}$ (m <sup>3</sup> /s)	980	470
$D$ (m <sup>2</sup> /s)	4,700	2,250
$C_e$ (m/s)	1.2	1.2

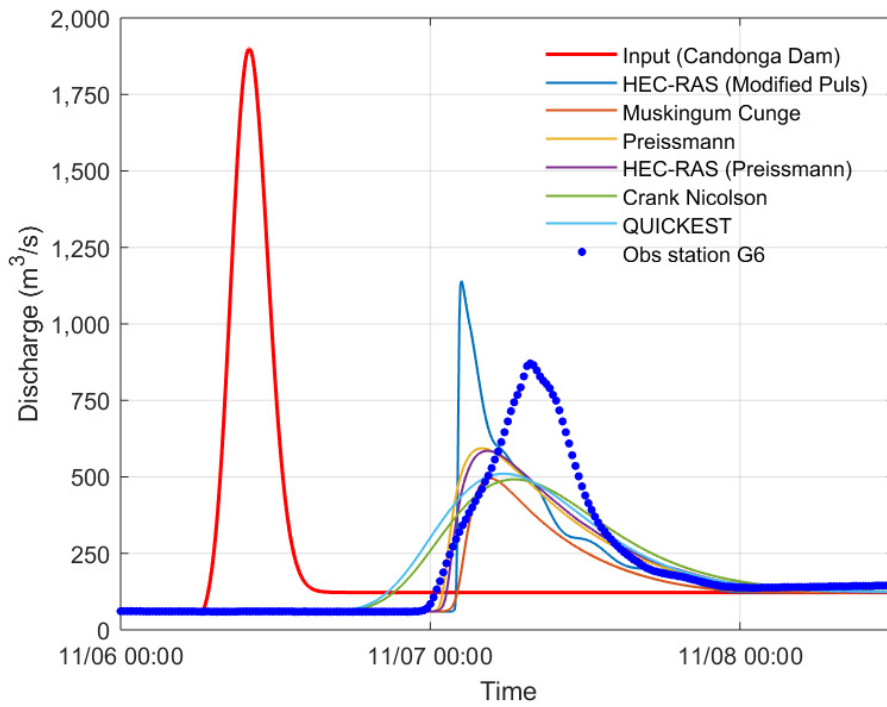


Figure 5.4 – Test of flood routing procedures, Reach A upstream (Candonga Dam – G6)

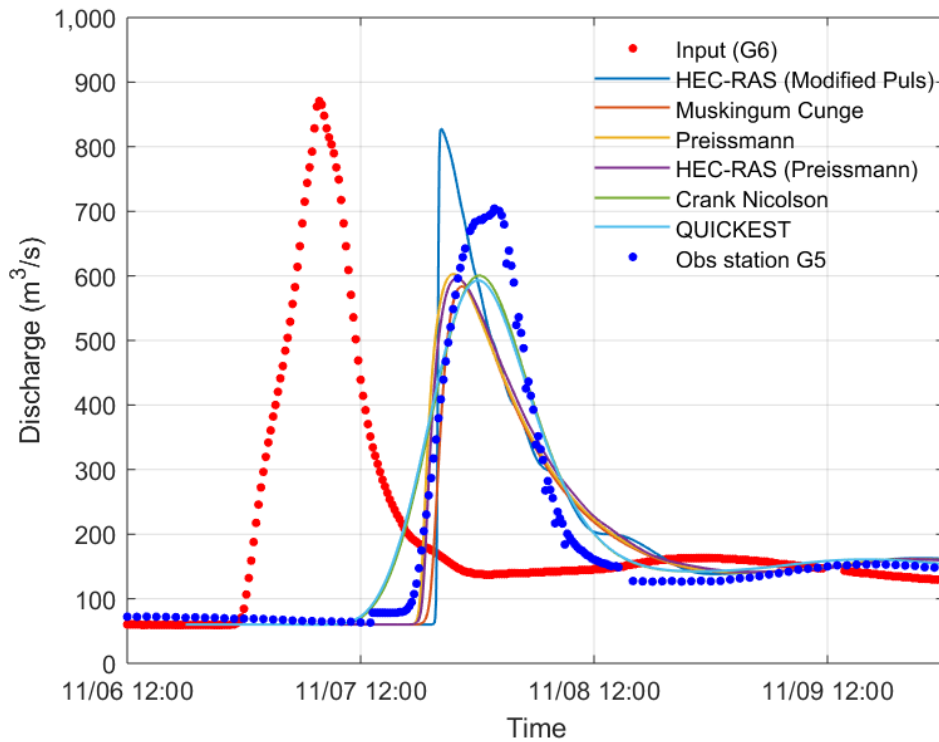


Figure 5.5 – Test of flood routing procedures, Reach A downstream (G6 – G5)

A quantitative comparison between the numerical simulations and the observed discharges is made by means of the relative percent difference (RPD) applied on the peak discharge, the root mean square error (RMSE), the mean absolute percentage error (MAPE) and the difference on the time of peak, as presented in Table 5.5.

**Table 5.5 – Quantitative comparison between the flood routing models and the observed discharge on Reach A**

Simulations	Upstream					Downstream				
	Peak (m <sup>3</sup> /s)	RPD	RMSE (m <sup>3</sup> /s)	MAPE	Time diff (h)	Peak (m <sup>3</sup> /s)	RPD	RMSE (m <sup>3</sup> /s)	MAPE	Time diff (h)
Observed	871	-	-	-	-	704	-	-	-	-
Modified Puls*	1141	31%	216	29%	-5.3	828	18%	122	28%	-5.5
Muskingum Cunge	495	-43%	184	24%	-3.2	584	-17%	90	24%	-3.3
Preissmann	594	-32%	146	18%	-3.8	603	-14%	91	24%	-4.2
Preissmann*	585	-33%	138	18%	-3.3	596	-15%	85	24%	-3.8
Crank Nicolson	492	-44%	140	31%	-1.3	601	-15%	69	31%	-1.5
QUICKEST	510	-41%	145	32%	-2.1	593	-16%	74	33%	-1.7

\*Simulated in HEC-RAS version 5.0.6.

The commonly used flood routing methods were not able to simulate the observed flashy hydrographs in the mild slope of the Doce River. All these numerical methods, except for the Modified Puls, underestimated the peak discharge, with an error up to 44%. The application of the Modified Puls resulted in a spiky distorted hydrograph, overestimating the peak by 31% and resulting in a difference in peak timing of approximately 5 hours. The Muskingum-Cunge method showed a lowered peak, underpredicting the discharge peak by 43%. The Preissmann scheme, solved either by the non-linear approach in Matlab or using linearization techniques in HEC-RAS, smoothed the solution and depressed the peak 33%. The diffusive wave routing models (Crank Nicolson and QUICKEST) resulted in an over reduced hydrograph due the hydraulic diffusivity coefficient, which was overestimated by the formulation presented in literature [Equation 2.17].

For these last two approaches the uncertainty about the choice of the reference discharge was a caveat. The use of the mean discharge resulted in an inaccurate estimative of  $D$  and the discharge peak would have resulted in higher value of  $D$ , causing even more floodwave attenuation.

The unsatisfactory results of the tested routing methods motivated the search for a more accurate method to simulate the flashy hydrograph (25 times higher than for the observed natural floods) in a mild slope channel. Nevertheless, the one-dimensional advection-dispersion equation (diffusive wave approximation) could provide a better simulation of the translation and attenuation of the floodwave if the hydraulic diffusivity coefficient was estimated more precisely. Therefore, it was clear that there are two issues that should be addressed in the development of a better algorithm for flashflood propagation in rivers: (1) to include all terms of the Saint-Venant equation, contrasting the diffusive wave approximation presented here; and (2) to define the diffusivity coefficient  $D$  function of parameters with less variability than the rapidly-varied discharge.

#### 5.4 New Approach to Calculate Floodwave Propagation

Initially, the general form of the flow resistance relationship can be written as (Julien, 2018):

$$Q = W\alpha h^\beta \quad (5.6)$$

Where  $Q$  is the discharge,  $h$  is the flow depth and  $\alpha$  and  $\beta$  are parameters conditioned to the resistance coefficient chosen (Manning, Darcy Welsbach or Chezy). From Equation 5.6, the floodwave celerity can also be derived as a function of mean flow velocity as  $C_e = \beta U$ .

The full dynamic wave equation can be written as an equivalent diffusive wave format, as presented earlier in Equation 2.9:

$$S_f = S_o - [1 - (\beta - 1)^2 Fr^2] \frac{\partial h}{\partial x} \quad (2.9)$$

Therefore, the full dynamic wave can be reduced to:

$$S_f = S_o - \Omega \frac{\partial h}{\partial x} \quad (5.7)$$

Where  $\Omega$  is the floodwave diffusivity, given by:

$$\Omega = [1 - (\beta - 1)^2 Fr^2] \quad (5.8)$$

The addition of  $\Omega$  takes into account the terms neglected in the derivation of the diffusive wave approximation. The inclusion of terms IV and V of Equation 2.8 into Equation 5.7 can calculate the floodwave attenuation more accurately, mainly in flashy hydrographs. In addition, the conversion of Equation 5.7 into an advection-dispersion format initially considers the channel resistance and the continuity in a wide rectangular channel, respectively equal to:

$$Q = K \sqrt{S_f} \rightarrow S_f = \frac{Q^2}{K^2} \quad (5.9)$$

$$\frac{\partial h}{\partial t} + \frac{1}{W} \frac{\partial Q}{\partial x} = 0 \quad (5.10)$$

Thus, taking the space derivative of Equation 5.10 results in:

$$\frac{\partial^2 h}{\partial t \partial x} = - \frac{\partial^2 Q}{W \partial x^2} \quad (5.11)$$

The substitution of Equation 5.9 into Equation 5.7 followed by the application of time derivative and considering the relationship obtained in Equation 5.11 leads to:

$$\frac{\partial}{\partial t} \left( \frac{Q^2}{K^2} \right) = \Omega \frac{\partial^2 Q}{W \partial x^2} \quad (5.12)$$

Furthermore, one should note that:

$$\frac{\partial K}{\partial t} = \frac{\partial K}{\partial h} \frac{\partial h}{\partial t} = \frac{\partial K}{\partial h} \left( - \frac{1}{W} \frac{\partial Q}{\partial x} \right) \quad (5.13)$$

$$\frac{\partial K}{\partial h} = \frac{\alpha\beta Wh^{\beta-1}}{\sqrt{S_f}} \quad (5.14)$$

The substitution of Equation 5.13 into Equation 5.12 and a further expansion results in:

$$\frac{2Q}{K^2} \frac{\partial Q}{\partial t} - \frac{2Q^2}{K^3} \frac{\partial K}{\partial h} \left( -\frac{1}{W} \frac{\partial Q}{\partial x} \right) = \Omega \frac{\partial^2 Q}{W \partial x^2} \quad (5.15)$$

Then, substituting Equation 5.14 into Equation 5.15 and simplifying:

$$\frac{\partial Q}{\partial t} + \beta U \frac{\partial Q}{\partial x} = \frac{\Omega Q}{2WS_f} \frac{\partial^2 Q}{\partial x^2} \quad (5.16)$$

Where the modified hydraulic diffusivity coefficient  $D_M$  is equal to:

$$D_M = \frac{\Omega Q}{2WS_f} \quad (5.17)$$

Assuming the energy slope equal to the bed slope,  $D_M$  becomes:

$$D_M = \Omega D \quad (5.18)$$

The floodwave celerity  $C_e$  is given by Equation 2.14 presented previously:

$$C_e = \beta U \quad (2.14)$$

Finally, Equation 5.16 becomes:

$$\frac{\partial Q}{\partial t} + C_e \frac{\partial Q}{\partial x} = \Omega D \frac{\partial^2 Q}{\partial x^2} \quad (5.19)$$

However, as observed in the Doce River simulations, the choice of a reference discharge to calculate the hydraulic diffusivity coefficient was a limitation on the linear diffusive wave routing procedure. Definitely the discharge was not a proper parameter in the flashy hydrograph propagation, since it varies quickly both in time and space.

The new approach defines the hydraulic diffusivity coefficient as a function of the less variable parameters in a channel during a flood event. These parameters are the Froude number  $Fr$  and the floodwave celerity  $C_e$ . Bearing this in mind, the conveyance  $K$  in a wide rectangular channel is rewritten into the following form, considering the energy slope equal to the bed channel slope (i.e.  $K = Q/\sqrt{S_o}$ ):

$$K = \frac{\alpha W}{\sqrt{S_o}} \left( \frac{U^2}{Fr^2 g} \right)^\beta \quad (5.20)$$

Substitution of Equations 5.20 and 2.14 into Equation 5.18 with  $D = K/2W\sqrt{S_o}$  from Equation 2.17 leads to:

$$D_M = [1 - (\beta - 1)^2 Fr^2] \frac{\alpha}{2S_o} \left[ \frac{1}{g} \left( \frac{C_e}{\beta Fr} \right)^2 \right]^\beta \quad (5.21)$$

For the Manning's equation in S.I, the parameters of Equation 5.21 are:

$$\alpha = \frac{\sqrt{S_o}}{n}, \beta = \frac{5}{3} \quad (5.22)$$

Finally, the modified diffusivity coefficient from Equations 5.21 and 5.22 becomes:

$$D_M = \left[ \frac{(1 - 0.444Fr^2)}{2n\sqrt{S_o}} \right] \left( \frac{0.6C_e}{Fr\sqrt{g}} \right)^{10/3} \quad (5.23)$$

This newly derived modified hydraulic diffusivity coefficient  $D_M$  considers the full dynamic acceleration terms neglected in the derivation of diffusive wave form and it is function of parameters  $Fr$  and  $C_e$ , with relatively small variations in a channel during a flood event. This coefficient can be implemented through the linear diffusive models (Crank Nicolson and QUICKEST schemes). The test of these two schemes in the Doce River using the new derived modified hydraulic diffusivity coefficient is presented in the next section.

#### 5.4.1 Test of the New Approach on the Doce River

The application of Equation 5.23 on the Reach A of the Doce River was made using the mean Froude number, while the celerity was obtained by an iterative procedure to approximate the timing to peak. Simulation parameters are presented in Table 5.6 while the quantitative comparison of the new approach is presented in Table 5.7.

**Table 5.6 – Parameters applied on the flood routing simulations on Reach A using the new method**

Parameter	Reach A	
	Upstream	Downstream
$L$ (km)	95	109
$n$	0.05	0.05
$Fr$	0.18	0.18
$D$ (m <sup>2</sup> /s)	977	977
$Ce$ (m/s)	1.2	1.2

**Table 5.7 – Flood routing simulation with new approach, Reach A**

Simulations	Upstream					Downstream				
	Peak (m <sup>3</sup> /s)	RPD	RMSE (m <sup>3</sup> /s)	MAPE	Time diff (h)	Peak (m <sup>3</sup> /s)	RPD	RMSE (m <sup>3</sup> /s)	MAPE	Time diff (h)
Observed	871	-	-	-	-	704	-	-	-	-
Crank Nicolson	891	2.3%	47	13%	-0.1	716	1.7%	22	9%	-1.0
QUICKEST	854	-1.9%	39	11%	-0.1	682	-3.2%	29	12%	-0.9

The new method using both the Crank Nicolson and the QUICKEST scheme better fitted the observed data when compared with all the previous methodologies. It presented a maximum error decrease from 44% to 2 % for RPD, 216 m<sup>3</sup>/s to 39 m<sup>3</sup>/s for RMSE, and 32% to 11% for MAPE. The maximum difference found in time of peak was about 1 hour. The results of the new method are illustrated in Figure 5.6 up to Figure 5.9.

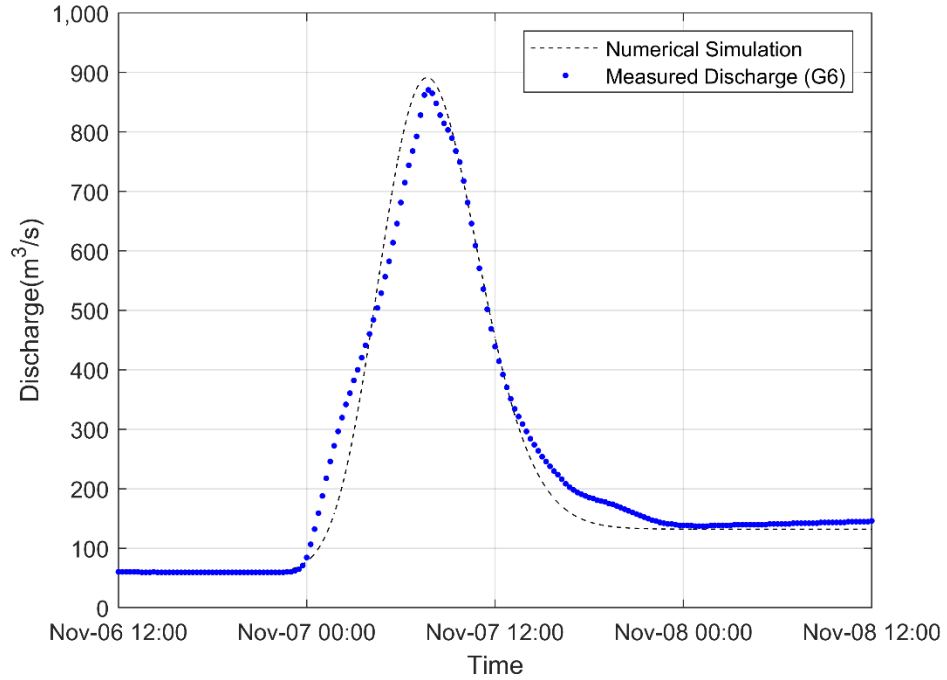


**Figure 5.6 – Application of the new hydraulic diffusivity coefficient on the Doce River reach using the Crank Nicolson scheme (Candonga Dam – G6)**

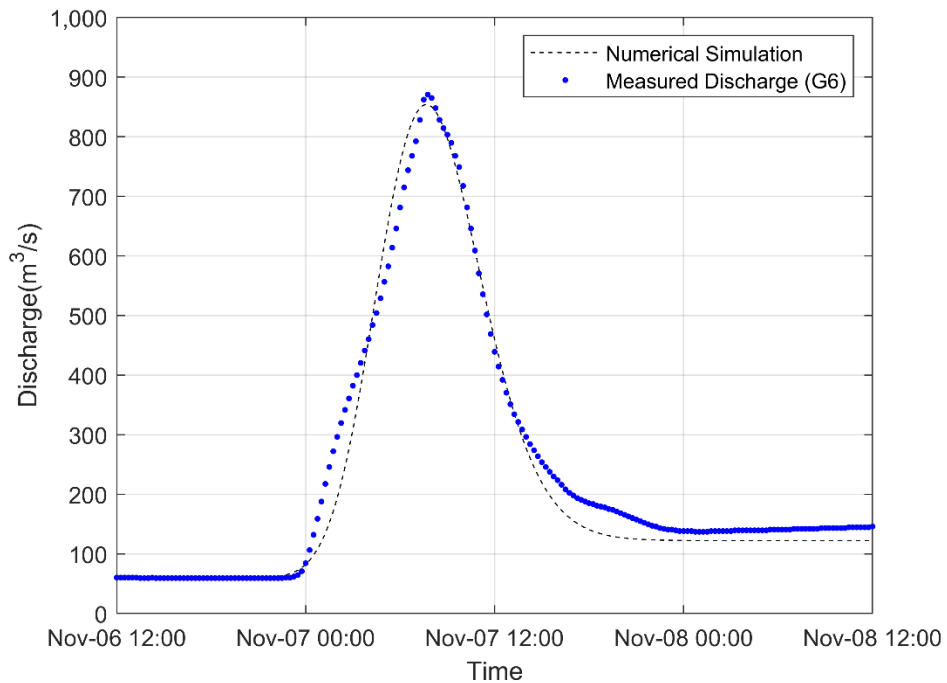


**Figure 5.7 – Application of the new hydraulic diffusivity coefficient on the Doce River reach using the QUICKEST scheme (Candonga Dam – G6)**

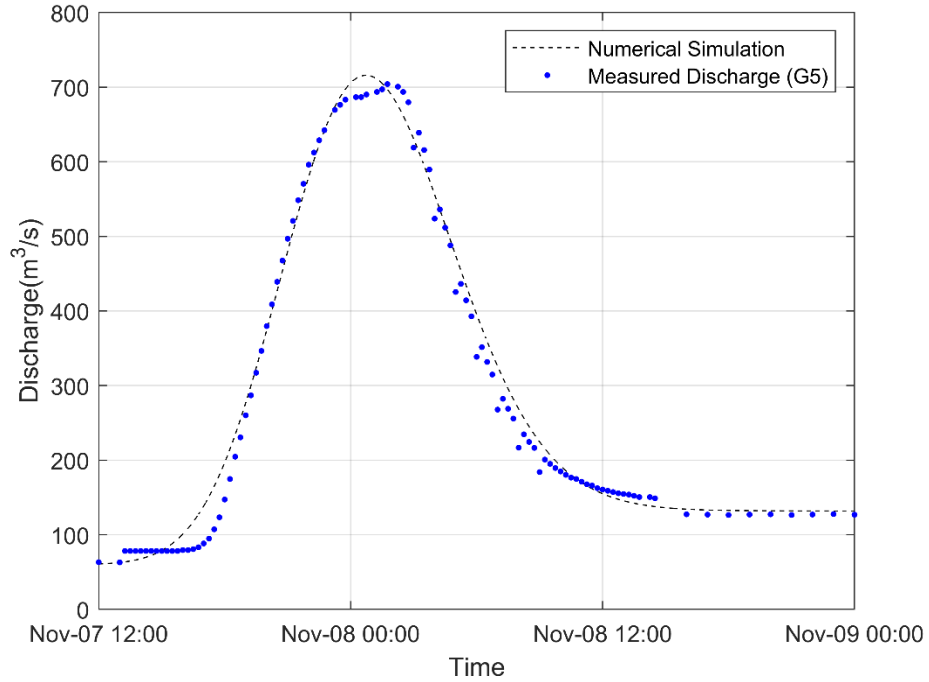


**Figure 5.8 – Application of the new hydraulic diffusivity coefficient on the Doce River reach using the Crank Nicolson scheme (G6 – G5)**

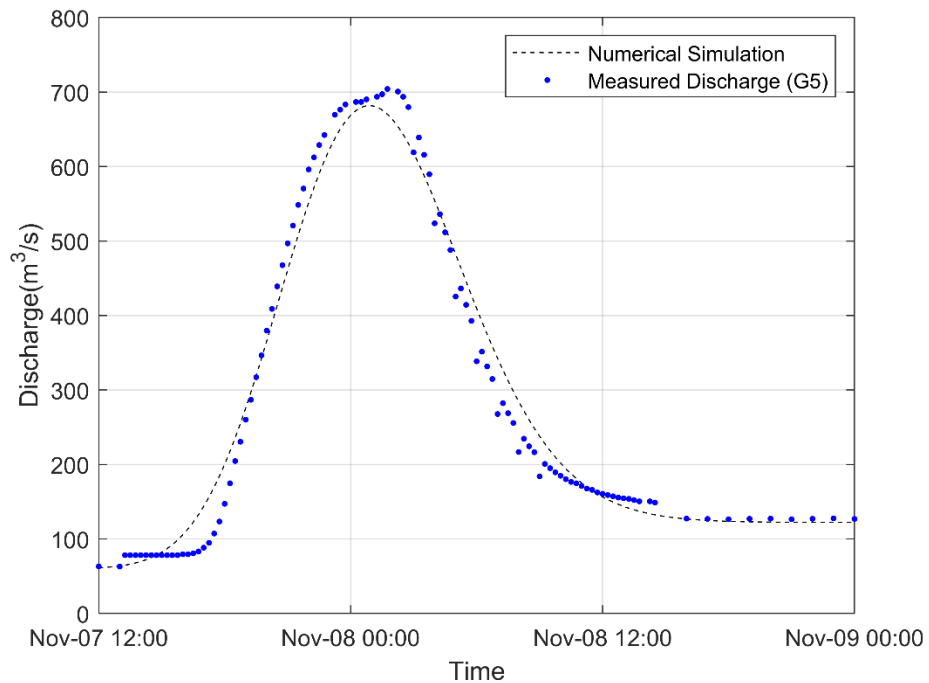


**Figure 5.9 – Application of the new hydraulic diffusivity coefficient on the Doce River reach using QUICKEST scheme (G6 – G5)**

The assumption about the equality of energy slope and channel bed slope stated in Equation 5.20 is verified by checking the results of the Crank Nicolson scheme, comparing the variation of  $\partial h/\partial x$  and  $S_f$  resultant of the simulation in the whole Reach A, as illustrated in Figure 5.10 and Figure 5.11

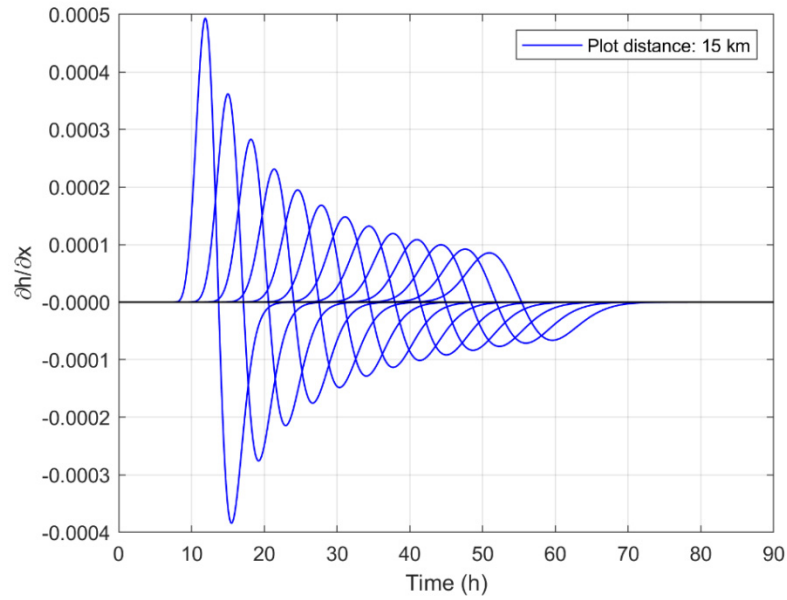


**Figure 5.10 – Variation of flow depth over distance during the numerical simulation (Reach A)**

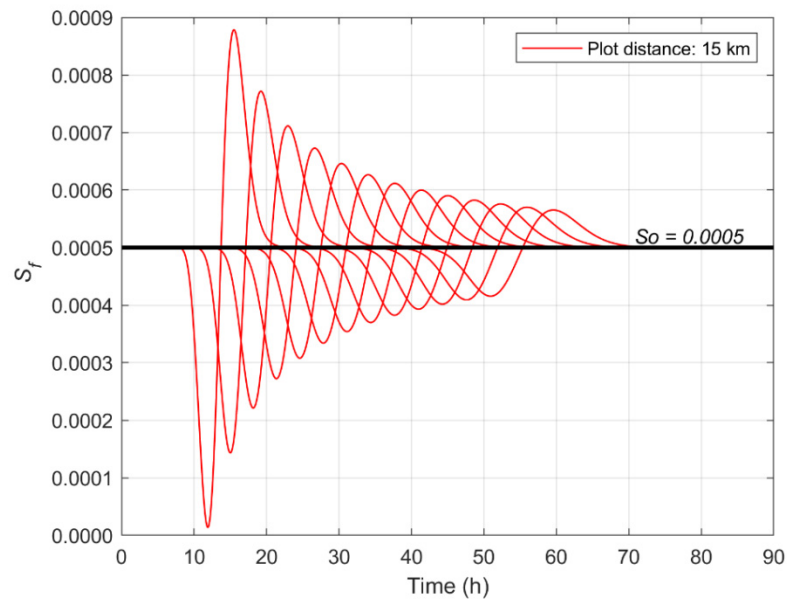


**Figure 5.11 – Variation of energy slope during the numerical simulation (Reach A)**

Observing Figure 5.10 and Figure 5.11 and comparing with Equation 5.7 one can realize that during the rising limb of the hydrograph  $\partial h/\partial x > 0$  and the energy slope is smaller than the bed slope ( $S_f < S_o$ ). The opposite is observed during the falling limb ( $\partial h/\partial x < 0$  and  $S_f > S_o$ ). However, despite the energy slope oscillation, one can realize that the average value is always equal to bed slope  $S_o$ .

Once the equality of energy slope and channel bed slope is validated, the improved performance of the new approach is attributed to the modified hydraulic coefficient, which uses parameters with less variability (Froude number and celerity) rather than the original method which depends on the high variable discharge. Moreover, the new method takes into account the additional acceleration terms of the Saint-Venant equation for the full dynamic wave. As demonstrated, both numerical schemes worked well, either the Crank Nicolson, which is implicit and unconditionally stable at the computation cost of matrix inversion and the QUICKEST, which is explicit and depends on the choice of the mesh to assure its stability. This new method is applied over the whole extension of the Doce River adopting the Crank Nicolson scheme, since its stability does not depend on the mesh size. Table 5.8 presents the summary of the parameters applied on simulation after the calibration of the river. The values of Manning  $n$  are considerably close of those obtained from the measured stage-discharge curves (Table 3.5). The mesh adopted was  $\Delta x = 250 \text{ m}$  and  $\Delta t = 300 \text{ s}$

**Table 5.8 – Floodwave simulation parameters**

Reach	$L$ (km)	$S$	$W$ (m)	$Fr$	$C_e$ (m/s)	$D_M$ (m <sup>2</sup> /s)	$n$
A	204	0.0005	200	0.18	1.20	977	0.05
B	128	0.0005	380	0.19	1.04	634	0.04
C	34	0.0008	620	0.27	1.13	267	0.03
D	108	0.0002	730	0.15	0.70	823	0.03

In the Aimorés Dam, where the most expressive routing occurred, the flood routing simulation was calculated using the Level Pool Routing to match the observed hydrographs upstream and downstream of the reservoir. The flood attenuation in Baguari Dam and Mascarenhas Dam was negligible, since the inflow hydrograph is essentially the same as the outflow. Simulated hydrographs and the observed values of the floodwave propagation are presented in the Figure 5.12 to the Figure 5.14.

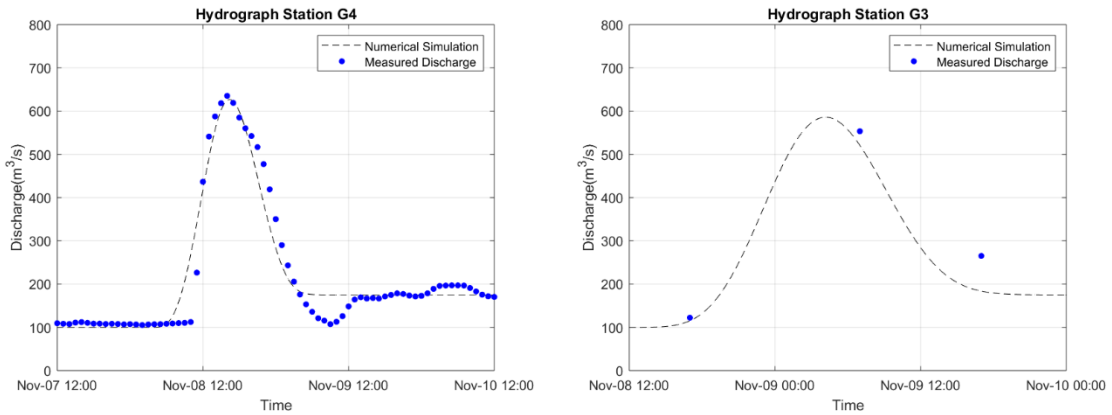


**Figure 5.12 –Hydrograph at station G4 and G3**

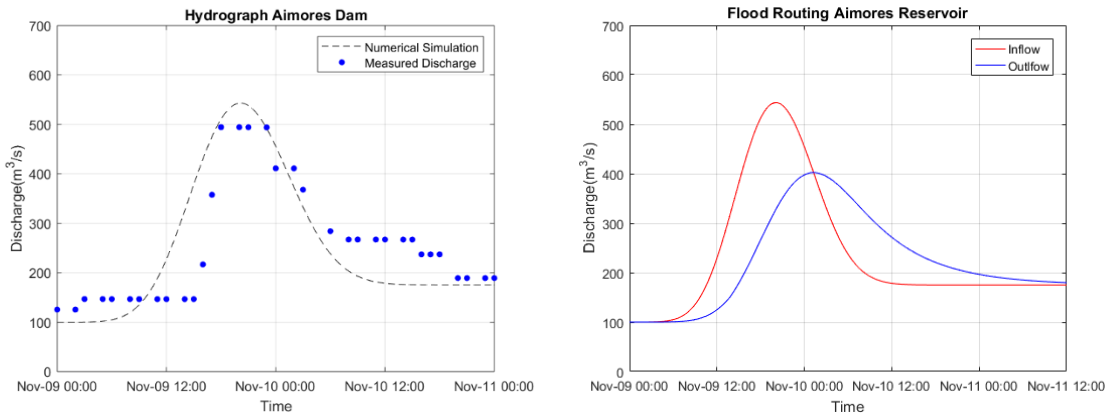


**Figure 5.13 – Hydrograph and flood routing at Aimorés Dam**

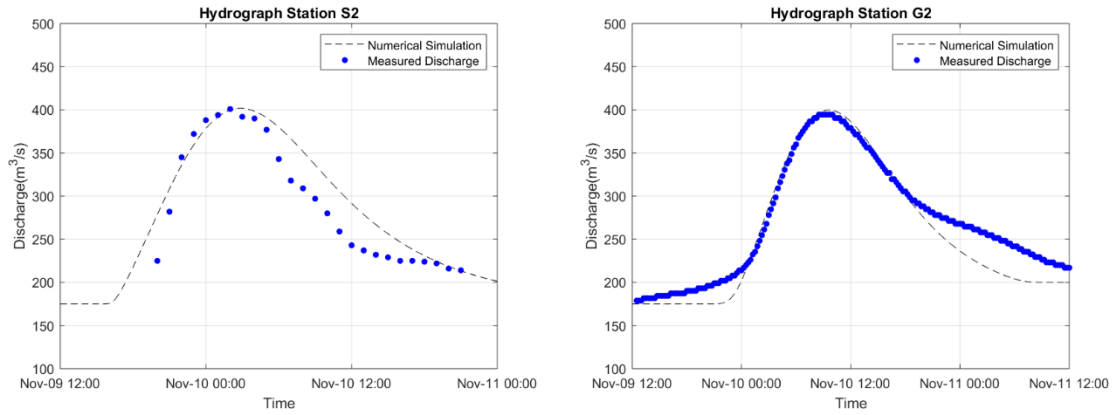


**Figure 5.14 –Hydrographs at station S2 and G2**

Finally, Figure 5.15 presents the result of numerical simulation as a space-time diagram of the Doce River. This diagram provides the visualization of the floodwave propagation in time and space through the color scale variation, according the changes in discharge magnitude. The floodwave celerity can be estimated comparing the traveled distance with the elapsed time.

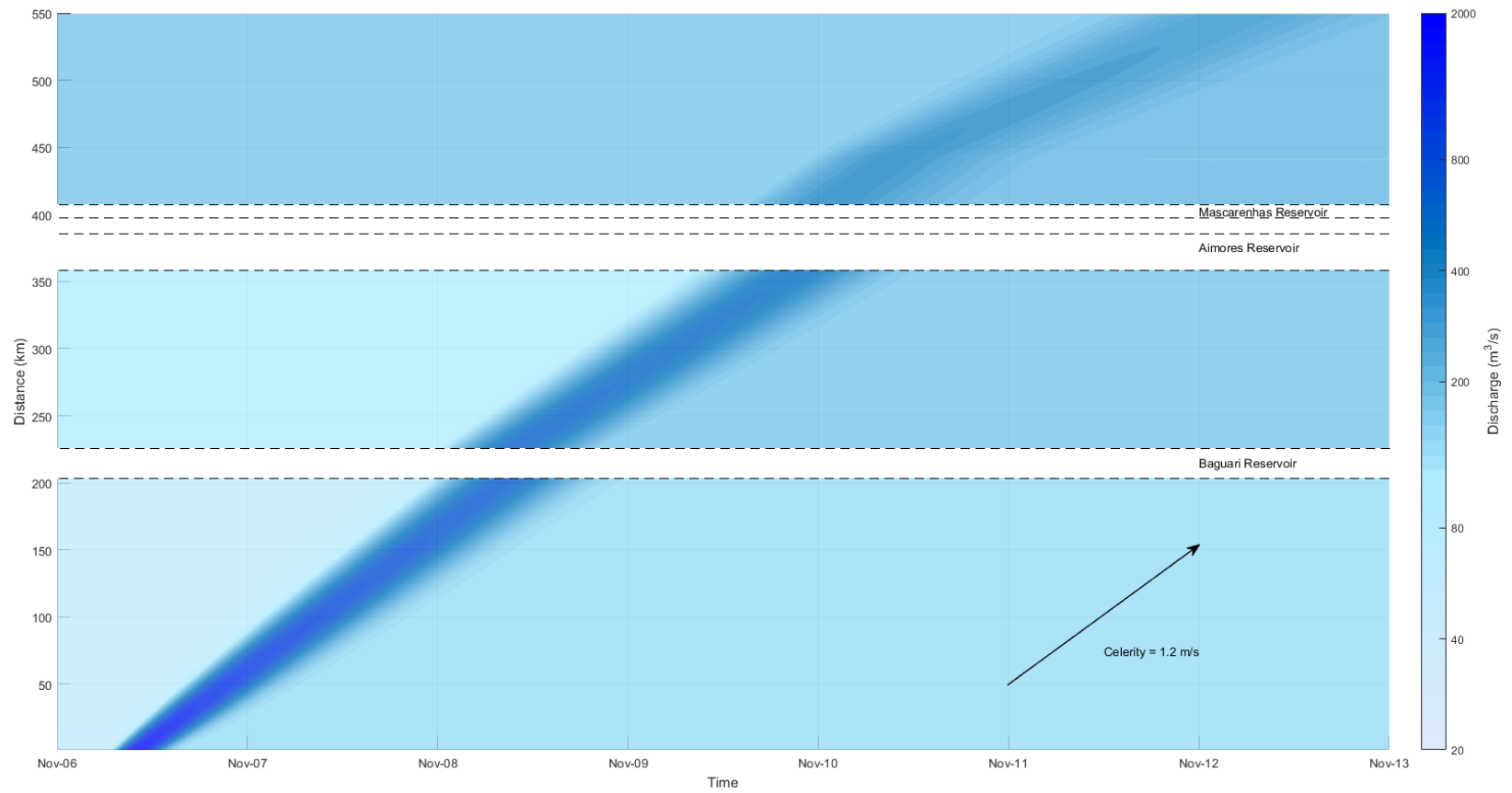


**Figure 5.15 – Space time diagram of the floodwave propagation along the Doce River after the Fundão Dam collapse**

## 5.5 Conclusions

Several common flooding routing procedures including the Modified Puls, Muskingum-Cunge, Preissmann, Crank Nicolson and QUICKEST were tested in the Doce River to simulate flashy hydrographs after the Fundão Dam collapse. None of these methods resulted in reasonable agreement with the observed hydrographs, because neither the discharge peak nor the timing was satisfactorily reproduced. All these numerical methods, except for the Modified Puls, underestimated the peak discharge with an error of up to 44%.

The unsatisfactory results presented by the traditional methods motivated the development of a new flood routing method to solve the propagation of flashy hydrograph in a low slope natural channel. The new proposed approach solves the full dynamic equation into an equivalent diffusive wave format using the modified hydraulic diffusivity coefficient, which considers all terms of the Saint-Venant equation and is determined as function of the Froude number and wave celerity, which are parameters with relatively small variation along the channel during a flood event. Numerical solution was obtained by the application of the Crank Nicolson or QUICKEST schemes, which presented very similar results. Application of the new method on the Doce River enhanced the prediction of the observed hydrographs. The maximum error decreased was from 44% to 2% RPD, from 216 m<sup>3</sup>/s to 39 m<sup>3</sup>/s RMSE and from 32% to 11% MAPE. The maximum difference found in time of peak was about 1 hour.

For the Doce River the primary improvement was due the new modified hydraulic diffusivity coefficient, which is derived as a function of Froude number and celerity instead of discharge. The addition of the acceleration terms into the Saint-Venant equation resulted in a secondary effect on the floodwave attenuation due to the low Froude number along the channel ( $Fr \approx 0.2$ ). Finally, once the flow condition is accurately calculated, the next step is to simulate the suspended sediment propagation, as presented in the next section.

## 6. SEDIMENT TRANSPORT MODEL

### 6.1 Numerical Model of Suspended Sediment Transport

The analytical solution of the advection-dispersion equation with settling using constant parameters along the Doce River (Section 4.4) presented satisfactory results on the evaluation of the suspended sediment transport after the Fundão Dam collapse. However now, a more comprehensive numerical simulation of the sediment transport was developed to be coupled with the numerical flow simulation, presented in the previous chapter. The physical processes and equations employed on this sediment transport numerical simulation are presented in Table 6.1

**Table 6.1 - Physical process and equations applied in the sediment transport simulation along the Doce River**

Physical Process	Equation
Suspended Sediment Transport	Advection-Dispersion with Settling
Changes in the river bed	Exner
Sediment Transport on Reservoirs	Conservation of sediment mass

Modeling of the suspended sediment transport is justified since it is the main mode of sediment transport after the Fundão Dam collapse, as defined in Section 4.3. Moreover, according to the observed data along the Doce River, in reach A the sediment transport occurred under the unsteady flow condition. For the other reaches downstream (reaches B, C and D), due to separation between the floodwave and suspended sediment, the sediment transport could be simulated considering the steady flow state. Therefore, along the reach A the model allowed the variation of the longitudinal dispersion coefficient  $K_d$  [Equation 4.4] and the settling rate  $k$  [Equation 2.30]. For the subsequent reaches the sediment transport parameters were held constant following the steady flow condition.

Parameters of the sediment model are presented in Table 6.2. The simulation was carried out by solving numerically the advection-dispersion equation through the Crank Nicolson scheme (Appendix D). The mesh adopted is the same of that used in the flow simulation, i.e.  $\Delta x = 250 \text{ m}$  and  $\Delta t = 300 \text{ s}$ .

**Table 6.2 – Sediment transport simulation parameters**

Reach	$Q \text{ (m}^3/\text{s)}$	$n$	$d_s \text{ (}\mu\text{m)}$	Water Temp ( $^{\circ}\text{C}$ )
A	Variable	0.050	1.50	29
B	175	0.074	1.95	30
C	315	0.071	1.20	29
D	315	0.030	1.45	29

The sediment propagation in the reservoirs was simulated using Equation 2.44 with the calibrated parameters  $k$  and  $t$  (Table 4.7). Figure 6.1 shows the result of the numerical simulations of the suspended sediment transport along the Doce River including the observed concentrations. Moreover, to illustrate the impact of the Fundão Dam collapse in the water supply systems, the plot indicates an estimate of the conventional limit of the water treatment plant (WTP), approximately 2,500 mg/l in the Doce River.

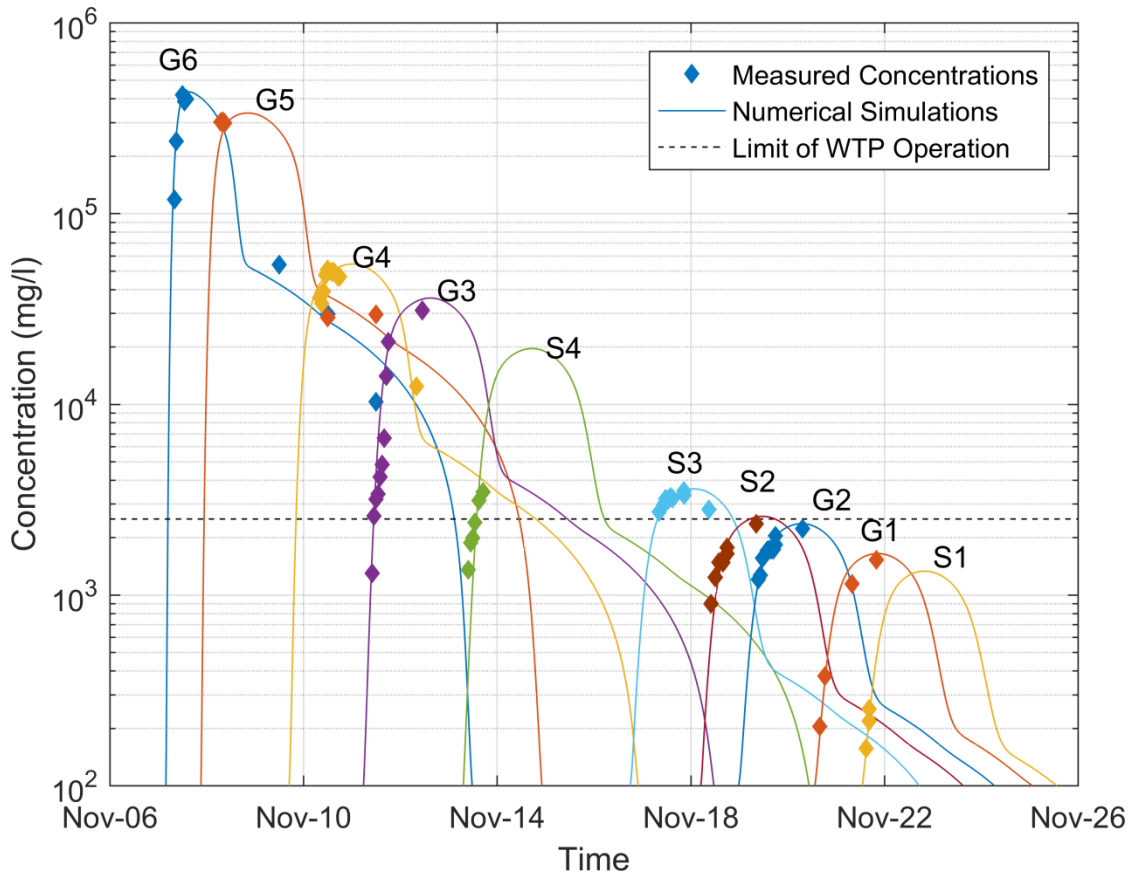


**Figure 6.1 – Sediment concentration along the Doce River after the Fundão Dam collapse and the limit of operation of WTP**

A visualization of the consequences of the high concentrated flow is provided in Figure 6.2, where there is an image of the treatment plant at Colatina Town (station G2), during the passage of the mud (Machado, 2015). The collapse of the Fundão Dam led to the water treatment plant shutdown, affecting more than 100,000 people in this town.



**Figure 6.2 – Water treatment plant at Colatina Town at station G2, (Machado, 2015)**

Another output of the numerical model is the sediment deposition along the Doce River. The thickness of the deposition layer was calculated using Equation 2.42, adopting an average value for porosity  $p_o$  equal to 0.4 (Julien, 2010; Koliji, 2018). Figure 6.3 and Figure 6.4 show the calculated deposition in the reaches A and B, where the volume settled was  $2.3 \text{ Mm}^3$  and  $0.4 \text{ Mm}^3$  respectively. Settling in reaches C and D was negligible since most of the remaining sediment was trapped in the Aimorés and Mascarenhas reservoir.

Despite the large amount deposited along the Doce River, the thicker layer deposited was on Reach A, with an average depth smaller than 0.1 m. The river dimensions were sufficient to accommodate the settled sediment without substantial changes along the cross section. Finally, Figure 6.5 shows the space-time diagram of the propagation of the suspended sediment along the Doce River to the ocean.

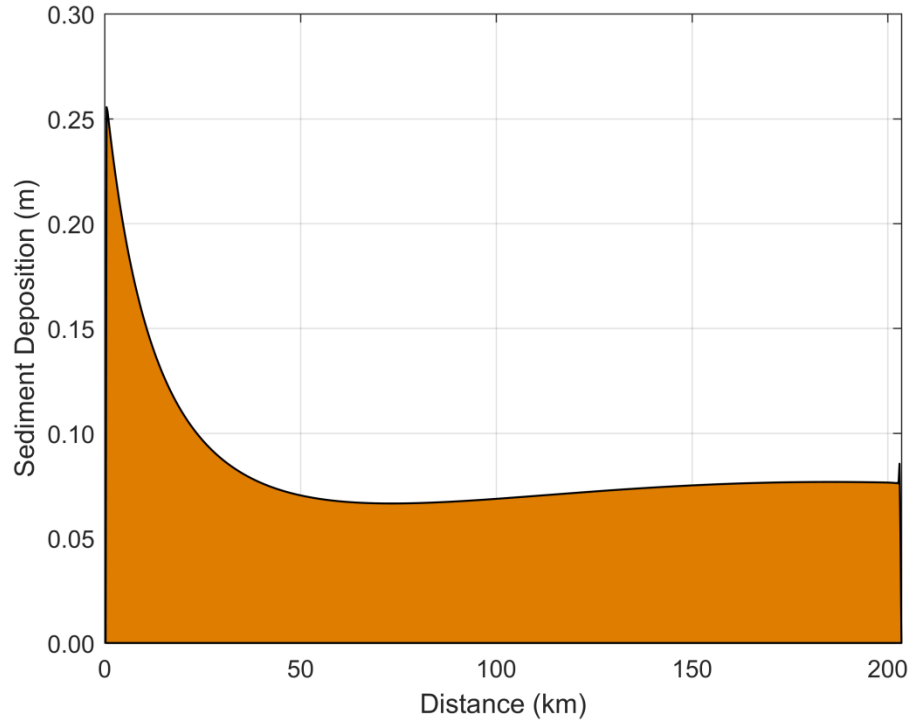


**Figure 6.3 – Sediment deposition at the Reach A**

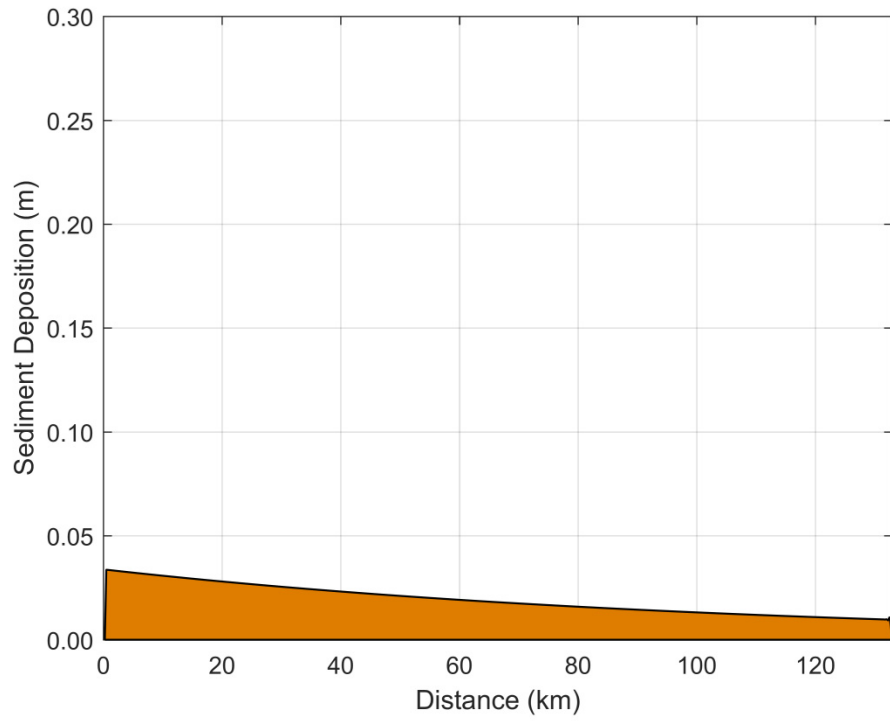


**Figure 6.4 – Sediment deposition at the Reach B**

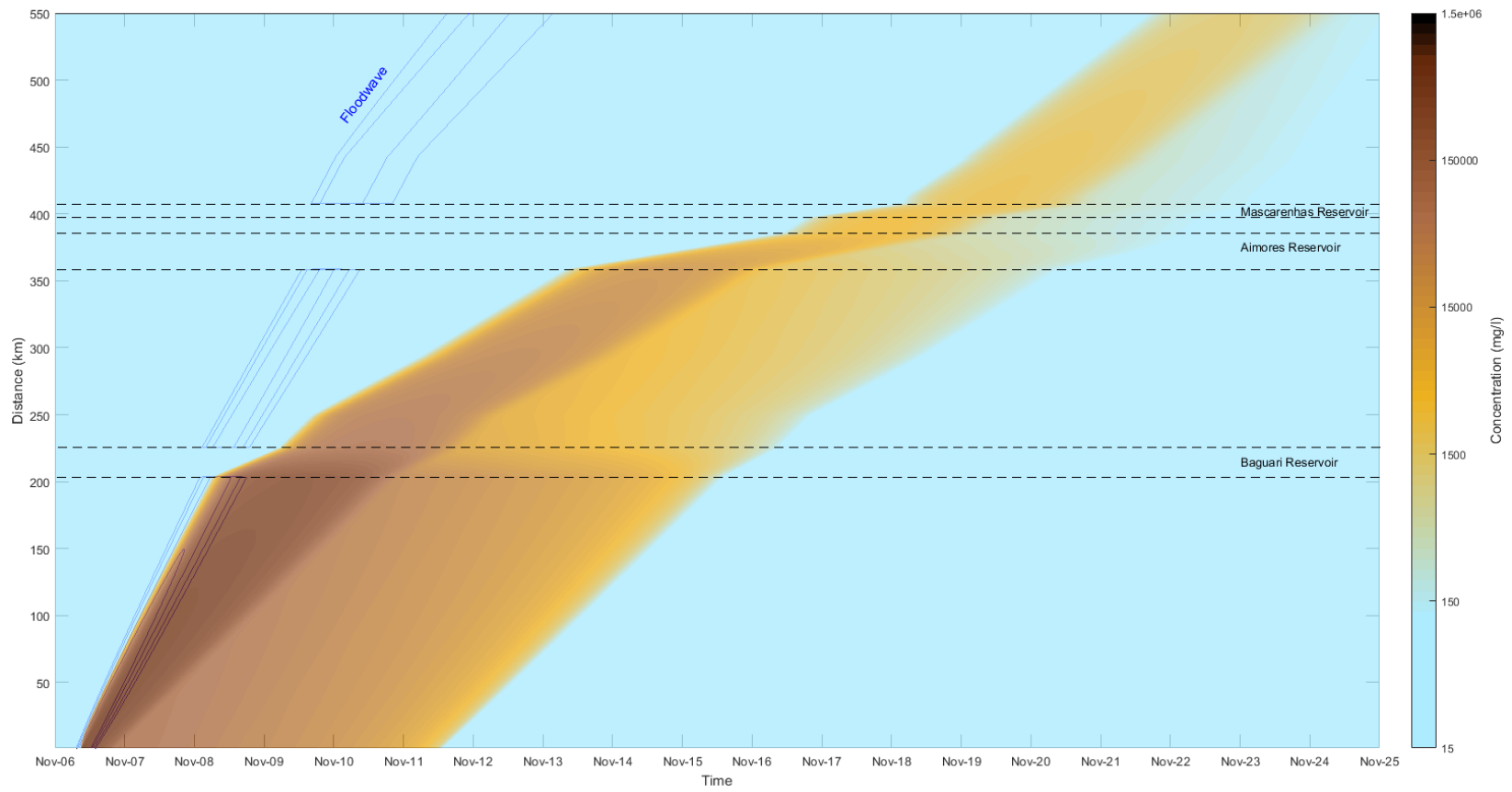


**Figure 6.5 – Space time diagram of the sediment concentration and floodwave propagation along the Doce River after the Fundão Dam collapse**

## 6.2 Effects of Changes in Water Temperature

The analysis of the observed sediment concentration along the Doce River showed that the settling rate is associated with fine sediment stored at Fundão Dam, as presented in Table 4.6. Measurements along the Doce River show that the average water temperature was approximately 29°C during the passage of the sediment. However, significant variations in water viscosity (and consequently in the fall velocity) can be expected due to changes in water temperature. For instance, for fine sediment (e.g., medium clay particle  $d_s \cong 1.5 \mu m$ ) the change in water temperature from 30°C to 5°C increases the kinematic viscosity and fall velocity in approximately 50%. This effect can lead to substantial changes in suspended sediment concentration through the river. Bearing this in mind, this investigation has the purpose to quantify the temperature variation effect on sediment propagation.

A sensitivity analysis was carried out using the same simulation parameters presented in Table 6.2, with exception of the water temperature, which was reduced from 29 °C to 5 °C, using 5°C intervals. Table 6.3 summarizes the results of the simulation presenting the maximum concentration in each station under different temperatures while Figure 6.6 presents a comparison between the observed concentrations and the maximum estimated concentration.

**Table 6.3 – Maximum simulated concentration as function of water temperature**

Station	Water Temperature					
	29°C	25°C	20°C	15°C	10°C	5°C
	Maximum Concentration (mg/l)					
G5	311,700	345,149	357,309	368,838	379,671	389,768
G4	51,600	68,273	83,622	103,040	124,784	147,964
G3	36,350	47,658	60,904	77,908	97,509	119,025
S4	21,840	27,951	38,050	51,457	67,636	86,200
S3	3,700	6,195	9,813	15,671	24,023	35,098
S2	2,800	4,607	7,519	12,406	19,601	29,414
G2	2,560	4,254	7,009	11,660	18,556	28,024
G1	1,930	3,100	5,302	9,114	14,930	23,128
S1	1,600	2,559	4,476	7,848	13,084	20,584

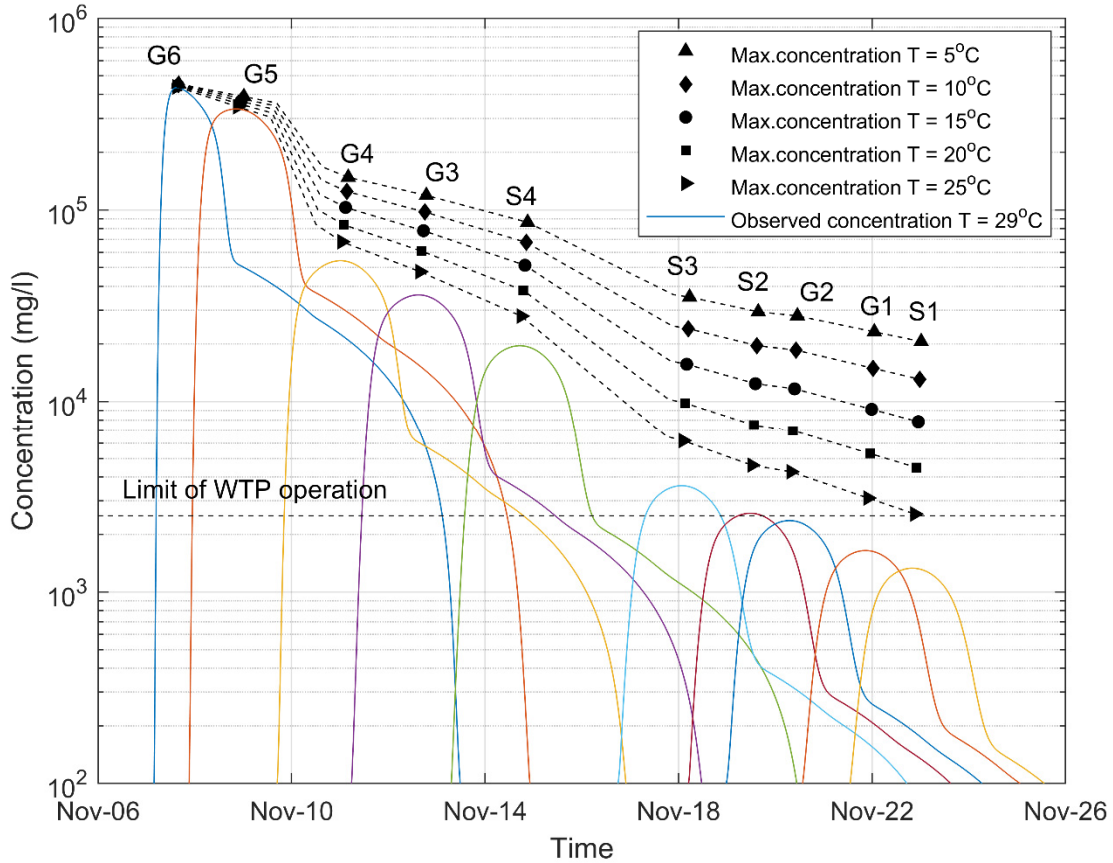


**Figure 6.6 – Analysis of the effects of the water temperature in the suspended sediment propagation**

One can observe that a hypothetical decrease in water temperature could have caused an increase in maximum concentration along the Doce River. A temperature drop of 25° C would have increased the sediment concentration at sea from 1,600 mg/l to 20,500 mg/l, which represents a concentration approximately 13 times higher. The analysis highlights that tailings dam spills are more critical in cold temperature zones since the water temperature can affect the sediment settling, propagating the high concentration flow along greater distances in the water bodies.

### 6.3 Effects of Reservoirs

A second analysis was carried out in order to simulate the effectiveness of the hydropower plant reservoirs in reducing the sediment concentration along the Doce River. Thus, the current simulation considers the hypothesis of the non-existence of the reservoirs.

The sediment concentration upstream of Candonga Dam  $C_i$  was obtained considering the following assumptions: initially, since the hyperconcentrated flow is classified as Mud Flood upstream of Candonga Dam (Table 4.1), it was assumed that the floodwave and the sediment arrived at same time at this reservoir. The observed data pointed that the flood arrived on Candonga Dam the next day about 07:00 AM after the collapse (CPRM & ANA, 2015a). Moreover, the time  $t$  for sediment to cross the reservoir is the difference between the time of arrival of the floodwave in this reservoir and the moment when it started to propagate downstream, what could be estimated using the numerical simulation with the observed concentration in the Doce River. Therefore, the suspended sediment concentration upstream of the Candonga Dam is estimated using the inverse of Equation 2.44, as shown in Equation 6.1:

$$C_{oi} = \frac{C_i}{e^{-kt}} \quad (6.1)$$

The settling rate in the reservoir must result in the same sediment volume deposited upstream of Candonga Dam, estimated by the Brazilian Agencies as  $11.8 \text{ Mm}^3$  (Table 4.1). Taking into account the above-mentioned assumptions, Table 6.4 shows the result of the parameters estimative.

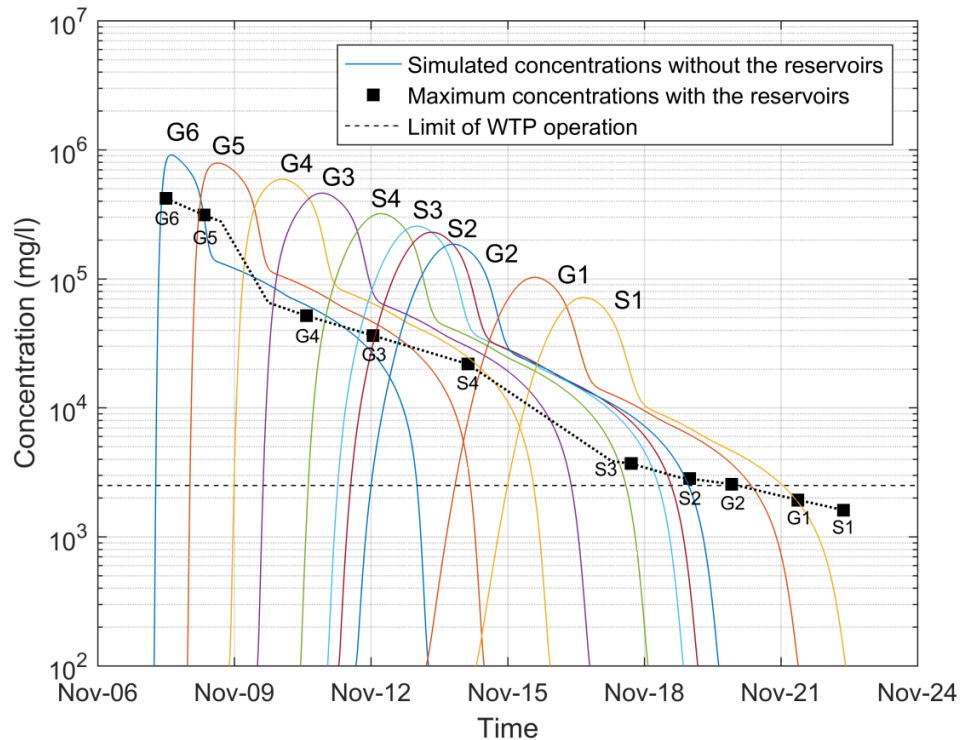
**Table 6.4 – Parameters of Candonga Dam reservoir to estimate the upstream concentration**

Reservoir Length (km)	Reservoir Depth (m)	Flow Velocity (m/s)	Water Temperature (°C)	$k$ ( $day^{-1}$ )	$d_s$ ( $\mu m$ )
8.5	14	0.94	30	8.21	35

The settling rate obtained corresponds to a representative particle size ( $d_s = 35 \mu m$ ) close to  $d_{50}$  ( $d_s = 38 \mu m$ ) of the material stored in the Fundão Dam.

Applying Equation 6.1, the estimated peak of suspended sediment concentration upstream of Candonga Dam resulted in approximately 1,500,000 mg/l. Thus, this estimated sediment concentration and the hydrograph at Candonga Dam obtained in section 5.2 were used to perform a simulation considering the hypothesis of non-existence of the hydropower plant reservoirs. The objective of this simulation was to quantify the impact of the reservoirs on the sediment propagation.

The sediment transport model was simulated considering the unsteady flow along the whole reach of the Doce River using the calibrated model developed in Chapter 5. The length of the reaches A and B were extended to consider the reservoirs extensions. Figure 6.7 presents the comparison between the numerical simulation without the reservoirs and a tracer of maximum concentration observed. In addition, Figure 6.7 shows the estimated limit of operation of the water treatment plant.



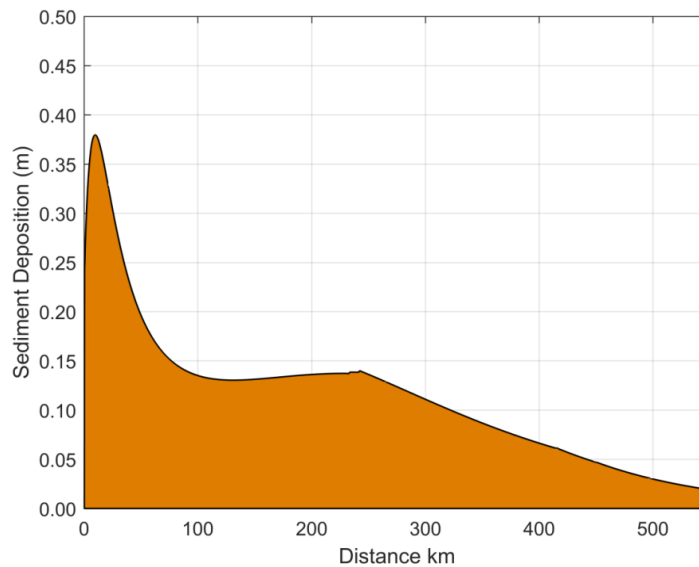
**Figure 6.7 – Suspended sediment simulation considering the hypothesis of inexistence of the Doce River hydropower reservoirs**

Table 6.5 shows the maximum concentration and the number of hours in each station where the concentration exceeds the conventional treatment limit. In addition, Figure 6.8 shows the simulated deposition along the Doce River. Finally, the space-time diagram of the floodwave and sediment propagation is presented in Figure 6.9.

**Table 6.5 – Comparison between observed concentrations and the simulation without the reservoirs**

Location	Observed		Simulation without reservoirs	
	Max. concentration (mg/l)	Number of hours above treatment limit	Max. concentration (mg/l)	Number of hours above treatment limit
Candonga Dam	620,000*	120	1,268,522	123
G6	418,850	142	912,126	138
G5	311,700	156	789,002	148
G4	51,600	119	590,436	158
G3	36,350	96	460,971	162
S4	21,840	63	319,607	167
S3	3,700	37	255,683	169
S2	2,800	12	229,506	169
G2	2,560	≈0	185,210	167
G1	1,930	0	102,533	156
S1	1,600	0	71,620	145

\* Value estimated using numerical model.



**Figure 6.8 – Sediment deposition along the Doce River (starting at Candonga Dam) without the reservoirs**

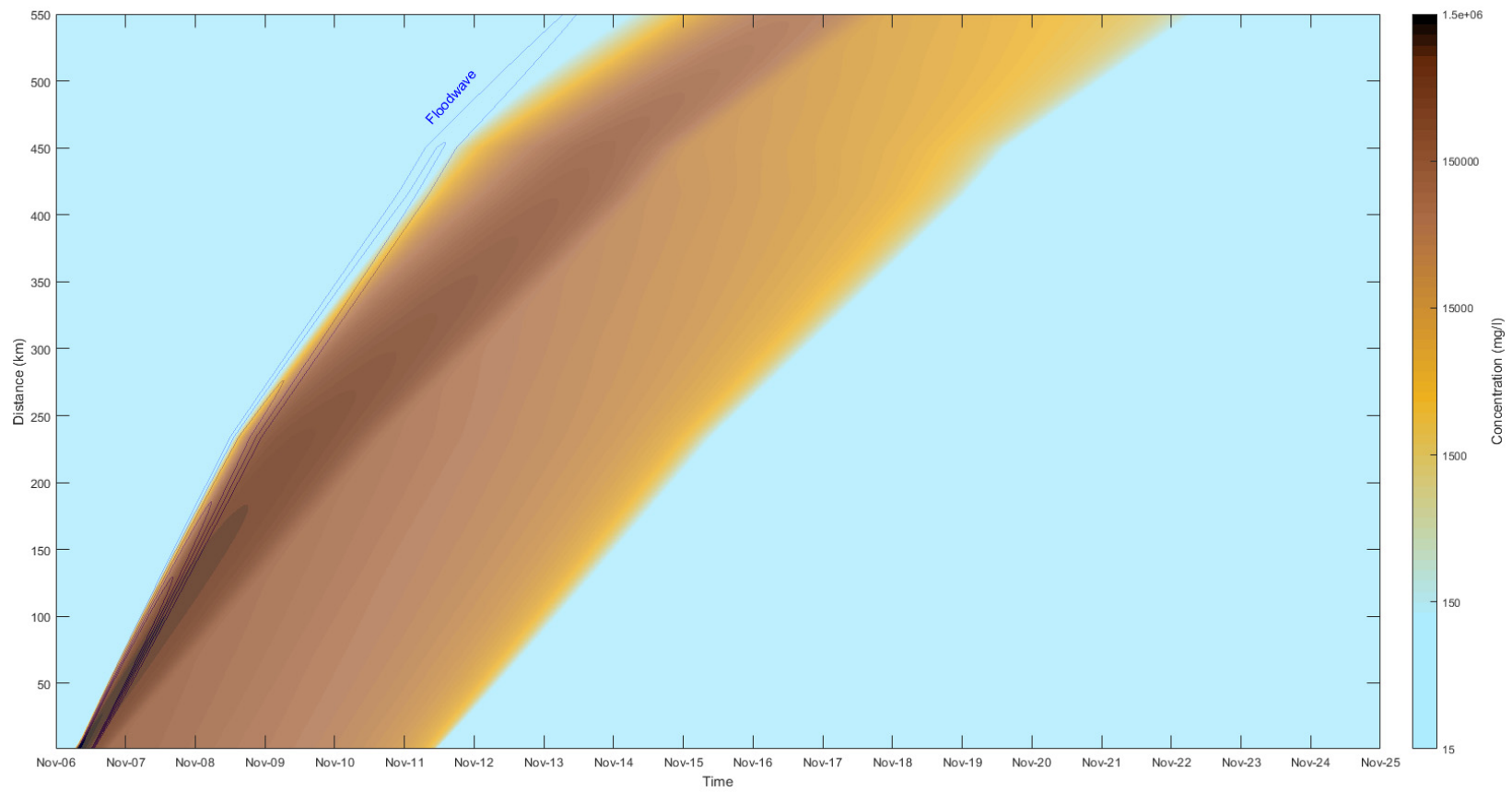


**Figure 6.9 – Space time diagram of the suspended sediment propagation and the floodwave assuming the hypothesis of inexistence of the reservoirs**

## 6.4 Conclusions

The one-dimensional model based on the numerical solution of the advection-dispersion equation with settling provided strong agreement with the observed suspended sediment concentrations. This model was able to simulate the suspended sediment transport along the Doce River and in the reservoirs under unsteady and steady flow conditions.

The calibrated model was applied for a parametric analysis on the evaluation of the two hypothetical scenarios: the changes in water temperature and the absence of reservoirs. Initially, the analysis with a hypothetical decrease in the water temperature of 25°C showed that it would have caused a concentration approximately 13 times higher at the coast. This is attributed to the substantial effect of water temperature on fine sediment settling.

The sediment propagation without the hydropower reservoirs along the Doce River would have caused an even higher sediment concentration, resulting in an extended interruption in water supply (up to 170 hours), particularly in the cities located in the lower part of the river. Furthermore, the concentration on the coast would have reached a concentration approximately 45 times higher.

## 7. MODEL APPLICATION TO SIMULATE THE HYPOTHETICAL COLLAPSE OF OTHER TAILINGS DAMS IN THE DOCE RIVER BASIN

### 7.1 Tailings Dams in the Doce River Basin

According to data of the National Department of Mineral Production (DNPM, 2017) there are 106 tailings dams placed in the Doce River basin as illustrated in the Figure 7.1.



**Figure 7.1 – Tailings Dams in the Doce River basin**

Among all the tailings dams in this basin, there is registered information for the main dams (total of 56), which are enrolled in the Dam Safety National Plan (DNPM, 2017). For these dams, data available are stored volume, dam height and type of material stored for some of them.

Thus, the objective of this current analysis is to simulate the propagation of the sediment (tailings) due the hypothetical collapse of these dams in order to evaluate the impact of each dam in water supply systems on towns located downstream. The path of the contaminated water after a possible failure of the evaluated tailings dams can be obtained using the hydrography data of the National Water Agency and the digital elevation model (DEM) of the Doce River basin, with a spatial resolution of 10 m (Geonetwork, 2007), as presented in Figure 7.2.

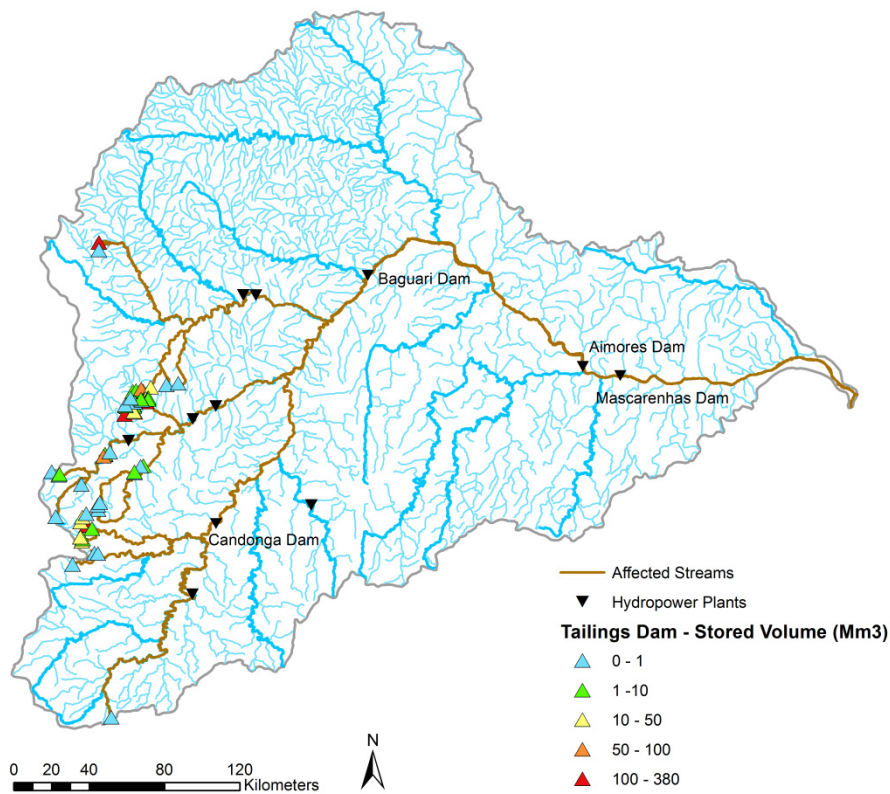


**Figure 7.2 – Reaches affected in the hypothesis of failure of other tailings dams in the Doce River basin**

The next section describes the details involved in the calculation of the propagation of the sediment following the hypothetical collapse of each dam.

## 7.2 Modeling the Suspended Sediment Propagation after a Tailings Dam Failure

Initially, the volume spilled after a tailings dam break can be estimated by Equation 2.1:

$$V_F = 0.354V^{1.01} \quad (2.1)$$

Where  $V_F$  is the waste outflow volume (which includes tailings and water) and  $V$  is the total impoundment volume. In addition, the peak discharge after the collapse of a tailings dam is approximated by Equation 2.20:

$$Q_{max} = 325(HV_F)^{0.42} \quad (2.2)$$

Considering that the dam break hydrograph has a triangular shape, the time for the spill of the stored material can be calculated through Equation 7.1:

$$t_{spill} = \frac{2V_F}{Q_{max}} \quad (7.1)$$

Then, substituting the empirical Equations 2.1 and 2.2 into Equation 7.1, one can obtain the time of spill  $t_{spill}$  in seconds

$$t_{spill} = 3369.5 \frac{V^{0.59}}{H^{0.42}} \quad (7.2)$$

Where  $V$  is the total impoundment volume in  $hm^3$  and  $H$  is the height of the dam in  $m$ .

The hypothetical failure simulation of the tailings dams in the Doce River basin considers the following the assumptions:

- I. The collapse of a tailings dam results in a pulse of sediment in the streams, which time duration is function of the stored volume and the dam high, as given by Equation 7.2.
- II. The maximum concentration of the suspended sediment after the spill is assumed to be 1,500,000 mg/l, which was the maximum estimated concentration after the Fundão Dam collapse according Table 4.1 and Equation 4.2.

- III. The propagation of the sediment pulse after the tailings dam collapse can be calculated through the one-dimensional advection-dispersion equation, which was validated with the observations along the Doce River after the Fundão Dam collapse:

$$\frac{\partial C}{\partial t} + U \frac{\partial C}{\partial x} = K_d \frac{\partial^2 C}{\partial x^2} - kC \quad (2.29)$$

- IV. The expression developed by Kashefipour and Falconer (2002), Equation 4.4, can be employed to estimate the longitudinal dispersion coefficient  $K_d$ :

$$K_d = 10.612(U/u_*)hU \quad (4.4)$$

- V. The settling rate along the rivers is given by Equation 2.30 assuming a representative particle size is equal to  $1.5 \mu m$ , which is the average particle size correspondent to the observed settling rate along the Doce River. Conservatively, the water temperature was assumed to be  $25^\circ C$ .

$$k = \frac{\omega_i}{h} \quad (2.30)$$

- VI. As a simplification, the flow regime in every stream was assumed to be in steady state, adopting a constant velocity of  $0.75 \text{ m/s}$  and the Manning's coefficient equal to  $0.045$  (mean values observed in the Doce River, according to the section 3.3).
- VII. The length and slope of the river reaches are obtained using the Doce River basin DEM data with spatial resolution of  $10 \text{ m}$  (Geonetwork, 2007). Data were processed in Hydrology Tool (Spatial Analyst Tool) in ArcMap 10.1. This procedure allowed the measurement of length and slope of each stream, starting from the nearest creek going to the next tributary and finally to the Doce River.
- VIII. The Crank Nicolson numerical scheme was applied since its application resulted in a satisfactory agreement with the observed data on Doce River. The mesh was equal to  $\Delta x = 250 \text{ m}$  and  $\Delta t = 300 \text{ s}$ .

As observed in the Doce River, there were hydropower reservoirs along the path of the contaminated waters (Figure 7.2). Thus, to consider the effect of the reservoirs over the suspended sediment propagation one can use Equation 2.44, which presented satisfactory results with the observed concentrations along the Doce River.

$$C_i = C_{oi}e^{-kt} \quad (2.44)$$

The flow velocity in every reservoir was assumed equal to 0.15 m/s and the representative particle size for the calculation of the settling rate equal to 7  $\mu\text{m}$ . Those values are the average observed values in the Doce River reservoirs after the Fundão Dam collapse. The data of the hydropower reservoirs in the tributaries, which locations are showed on Figure 3.1, is presented in Table 7.1.

**Table 7.1 – Data of reservoirs in the tributaries(Geonetwork, 2007; CEMIG, 2018)**

Reservoir	Area (km <sup>2</sup> )	Volume (hm <sup>3</sup> )	Depth (m)	Length (km)
Brecha Dam	0.14	0.9	6.2	1.3
Gui-Amorin Dam	1.17	3.96	3.4	5
Peti Dam	5.81	80.04	13.8	11.5
Porto Estrela Dam	4.53	89.04	19.7	10.5
Sa Carvalho Dam	0.58	1.38	2.4	4
Sao Goncalo Dam	1.26	5.86	4.7	3.7

After a hypothetical tailings dam failure, the generated sediment pulse is propagated in the main tributaries using the numerical solution of advection-dispersion equation. Then, the sediment concentration is converted to turbidity through the relationship obtained from the measurements, as illustrated in Figure 3.18. The towns in the region where the sediment concentration is equal or greater than 2,500 mg/l (Chang & Liao, 2012) are considered affected, because the conventional water treatment is hindered. The sediment is not considered toxic, because the most of the dams store tailings similar as those in Fundão Dam. The affected population is counted considering the data of the Brazilian Institute of Geography and Statistics (IBGE, 2010), as illustrated in Figure 3.3.

Figure 7.3 summarizes the processes simulated in the numerical model while Figure 7.4 shows an example of estimate of the affected population after a hypothetical failure of a tailings dam in the Doce River basin.

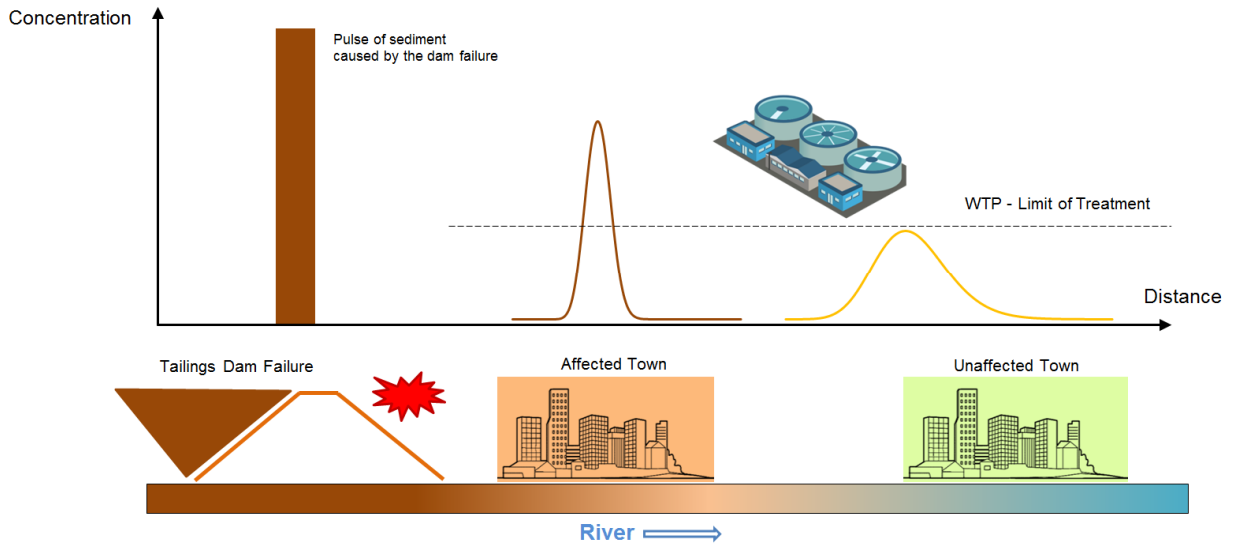


Figure 7.3 – Sketch of the sediment propagation after a hypothetical tailings dam failure

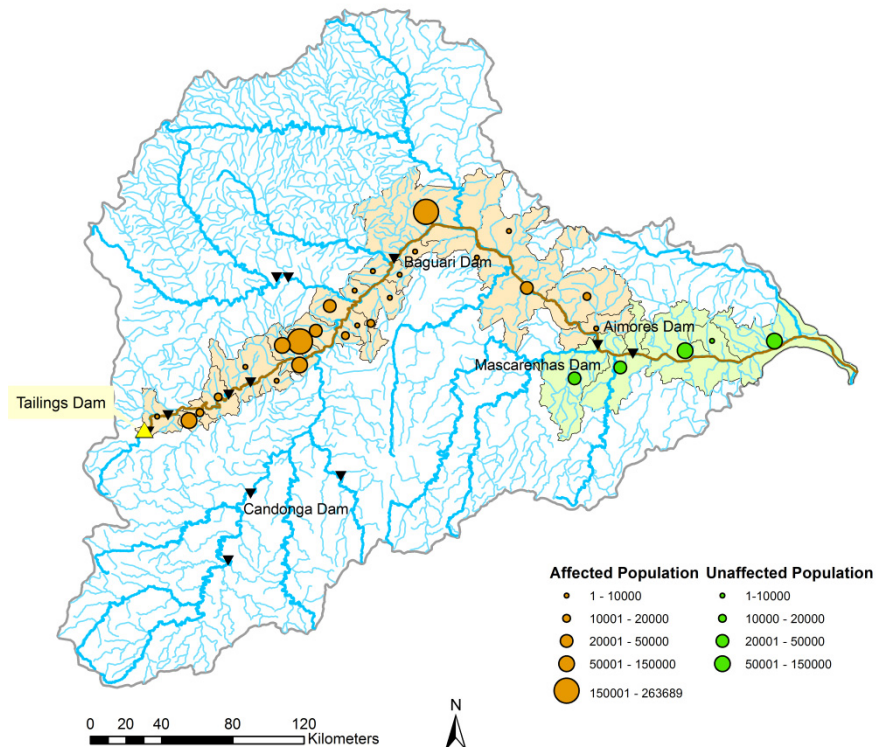
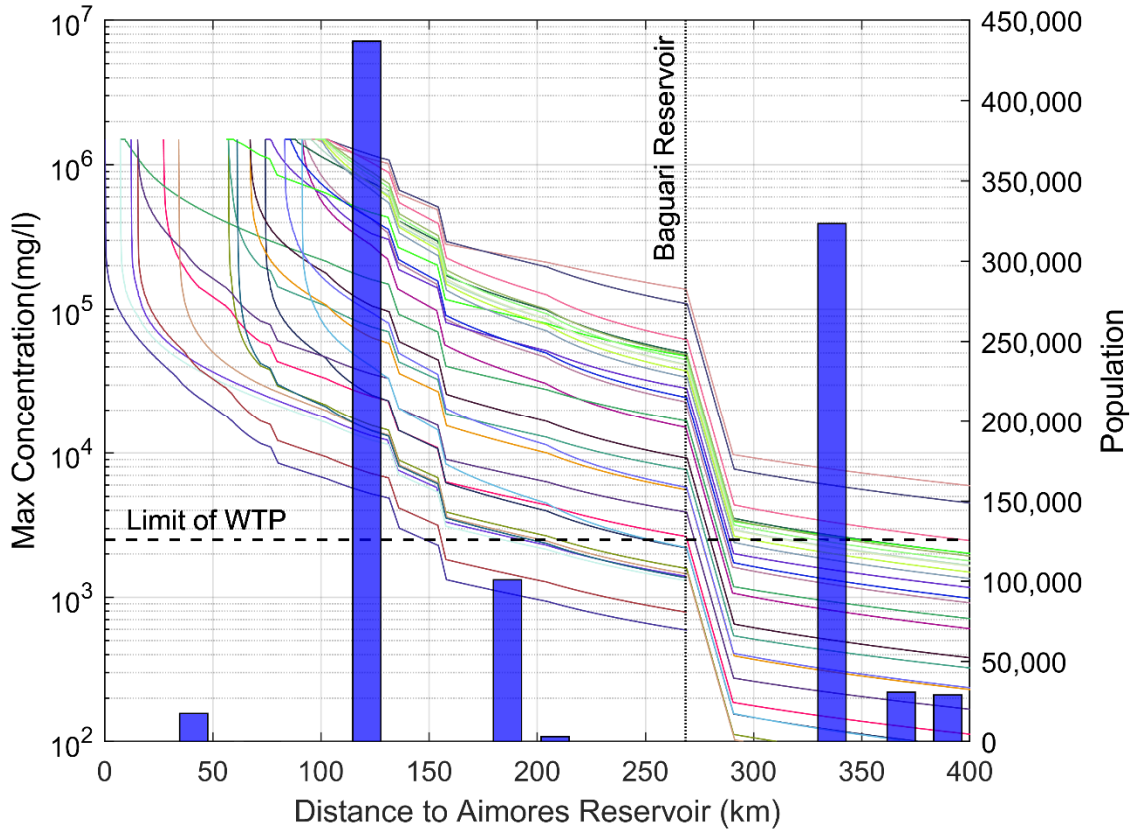
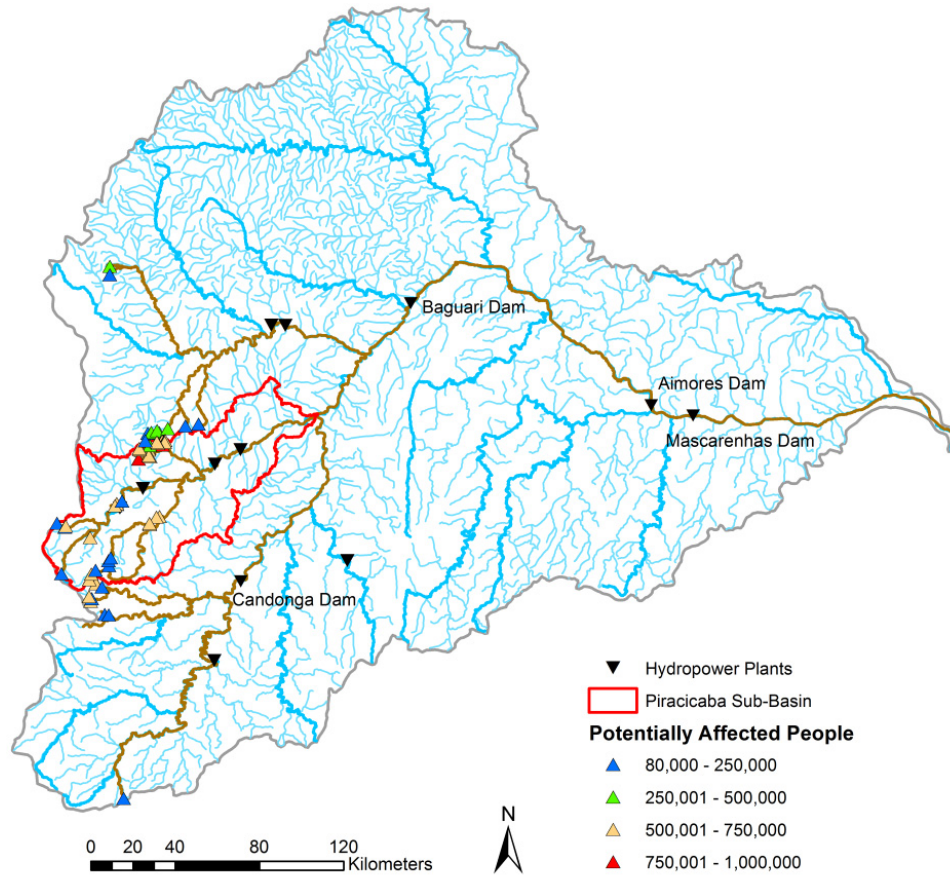


Figure 7.4 – Example of the affected population after a hypothetical tailings dam failure on the Doce River basin

The numerical simulation calculates the propagation of the high sediment concentration, which is then compared with water treatment plant limit ( $\approx 2,500$  mg/l) and the location of the towns, as illustrated in Figure 7.5. Finally, the tailings dams are classified according to the potentially affected people, as shown in Figure 7.6.



**Figure 7.5 – Propagation of the high sediment concentration due the collapse of tailings dams in the Doce River basin**



**Figure 7.6 – Mapping the tailings dam according the number of potentially affected people**

The region with the dams with highest potential impact is the Piracicaba River sub-basin, with an area of 5,400 km<sup>2</sup>. There are thirty-four dams in this sub-basin and these dams are prone to affect more people due several factors as stored volume, proximity with populated towns and existence of only small hydropower reservoirs, with reduced capacity to trap sediment. Figure 7.7 shows the tailings dams in the Piracicaba River sub-basin

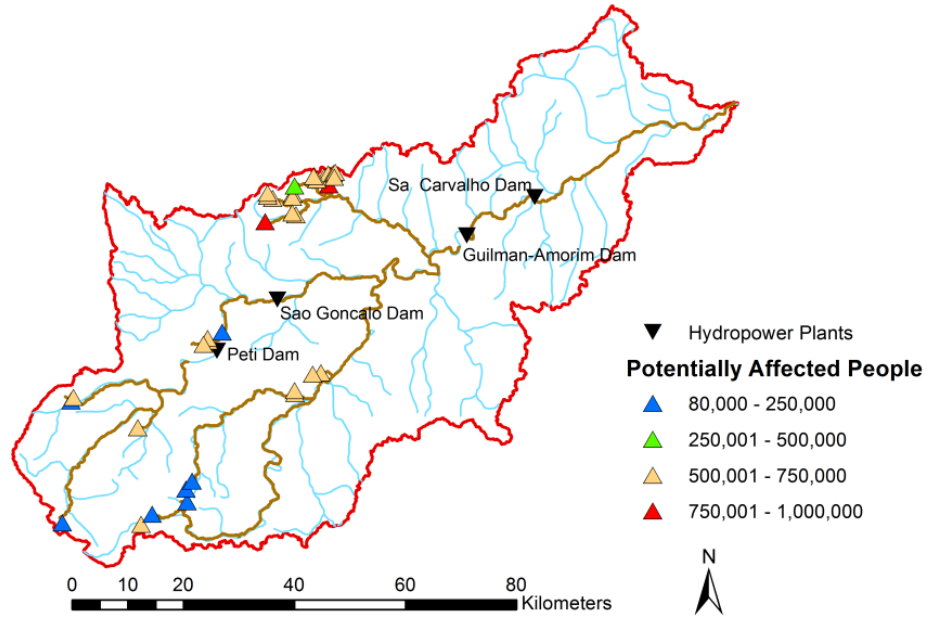


**Figure 7.7 Tailings dams in the Piracicaba River sub-basin classified according to the potentially affected people**

The result of the numerical simulation is presented also as a rank, from the most impacting dam to the less, making distinction between the tailings dams in the Piracicaba River Sub-basin and in other sub-basins, as showed in Figure 7.8.

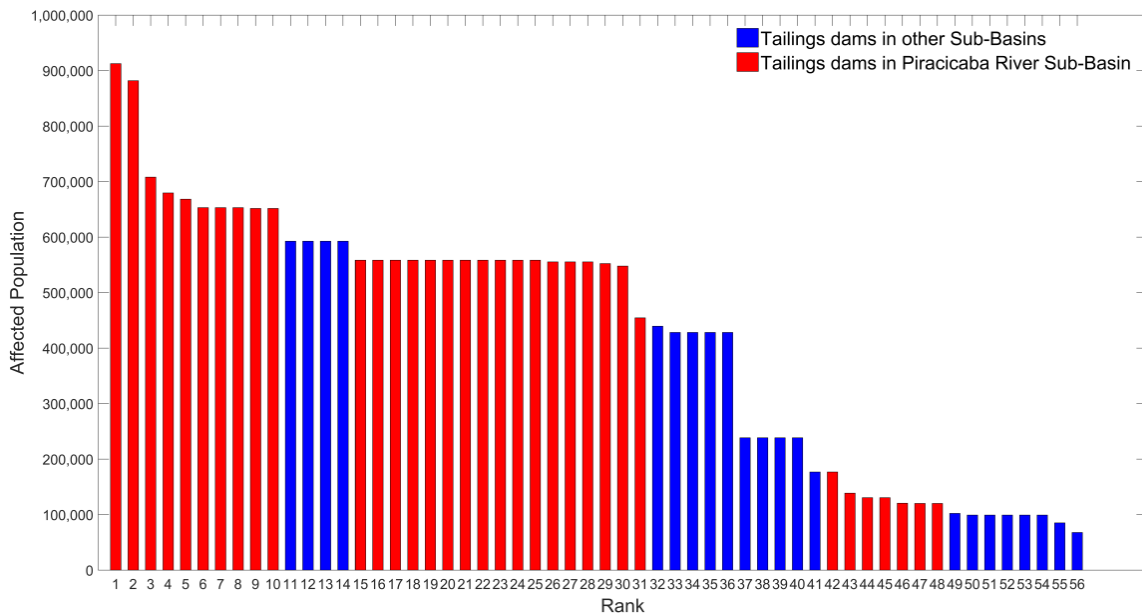


**Figure 7.8 – Rank of the potential impact of the tailings dams in the Doce River Basins.**

### 7.3 Conclusions

The model developed based on the observed sediment concentration along the Doce River is now applied on the other tailings dams. This simulation considers that the failure of the dams will cause a sediment pulse in the streams located immediately downstream.

The propagation of the suspended sediment is carried out through the application of the advection-dispersion equation with settling solved numerically using the Crank Nicolson scheme in the river reaches and the sediment settling in the reservoirs. The determination of the equation parameters is based on the observations on Doce River after the Fundão Dam collapse.

The result of the simulation shows that the tailings dams located in the Piracicaba River sub-basin have the highest potential to affect the water supply in the downstream towns. From the thirty-four dams located in this sub-basin, twenty-six dams have the potential to affect half million people or more. Ultimately, the collapse of only one specific dam in this sub-basin could affect almost one million people.

## 8. CONCLUSIONS

The main conclusions of this research are presented in accordance with the proposed objectives.

### Objective 1:

- a) The analysis of the available measurements carried out along Doce River enabled the validation of the one-dimensional advection-dispersion equation with sediment settling. The observed longitudinal dispersion coefficient  $K_d$  is in good agreement with the literature ( $K_d \approx 30 - 120 \text{ m}^2/\text{s}$ ) while the parameter  $k$  resulted in consistent values ( $k \approx 0.11 - 0.33 \text{ day}^{-1}$ ), indicating that the sediment settling rate relates to particle sizes from  $1.1 \text{ }\mu\text{m}$  to  $2.0 \text{ }\mu\text{m}$ , which is clearly associated with the finer sediment stored at Fundão Dam.
  
- b) The observed data and trap efficiency calculations carried out showed that the total volume trapped behind Candonga Dam and Baguari Dam immediately after the Fundão Dam collapse was  $7 \text{ Mm}^3$  and  $2 \text{ Mm}^3$ , respectively. These values correspond to reservoir volume loss of 17% in Candonga Dam and 5% in Baguari Dam. Volume losses for the other hydropower reservoirs were negligible.

### Objective 2:

- a) Several common flooding routing procedures (Modified Puls, Muskingum-Cunge, Preissmann, Crank Nicolson and QUICKEST scheme) were tested in the Doce River to simulate the flashy hydrographs after the Fundão Dam collapse.

All these existing methods presented unsatisfactory results, with an error in predicting the peak of up to 44%, and a time peak error up to 5 hours.

A new method to calculate floodwave propagation is proposed to solve the full dynamic-wave equation employing the new modified hydraulic diffusivity coefficient, which is function of the Froude number and floodwave celerity. Satisfactory numerical solution could be obtained by either the application of the Crank Nicolson or the QUICKEST scheme. Test of the new method on the Doce River presented an enhancement on the precision for prediction of the propagated hydrographs. The maximum error decreased from 44% to 2% for RPD, from 216 m<sup>3</sup>/s to 39 m<sup>3</sup>/s for RMSE, and from 32% to 11% for MAPE. The maximum difference found in time of peak was about 1 hour.

- b) A comprehensive numerical model was developed to calculate the suspended sediment transport along the Doce River and its reservoirs. This model solved the advection-dispersion equation with settling using the Crank Nicolson scheme. The calibrated model showed strong agreement with the observed sediment concentration data along the Doce River. Sediment deposition is also calculated using the Exner equation. This model can be used as a predictive tool for the simulation of other tailings dams collapse.

Objective 3:

- a) A parametric analysis was conducted using numerical model to determine the influence of varying temperature from 29°C (as measured) to 5°C, showing an increase in suspended sediment concentration up to 20,500 mg/l rather than 1,600 mg/l observed at the river mouth. This effect results from changes in kinematic viscosity and fall velocity due to variations in water temperature, which affects mainly the deposition of fine sediment. The analysis highlights that tailings dam spills are more critical in cold temperature zones, where the high concentration flow can be propagated along greater distances in the water bodies. In addition, hypothetical simulations without the hydropower reservoirs showed that the concentration at the Atlantic Ocean would increase from 1,600 mg/l to 70,000 mg/l, causing an extended shutdown in the water supply on the downs located in the lower part of the river.
  
- b) The simplified model was applied to simulate the hypothetical collapse of additional 56 tailings dams in the Doce River basin. Results show that the dams located in the Piracicaba River sub-basin are the most critical. Twenty-six dams located in this sub-basin have the potential to affect half million people or more. Ultimately, the collapse of only one specific dam in this sub-basin could affect almost one million people.

## REFERENCES

- Abbott, M. B., & Basco, D. R. (1990). *Computational Fluid Dynamics: An Introduction for Engineers*. New York: Longman Sc & Tech.
- Akan, A. O. (2006). *Open Channel Hydraulics* (1st edition). Burlington: Butterworth-Heinemann.
- ANA. (2016a). Encarte especial sobre a bacia do Rio Doce - Rompimento da barragem em Mariana/MG. *Conjuntura dos Recursos Hídricos no Brasil - Informe 2015*, 50.
- ANA. (2016b). *Relatório de Segurança de Barragens 2015* (p. 166). Brasília, Brazil: Agência Nacional de Águas, Ministério do Meio Ambiente.
- ANA. (2016c). SAR - Sistema de Acompanhamento de Reservatórios. Retrieved April 11, 2016, from <http://sar.ana.gov.br/>
- ANA. (2017). HidroWeb. Retrieved June 23, 2017, from <http://hidroweb.ana.gov.br/default.asp>
- Antunes, M. (2015). *Revista Mineração & Sustentabilidade*, 25(As lições de uma tragédia), 29–31.
- Armanini, A., Fraccarollo, L., & Rosatti, G. (2009). Two-dimensional simulation of debris flows in erodible channels. *Computers & Geosciences*, 35(5), 993–1006.
- Ávila, J. P. (2016). *Acidentes em Barragens de Rejeitos no Brasil*. Governo do Estado de São Paulo, Brazil - Secretaria de Energia e Mineração. Retrieved from <http://www.energia.sp.gov.br/wp-content/uploads/2016/07/ACIDENTES-EM-BARRAGENS-Joaquim-Pimenta-Pimenta-de-%C3%81vila-Engenharia.pdf>
- Ayala-Carcedo, F. J. (1998). La rotura de la balsa de residuos mineros de Aznalcóllar (España) de 1998 y el desastre ecológico consecuente del río Guadiamar: causas, efectos y lecciones. *Boletín Geológico y Minero*, 115, 711–738.
- Azam, S., & Li, Q. (2010). Tailings Dam Failures: A Review of the Last One Hundred Years. *Geotechnical News Magazine*, 28(4), 50–53.

- Baker, D. B., Richards, R. P., Loftus, T. T., & Kramer, J. W. (2004). A New Flashiness Index: Characteristics and Applications to Midwestern Rivers and Streams<sup>1</sup>. *JAWRA Journal of the American Water Resources Association*, 40(2), 503–522.
- Barbosa, E. F. (2010). *Diversidade e Composicao da Mirmecofaunda como Indicadora de Regeneracao de Areas Ciliares em Empreendimentos Hidretricos*. Universidade Federal de Juiz de Fora, Juiz de Fora, Brazil.
- Battjes, J. A., & Labeur, R. J. (2017). *Unsteady Flow in Open Channels* (1st edition). Cambridge, United Kingdom: Cambridge University Press.
- BBC. (2019). Brazil dam collapse mine chief steps down. Retrieved March 6, 2019, from <https://www.bbc.com/news/business-47432134>
- Biló, G. (2015). Moradores relatam saques e desespero por água mineral em Governador Valadares. Retrieved August 13, 2017, from <http://www.gazetaonline.com.br/noticias/brasil/2015/11/moradores-relatam-saques-e-desespero-por-agua-mineral-em-governador-valadares-1013914447.html>
- Burritt, R. L., & Christ, K. L. (2018). Water risk in mining: Analysis of the Samarco dam failure. *Journal of Cleaner Production*, 178, 196–205.
- Caldwell, J. A., Oboni, F., & Oboni, C. (2015). Tailings facility failures in 2014 and an update on failure statistics. In *Proceedings Tailings and Mine Waste 2015*. Vancouver.
- Cappelaere, B. (1997). Accurate Diffusive Wave Routing. *Journal of Hydraulic Engineering*, 123(3), 174–181.
- Carmo, F. F. do, Kamino, L. H. Y., Junior, R. T., Campos, I. C. de, Carmo, F. F. do, Silvino, G., Castro, K. J. da S. X. de, Mauro, M. L., Rodrigues, N. U. A., Miranda, M. P. de S., & Pinto, C. E. F. (2017). Fundação tailings dam failures: the environment tragedy of the largest technological disaster of Brazilian mining in global context. *Perspectives in Ecology and Conservation*. Retrieved July 31, 2017, from <http://www.sciencedirect.com/science/article/pii/S1679007316301566>

- Carr, M. L., & Rehmann, C. R. (2007). Estimating the Dispersion Coefficient with an Acoustic Doppler Current Profiler. *Journal of Hydraulic Engineering, ASCE*, 133(8), 977–982.
- CBDB. (2011). *A História das Barragens no Brasil, Séculos XIX, XX e XXI : cinquenta anos do Comitê Brasileiro de Barragens* (First). Rio de Janeiro, Brazil: Sindicato Nacional dos Editores de Livros.
- Cecen, K. M. (1969). Distribution of Suspended Matter and Similarity Criteria in Settling Basins. In *Proceedings 13th Congress IAHR* (Vol. 4, pp. 215–225). Kyoto.
- CEMIG. (2018). Usinas em Consorcio - CEMIG. Retrieved from [http://www.cemig.com.br/pt-br/a\\_cemig/Nossa\\_Historia/Paginas/Consortorios.aspx](http://www.cemig.com.br/pt-br/a_cemig/Nossa_Historia/Paginas/Consortorios.aspx)
- Chambers, D. M., & Higman, B. (2011). Long term risks of tailings dam failure. U.S National Park Service. Retrieved from [http://www.csp2.org/files/reports/Long% 20Term%20Risks %20of%20Tailings%20Dam%20Failure%20-%20Chambers%20%26%20Higman%20Oct11-2.pdf](http://www.csp2.org/files/reports/Long%20Term%20Risks%20of%20Tailings%20Dam%20Failure%20-%20Chambers%20%26%20Higman%20Oct11-2.pdf)
- Chang, C.-L., & Liao, C.-S. (2012). Assessing the risk posed by high-turbidity water to water supplies. *Environmental Monitoring and Assessment*, 184(5), 3127–3132.
- Chanson, H. (2004). *Environmental Hydraulics for Open Channel Flows* (1st edition). Amsterdam ; Boston: Butterworth-Heinemann.
- Chapra, S. C. (2008). *Surface Water-Quality Modeling*. Long Grove, Ill: McGraw-Hill.
- Chaudhry, M. H. (2007). *Open-Channel Flow* (2nd edition). New York, NY: Springer.
- Chow, V. T. (1988). *Applied Hydrology* (International Ed edition). New York: McGraw-Hill Publishing Company.
- Clemente, J. L. M., Snow, R. E., Bernedo, C., Strachan, C. L., & Fourie, A. (2013). Dam Break Analysis Applied to Tailings Dam: USSD Workshop Summary and Perspectives. In *Changing Times - The Challenges and Risks of Managing Aging Infrastructure Under a New Financial Reality*. Phoenix.

- Consórcio Candonga. (2018). Usina Hidrelétrica Risoleta Neves - UHE — Consórcio Candonga. Retrieved June 13, 2018, from <http://www.candonga.com.br>
- Consórcio UHE Baguari. (2018). Consórcio UHE Baguari. Retrieved June 13, 2018, from <http://www.uhebaguari.com.br>
- Cortez, J. R. (2013). *Desempenho de Modelos Numéricos em Estudos de Assoreamento de Reservatórios – Caso UHE Aimorés*. (Master thesis). UFMG, Belo Horizonte, Brazil.
- Costa, J. E. (1985). *Floods from dam failures* (USGS Numbered Series No. 85–560). U.S. Geological Survey. Retrieved March 6, 2018, from <http://pubs.er.usgs.gov/publication/ofr85560>
- CPRM, & ANA. (2015a). *Monitoramento Especial da Bacia do Rio Doce* (Acompanhamento da onda de cheia No. I) (p. 33). Belo Horizonte, Brazil: Serviço Geológico do Brasil - Agência Nacional de Águas.
- CPRM, & ANA. (2015b). *Monitoramento Especial da Bacia do Rio Doce* (Geoquímica No. II) (p. 35). Belo Horizonte, Brazil: Serviço Geológico do Brasil - Agência Nacional de Águas.
- CPRM, & ANA. (2016a). *Monitoramento Especial da Bacia do Rio Doce* (Hidrometria, Sedimentometria e Qualidade da Água nas Estações Fluviométricas da RHN após a Ruptura da Barragem de Rejeito No. IV) (p. 61). Belo Horizonte, Brazil: Serviço Geológico do Brasil - Agência Nacional de Águas.
- CPRM, & ANA. (2016b). *Monitoramento Especial da Bacia do Rio Doce* (Monitoramento Simultâneo ao longo de 15 dias No. IIII) (p. 84). Belo Horizonte, Brazil: Serviço Geológico do Brasil - Agência Nacional de Águas.
- Cui, Y., & Parker, G. (2005). Numerical Model of Sediment Pulses and Sediment-Supply Disturbances in Mountain Rivers. *Journal of Hydraulic Engineering*, 131(8), 646–656.
- Cunge, J. A., Holly, F. M., & Verwey, A. (1980). *Practical aspects of computational river hydraulics*. Pitman Advanced Publishing Program.

- D'Agostino, L. F. (2008). *Praias de Barragens de Rejeitos de Mineração: Características e Análise de Sedimentação* (Doctoral thesis). Escola Politécnica da Universidade de São Paulo, São Paulo, Brazil.
- Davies, M. (2002). Tailings impoundment failures: are geotechnical engineers listening? *Geotechnical News*, 20, 31–36.
- Davies, M., Marting, T., & Peter, L. (2000). *Mine Tailings Dams: When Things Go Wrong* (Association of State Dam Safety Officials, U.S. Committee on Large Dams) (pp. 261–273). Las Vegas: U.S. Committee on Large Dams. Retrieved from <http://www.infomine.com/library/publications/docs/Davies 2002d.pdf>
- Deng, Z.-Q., Singh, V. P., & Bengtsson, L. (2001). Longitudinal Dispersion Coefficient in Straight Rivers. *Journal of Hydraulic Engineering, ASCE*, 127(11), 919–927.
- DNPM. (2017). Cadastro Nacional de Barragens de Mineração. Retrieved from <http://www.dnpm.gov.br/assuntos/barragens/cadastro-nacional-de-barragens-de-mineracao>
- Elder, J. W. (1959). The dispersion of marked fluid in turbulent shear flow. *Journal of Fluid Mechanics*, 5(4), 544–560.
- EPA. (2014). An Assessment of Potential Mining Impacts on Salmon Ecosystems of Bristol Bay, Alaska (Final Report) [Reports & Assessments]. Retrieved May 24, 2017, from <https://cfpub.epa.gov/ncea/bristolbay/recordisplay.cfm?deid=253500>
- Faria, M. (2015). Barragens de rejeito já causaram diversas tragédias em Minas Gerais; relembre. Retrieved from [http://www.em.com.br/app/noticia/gerais/2015/11/05/interna\\_gerais,705019/barragens-de-rejeito-ja-causaram-diversas-tragedias-em-minas-gerais-r.shtml](http://www.em.com.br/app/noticia/gerais/2015/11/05/interna_gerais,705019/barragens-de-rejeito-ja-causaram-diversas-tragedias-em-minas-gerais-r.shtml)
- Fenton, J. D. (2011). Accuracy of Muskingum-Cunge flood routing [Alternative Hydraulics]. Retrieved from <http://johndfenton.com/Alternative-Hydraulics.html>

- Fernandes, G. W., Goulart, F. F., & Ranieri, B. D. (2016). Deep into the mud: ecological and socio-economic impacts of the dam breach in Mariana, Brazil. *Natureza & Conservação*, 14(2), 35–45.
- Fischer, H. B., List, E. J., Koh, R. C. Y., Imberger, J., & Brooks, N. H. (1979). *Mixing in Inland and Coastal Waters* (1 edition). New York: Academic Press.
- Garcia, L. C., Ribeiro, D. B., Roque, F. de O., Ochoa-Quintero, J. M., & Laurance, W. F. (2017). Brazil's worst mining disaster: Corporations must be compelled to pay the actual environmental costs. *Ecological Applications*, 27(1), 5–9.
- Geonetwork. (2007). Portal Metadados ANA - Geonetwork [InteractiveResource]. Retrieved June 23, 2017, from <http://metadados.ana.gov.br/geonetwork/srv/pt/main.home>
- Gilbert, G. K. (1917). *Hydraulic-mining Débris in the Sierra Nevada*. U.S. Government Printing Office.
- Google. (2015). Google Earth Pro (Version 7.1.5.1557). Google.
- Google. (2018). Google Earth Pro (Version 7.3.2.5491 (64-bit)) [Microsoft Windows (6.2.9200.0)]. Google. Retrieved from <https://www.google.com/earth/>
- Gran, K. B., & Czuba, J. A. (2017). Sediment pulse evolution and the role of network structure. *Geomorphology*, 277, 17–30.
- Hayami, S. (1951). *On the Propagation of Flood Waves* (Disaster Prevention Research Institute No. Bulletin 1) (pp. 12–20). Kyoto: Kyoto University.
- IBAMA. (2016). Instituto Brasileiro do Meio Ambiente e dos Recursos Naturais Renováveis. Retrieved from [http://www.ibama.gov.br/phocadownload/emergenciasambientais/respostas\\_deliberacao\\_3\\_e\\_4\\_do\\_cif.pdf](http://www.ibama.gov.br/phocadownload/emergenciasambientais/respostas_deliberacao_3_e_4_do_cif.pdf)
- IBGE. (2010). Instituto Brasileiro de Geografia e Estatística. Retrieved July 17, 2018, from <https://www.ibge.gov.br/>

- ICOLD. (2001). *Tailings Dams Risk of Dangerous Occurrences, Lessons learnt from practical experiences* (Bulletin 121) (p. 145). Paris, France: ICOLD Committee on Tailings Dams and Waste Lagoons.
- IPEA. (2012). *Diagnóstico dos Resíduos Sólidos da Atividade de Mineração de Substâncias Não Energéticas* (Research Report) (p. 40). Brasília, Brazil: Instituto de Pesquisa Econômica Aplicada. Retrieved June 1, 2017, from <http://www.ipea.gov.br>
- Iseya, F., & Ikeda, H. (1987). Pulsations in Bedload Transport Rates Induced by a Longitudinal Sediment Sorting: A Flume Study using Sand and Gravel Mixtures. *Geografiska Annaler: Series A, Physical Geography*, 69(1), 15–27.
- Iwasa, Y., & Aya, S. (1991). Predicting longitudinal dispersion coefficient in open channel flows. In *Proceedings of International Symposium on Environmental Hydraulics* (pp. 505–510). Hong Kong.
- Jain, S. C. (2001). *Open-Channel Flow* (1st ed.). Canada: Wiley. Retrieved June 12, 2018, from <https://www.amazon.com/Open-Channel-Flow-Subhash-C-Jain-ebook/dp/B000UHLQ74>
- Jeyapalan, J. K., Duncan, J. M., & Seed, H. B. (1983). Investigation of Flow Failures of Tailings Dams. *Journal of Geotechnical Engineering, ASCE*, 109(2), 172–189.
- Jin, M., & Fread, D. L. (1999). 1D modeling of mud/debris unsteady flows. *Journal of Hydraulic Engineering, ASCE*, 125, 827–834.
- Julien, P. Y. (2010). *Erosion and sedimentation* (2nd edition). Cambridge: Cambridge University Press.
- Julien, P. Y. (2018). *River Mechanics* (2nd edition). Cambridge, United Kingdom: Cambridge University Press.
- Kashefipour, S. M., & Falconer, R. A. (2002). Longitudinal dispersion coefficients in natural channels. *Water Research*, 36(6), 1596–1608.
- Kim, H. Y. (2016). *Optimization of Sangju Weir Operations to Mitigate Sedimentation Problems*. Colorado State University, Fort Collins.

- Koliji, A. (2018). Geotechdata.info. Retrieved December 11, 2018, from <http://www.geotechdata.info/parameter/soil-porosity.html>
- Kossoff, D., Dubbin, W. E., Alfredsson, M., Edwards, S. J., Macklin, M. G., & Hudson-Edwards, K. A. (2014). Mine tailings dams: Characteristics, failure, environmental impacts, and remediation. *Applied Geochemistry*, *51*, 229–245.
- Koussis, A. D., & Rodríguez, J. M. (1998). Hydraulic Estimation of Dispersion Coefficient for Streams. *Journal of Hydraulic Engineering*, *124*(3), 317–320.
- Kunkel, J. (2011). Downstream Modeling of Tailings Flow from Failure of a 380-ft High Tailing Dam. Presented at the USSD Workshop, Denver.
- Leonard, B. P. (1979). A stable and accurate convective modelling procedure based on quadratic upstream interpolation. *Computer Methods in Applied Mechanics and Engineering*, *19*(1), 59–98.
- Li, Z. H., Huang, J., & Li, J. (1998). Preliminary study on longitudinal dispersion coefficient for the gorges reservoir. In *Proceedings of the Seventh International Symposium Environmental Hydraulics* (pp. 16–18). Hong Kong.
- Lin, J., & Li, J. (2012). Tailings Dam Break Flow and Sediment Numerical Simulation. In *Civil Engineering and Urban Planning 2012 Proceedings* (pp. 677–683). Yantai, China: ASCE.
- Liu, H. (1977). Predicting Dispersion Coefficient of Streams. *Journal of the Environmental Engineering Division*, *103*(1), 59–69.
- Liu, H. (2018). *An Experimental and Numerical Study of Runout from a Tailings Dam Failure* (PhD Thesis). University of Western Australia, Perth. Retrieved from [https://api.research-repository.uwa.edu.au/portalfiles/portal/26431245/THESIS\\_DOCTOR\\_OF\\_PHILOSOPHY\\_LIU\\_Huiting\\_2018.pdf](https://api.research-repository.uwa.edu.au/portalfiles/portal/26431245/THESIS_DOCTOR_OF_PHILOSOPHY_LIU_Huiting_2018.pdf)
- Lucas, C. (2001). The Baia Mare and Baia Borsa Accidents: Cases of Severe Transboundary Water Pollution. *Environmental Policy and Law*, *31*(2), 106–111.

- Lucia, P., Duncan, M., & Seed, H. B. (1981). Summary on Research on Case Histories of Flow Failure of Mine Tailings Impoundment. In *Mine Waste Disposal Technology Proceedings*. Denver.
- Luz, S. J. (2015). Rompimento de barragens em MG destruiu 158 das 180 casas de vilarejo. Retrieved January 26, 2018, from <http://g1.globo.com/minas-gerais/noticia/2015/11/rompimento-de-barragens-em-mg-destruiu-158-das-180-casas-de-vilarejo.html>
- Machado, N. C. (2017). *Retroanálise da propagação decorrente da ruptura da barragem do fundão com diferentes modelos numéricos e hipóteses de simulação* (Master thesis). Universidade Federal de Minas Gerais, Escola de Engenharia, Belo Horizonte, Brazil.
- Machado, V. (2015). Colatina interrompe captação no Rio Doce após novas análises. Retrieved June 5, 2018, from <http://g1.globo.com/espírito-santo/noticia/2015/11/colatina-interrompe-captacao-no-rio-doce-apos-novas-analises.html>
- Mahmood, V., & Yevjevich, V. (1975). *Unsteady Flow in Open Channels* (Vol. 1). Fort Collins: Water Resources Publications.
- Marsooli, R., McGrath, M., & Altinakar, M. (2013). 2-D Numerical Modeling of Tailings Dam Failure. Presented at the Mid-South Annual Engineering and Science Conference, Oxford, Mississippi, USA.
- Marta-Almeida, M., Mendes, R., Amorim, F. N., Cirano, M., & Dias, J. M. (2016). Fundão Dam collapse: Oceanic dispersion of River Doce after the greatest Brazilian environmental accident. *Marine Pollution Bulletin*, 112(1), 359–364.
- Martins, L. T. (2015). Nota sobre o rompimento das barragens de rejeitos localizadas nos municípios de Mariana e Ouro preto (MG). Retrieved from <http://www.cbhdoce.org.br/geral/nota-sobre-o-rompimento-das-barragens-de-rejeitos-localizadas-nos-municipios-de-mariana-e-ouro-preto-mg>
- McCuen, R. H. (2016). *Hydrologic Analysis and Design* (4 edition). Boston: Pearson.

- McQuivey, R. S., & Keefer, T. N. (1974). Simple Method for Predicting Dispersion in Streams. *Journal of the Environmental Engineering Division, ASCE*, 100(4), 997–1011.
- Melo, L. P. R. (2013). *Análise Comparativa de Metodologias de Previsão de Inundação Decorrente da Ruptura de Barragens de Rejeitos: Caso Hipotético da Barragem Tico-Tico* (Master thesis). Universidade Federal de Minas Gerais, Belo Horizonte, Brazil.
- Mesquita, J. L. (2015). Rio Doce: carta de repúdio por nomeação política. Retrieved April 26, 2018, from <https://marsemfim.com.br/rio-doce-a-morte-de-um-corpo-dagua/>
- Milliman, J. D., & Farnsworth, K. L. (2013). *River Discharge to the Coastal Ocean: A Global Synthesis* (Reprint edition). Cambridge University Press.
- Moin, P. (2010). *Fundamentals of Engineering Numerical Analysis* (2nd edition). Cambridge: Cambridge University Press.
- Moraes, R. (2015). Mining waste reaches Brazilian coast two weeks after BHP dam collapse. Retrieved September 7, 2017, from <https://www.theguardian.com/world/2015/nov/23/brazil-dam-collapse-mining-waste-reaches-ocean-rio-doce>
- Morgenstern, N. R., Vick, S. G., Viotti, C. B., & Watts, B. D. (2016). *Report on the Immediate Causes of the Failure of the Fundão Dam* (p. 76). Cleary Gottlieb Steen & Hamilton LLP. Retrieved June 4, 2017, from <http://fundaoinvestigation.com/>
- Noori, R., Ghiasi, B., Sheikhan, H., & Adamowski, J. F. (2017). Estimation of the Dispersion Coefficient in Natural Rivers Using a Granular Computing Model. *Journal of Hydraulic Engineering*, 143(5), 04017001.
- O'Brien, J. S., & Julien, P. Y. (1985). Physical properties and mechanics of hyperconcentrated sediment flows. In *Delineation of Landslide, Flash Flood, and Debris Flow Hazards in Utah* (pp. 290–279). Utah: Civil and Environmental Engineering Commons and the Water Resource Management Commons. Retrieved from [http://digitalcommons.usu.edu/water\\_rep/596](http://digitalcommons.usu.edu/water_rep/596)

- O'Brien, J. S., Julien, P. Y., & Fullerton, W. T. (1993). Two-Dimensional Water Flood and Mudflow Simulation. *Journal of Hydraulic Engineering, ASCE*, 119, 244–261.
- ONS. (2017). Operador Nacional do Sistema Elétrico. Retrieved June 23, 2017, from [http://ons.org.br/Paginas/resultados-da-operacao/historico-da-operacao/dados\\_hidrologicos\\_vazoes.aspx](http://ons.org.br/Paginas/resultados-da-operacao/historico-da-operacao/dados_hidrologicos_vazoes.aspx)
- Pickup, G., Higgins, R. J., & Grant, I. (1983). Modelling sediment transport as a moving wave — The transfer and deposition of mining waste. *Journal of Hydrology*, 60(1), 281–301.
- Pimentel, T. (2016). Usina afetada por lama da Samarco fecha comportas para limpeza em MG. Retrieved December 3, 2018, from <http://g1.globo.com/minas-gerais/desastre-ambiental-em-mariana/noticia/2016/06/usina-afetada-por-lama-da-samarco-fecha-comportas-para-limpeza-em-mg.html>
- Press, W. H., Teukolsky, S. A., Vetterling, W. T., & Flannery, B. P. (2007). *Numerical Recipes 3rd Edition: The Art of Scientific Computing* (3rd edition). Cambridge, UK: Cambridge University Press.
- Price, R. K. (2009). Volume-Conservative Nonlinear Flood Routing. *Journal of Hydraulic Engineering*, 135(10), 838–845.
- Ramirez, J. A. (2015). Basic Hydrology. Retrieved from [http://www.engr.colostate.edu/~ramirez/ce\\_old/classes/cive322-Ramirez/CE322\\_Web/Example\\_LevelPoolRouting.htm](http://www.engr.colostate.edu/~ramirez/ce_old/classes/cive322-Ramirez/CE322_Web/Example_LevelPoolRouting.htm)
- Reid, I., Frostick, L., & Layman, J. (1985). The incidence and nature of bedload transport during flood flows in coarse-grained alluvial channels. *Earth Surface Processes and Landforms*, 10, 33–44.
- Renova. (2018). Manejo de Rejeitos. Retrieved April 29, 2018, from <http://www.fundacaorenova.org/manejo-de-rejeitos/>
- Rezende, V. A. (2013). *Estudo do Comportamento de Barragem de Rejeito Arenoso Alteada por Montante* (Masters thesis). Universidade Federal de Ouro Preto, Ouro Preto, Brazil.

- Rickenmann, D., Laigle, D., McArdell, B. W., & Hübl, J. (2006). Comparison of 2D debris-flow simulation models with field events. *Computational Geosciences*, 10(2), 241–264.
- Rico, M., Benito, G., & Díez-Herrero, A. (2008). Floods from tailings dam failures. *Journal of Hazardous Materials*, 154(1–3), 79–87.
- Roberson, J. A., Cassidy, J. J., & Chaudhry, M. H. (1998). *Hydraulic Engineering* (3rd edition). New York: Wiley.
- Roberto, C. (2016). UHE Baguari volta a operar após rompimento da barragem da Samarco [Notícias]. Retrieved from <https://fullenergy.grupomidia.com/uhe-baguari-volta-a-operar-apos-rompimento-da-barragem-da-samarco/>
- Rocha, F. F. (2016). *Cenários de Formação e Evolução de Rupturas em Barragens de Rejeitos (Dam Break)*. Presented at the SEA – Seminário de Emergência Ambiental, Minas Gerais. Retrieved May 25, 2017, from [http://www.meioambiente.mg.gov.br/images/stories/2016/ASCOM\\_DIVERSOS/01\\_-\\_Semin%C3%A1rio\\_Emerg%C3%Aancia\\_Ambiental\\_-\\_Dam\\_Break\\_-\\_Felipe\\_Rocha.pdf](http://www.meioambiente.mg.gov.br/images/stories/2016/ASCOM_DIVERSOS/01_-_Semin%C3%A1rio_Emerg%C3%Aancia_Ambiental_-_Dam_Break_-_Felipe_Rocha.pdf)
- Rutherford, J. C. (1994). *River Mixing* (1st edition). Chichester England ; New York: Wiley.
- Santos, C. (2015). Povoado que fugiu de enchente é coberto de lama. Retrieved April 26, 2018, from <https://noticias.uol.com.br/album/2015/11/08/povoado-que-fugiu-de-enchente-e-coberto-de-lama.htm>
- Schamber, D., & MacArthur, R. (1985). One Dimensional Model for Mud Flows. In *Proceedings of ASCE Hydraulic Division Specialty Conference on Hydraulics and Hydrology in the Small Computer Age* (pp. 1–14). Orlando, FL: USACE.
- Seo, I. W., & Cheong, T. S. (1998). Predicting Longitudinal Dispersion Coefficient in Natural Streams. *Journal of Hydraulic Engineering, ASCE*, 124(1), 25–32.
- Shen, H. W. (Ed.). (1971). *River Mechanics, Vol. 1*. Water Resources Publication.

- Simon, C. (2015). Máquinas são usadas em buscas por desaparecidos em Bento Rodrigues. Retrieved November 12, 2015, from <http://g1.globo.com/minas-gerais/noticia/2015/11/maquinas-sao-usadas-em-buscas-por-desaparecidos-em-bento-rodrigues.html>
- Singh, V. P. (1996). *Kinematic Wave Modeling in Water Resources, Surface-Water Hydrology* (1 edition). New York: Wiley-Interscience.
- Sturm, T. W. (2009). *Open Channel Hydraulics* (2nd edition). Dubuque, IA: McGraw-Hill Education.
- Szymkiewicz, R. (2010). *Numerical Modeling in Open Channel Hydraulics* (1st edition). New York: Springer.
- Tayfur, G., & Singh, V. P. (2005). Predicting Longitudinal Dispersion Coefficient in Natural Streams by Artificial Neural Network. *Journal of Hydraulic Engineering, ASCE*, 131(11), 991–1000.
- Tschiedel, A. . (2016). Modelagem Hidrológica Chuva-Vazão Na Bacia do Rio Docea Partir do Modelo MGB-IPH. In *Proceedings of 10 Simpósio Internacional de Qualidade Ambiental*. Porto Alegre, Brazil.
- UOL. (2015). Rejeitos avançam pela Usina Hidrelétrica de Mascarenhas. Retrieved from <https://noticias.uol.com.br/cotidiano/ultimas-noticias/2015/11/18/rejeitos-avancam-pela-usina-hidreletrica-de-mascarenhas.htm>
- USACE. (2016). HEC-RAS User's Manual (Version 5.0). Davis, California: US Army Corps of Engineers - Hydrologic Engineering Center.
- USBR. (2015). *Technical Evaluation of the Gold King Mine Incident* (p. 132). Denver: USBR.
- USGS. (2019). Turbidity [Water Properties,]. Retrieved March 6, 2019, from <https://water.usgs.gov/edu/turbidity.html>
- Versteeg, H., & Malalasekera, W. (2007). *An Introduction to Computational Fluid Dynamics: The Finite Volume Method* (2 edition). Harlow, England ; New York: Pearson.

- WISE. (2019). Chronology of major tailings dam failures. Retrieved May 26, 2017, from <http://www.wise-uranium.org/mdaf.html>
- Wohl, E. (2014). *Rivers in the Landscape: Science and Management* (1 edition). Hoboken, NJ: Wiley-Blackwell.
- Wu, J., Bao, K., & Zhang, H. (2011). Research progress on dam-break floods. In *2011 2nd IEEE International Conference on Emergency Management and Management Sciences* (pp. 334–338).
- Wu, W. (2007). *Computational River Dynamics*. London ; New York: CRC Press.
- Yang, Y., Endreny, T. A., & Nowak, D. J. (2016). Application of advection-diffusion routing model to flood wave propagation: A case study on Big Piney River, Missouri USA. *Journal of Earth Science*, 27(1), 9–14.
- Zeng, Y., & Huai, W. (2014). Estimation of longitudinal dispersion coefficient in rivers. *Journal of Hydro-Environment Research*, 8(1), 2–8.

APPENDIX A

Measured data of Suspended Sediment Concentration and Turbidity

**Table A1 – Measured suspended sediment concentration and turbidity (CPRM & ANA, 2015)**

Station	Date	Concentration (mg/l)	Turbidity (NTU)
G6	11/7/2015 8:00	118,396	181,200
	11/7/2015 9:00	239,030	311,600
	11/7/2015 12:00	418,848	567,600
	11/7/2015 13:00	387,388	635,600
	11/7/2015 14:00	397,428	822,000
	11/9/2015 12:00	53,820	-
	11/9/2015 12:00	53,820	-
	11/10/2015 12:00	29,680	-
	11/11/2015 12:00	10,280	-
	11/12/2015 12:00	860	-
G5	11/8/2015 7:00	301,692	414,800
	11/8/2015 8:00	304,594	430,000
	11/8/2015 9:00	298,060	446,800
	11/10/2015 12:00	28,520	-
	11/11/2015 12:00	29,540	-
G4	11/10/2015 8:00	36,240	82,160
	11/10/2015 9:00	33,728	57,360
	11/10/2015 10:00	39,040	91,680
	11/10/2015 11:00	47,582	119,360
	11/10/2015 12:00	50,942	116,200
	11/10/2015 14:00	49,372	113,520
	11/10/2015 15:00	49,490	104,040
	11/10/2015 17:00	46,700	93,960
	11/10/2015 18:00	46,718	90,560
	11/12/2015 8:00	12,422	-
11/13/2015 12:00	1,190	-	
G3	11/11/2015 10:00	1,298	2,243
	11/11/2015 11:00	2,598	3,368
	11/11/2015 12:00	3,174	5,932
	11/11/2015 13:00	3,374	5,572
	11/11/2015 14:00	4,162	8,440
	11/11/2015 15:00	4,822	9,160
	11/11/2015 16:00	6,636	13,680
	11/11/2015 17:00	14,022	27,260
	11/11/2015 18:00	21,270	49,460
	11/12/2015 11:00	31,056	-

Station	Date	Concentration (mg/l)	Turbidity (NTU)
S4	11/13/2015 9:45	1,356	2,172
	11/13/2015 11:00	1,876	3,266
	11/13/2015 12:00	1,994	3,694
	11/13/2015 13:00	2,402	3,724
	11/13/2015 15:00	3,130	6,300
	11/13/2015 17:00	3,466	4,960
	11/15/2015 11:00	7,706	-
	11/15/2016 10:00	3,504	-
S3	11/17/2015 8:20	2,726	8,420
	11/17/2015 10:30	2,968	8,620
	11/17/2015 11:30	3,190	9,720
	11/17/2015 13:00	3,170	9,160
	11/17/2015 14:00	3,258	10,180
	11/17/2015 15:00	3,202	9,740
	11/17/2015 20:30	3,508	11,400
	11/17/2015 20:45	3,338	-
	11/18/2015 9:00	2,802	-
S2	11/18/2015 10:00	898	2,640
	11/18/2015 12:00	1,238	3,120
	11/18/2015 14:00	1,484	4,120
	11/18/2015 16:00	1,476	4,760
	11/18/2015 18:00	1,648	4,840
	11/18/2015 18:00	1,770	-
	11/19/2015 8:30	2,358	8,600
G2	11/19/2015 9:30	1,208	3,240
	11/19/2015 10:30	1,266	3,260
	11/19/2015 11:30	1,556	3,720
	11/19/2015 14:00	1,704	4,820
	11/19/2015 15:00	1,726	4,340
	11/19/2015 16:00	1,730	4,260
	11/19/2015 17:00	1,726	4,660
	11/19/2015 18:00	1,834	5,080
	11/19/2015 18:00	2,044	-
	11/20/2015 7:30	2,226	6,740
G1	11/20/2015 16:00	204	474
	11/20/2015 18:30	376	2,960
	11/21/2015 8:00	1,144	5,680
	11/21/2015 20:00	1,530	-
S1	11/21/2015 14:30	90	193
	11/21/2015 15:00	157	346
	11/21/2015 16:30	218	471
	11/21/2015 16:30	252	-

Longitudinal Dispersion Coefficient

Table A2 – Literature Data

Number	Data Source	Stream	Width <i>W</i> (m)	Depth <i>h</i> (m)	Velocity <i>U</i> (m/s)	Shear velocity <i>u</i> * (m/s)	Disp. Coeff. <i>Kd</i> (m <sup>2</sup> /s)
1	a	Bayou Anacoco, LA	25.91	0.94	0.34	0.067	32.52
2	a		36.58	0.91	0.4	0.067	39.48
3	a	Nooksack River, WA	64.01	0.76	0.67	0.268	34.84
4	a	Wind Bighorn River, WY	59.44	1.1	0.88	0.119	41.81
5	a		68.58	2.16	1.55	0.168	162.58
6	a	John Day River, OR	24.99	0.58	1.01	0.14	13.94
7	a		34.14	2.47	0.82	0.18	65.03
8	a	Sabine River	103.6	2.04	0.56	0.054	315.87
9	a	Sabine River	127.4	4.75	0.64	0.081	668.9
10	a	Yadkin River, N.C.	70.1	2.35	0.43	0.101	111.48
11	a		71.63	3.84	0.76	0.128	260.13
12	a	Comite River	13	0.26	0.31	0.044	7
13	a		16	0.43	0.37	0.056	13.9
14	b	Copper Creek, VA. (below gage)	15.9	0.49	0.21	0.079	19.52
15	b		18.3	0.84	0.52	0.1	21.4
16	b		16.2	0.49	0.25	0.079	9.5
17	b	Clinch River, TN. (below gage)	46.9	0.86	0.28	0.067	13.93
18	b		59.4	2.13	0.86	0.104	53.88
19	b		53.3	2.09	0.79	0.107	46.45
20	b	Copper Creek, VA (above gage)	18.6	0.39	0.14	0.116	9.85
21	b	Power River, TN.	33.8	0.85	0.16	0.055	9.5
22	b	Clinch River, VA.	36	0.58	0.3	0.049	8.08
23	b	Coachella Canal, CA.	24.4	1.56	0.67	0.043	9.57
24	c	Miljacka	11	0.29	0.35	0.058	2.7
25	c	Upper Tame	9.9	0.83	0.46	0.09	5.5
26	c	Upper Tame	9.9	0.92	0.52	0.1	5.1
27	c	Punehu	5	0.28	0.26	0.21	7.2
28	c	Kapuni	9	0.3	0.37	0.15	8.4
29	c	Kapuni	10	0.35	0.53	0.17	12.4
30	c	Manganui	20	0.4	0.19	0.18	6.5
31	c	Vaiongana	13	0.6	0.48	0.24	6.8
32	c	Stony	10	0.63	0.55	0.3	13.5
33	c	Waiotapu	11.4	0.75	0.41	0.061	8
34	c	Manawatu	59	0.72	0.37	0.07	32
35	c	Manawatu	63	1	0.32	0.094	22
36	c	Manawatu	60	0.95	0.46	0.092	47
37	c	Tarawera	25	1.21	0.73	0.084	27
38	c		20	1.92	0.62	0.123	11.5
39	c		25	1.38	0.77	0.091	20.5
40	c		25	1.4	0.78	0.091	15.5
41	c	Waikato	25	1.57	0.83	0.096	18
42	c		85	2.6	0.69	0.06	52
43	c		120	2	0.64	0.05	67
44	d	Antietam Creek, MD	12.8	0.3	0.42	0.057	17.5
45	d		24.08	0.98	0.59	0.098	101.5
46	d		11.89	0.66	0.43	0.085	20.9
47	d		21.03	0.48	0.62	0.069	25.9
48	d	Monocacy River, MD	48.7	0.55	0.26	0.052	37.8

Number	Data Source	Stream	Width $W$ (m)	Depth $h$ (m)	Velocity $U$ (m/s)	Shear velocity $u^*$ (m/s)	Disp. Coeff. $Kd$ (m <sup>2</sup> /s)
49	d		92.96	0.71	0.16	0.046	41.4
50	d		51.21	0.65	0.62	0.044	29.6
51	d		97.54	1.15	0.32	0.058	119.8
52	d		40.54	0.41	0.23	0.04	66.5
53	d	Conococheague Creek, MD	42.41	0.69	0.23	0.064	40.8
54	d		49.68	0.41	0.15	0.081	29.3
55	d		42.98	1.13	0.63	0.081	53.3
56	d	Chattahoochee River, GA	75.59	1.95	0.74	0.138	88.9
57	d		91.9	2.44	0.52	0.094	166.9
58	d	Salt Creek, NE	32	0.5	0.24	0.038	52.2
59	d	Difficult Run, VA	14.48	0.31	0.25	0.062	1.9
60	d	Little Pincy Creek, MD	15.85	0.22	0.39	0.053	7.1
61	d	Bayou Anacoco, LA	17.53	0.45	0.32	0.024	5.8
62	d	Comite River, LA	15.7	0.23	0.36	0.039	69
63	d	Bayou Bartholomew, LA	33.38	1.4	0.2	0.031	54.7
64	d	Amite River, LA	21.34	0.52	0.54	0.027	501.4
65	d	Tickfau River, LA	14.94	0.59	0.27	0.08	10.3
66	d	Tangipahoa, River, LA	31.39	0.81	0.48	0.072	45.1
67	d		29.87	0.4	0.34	0.02	44
68	d	Red River, LA	253.59	1.62	0.61	0.032	143.8
69	d		161.54	3.96	0.29	0.06	130.5
70	d		152.4	3.66	0.45	0.057	227.6
71	d		155.14	1.74	0.47	0.036	177.7
72	d	Sabine River, LA	116.43	1.65	0.58	0.054	131.3
73	d		160.32	2.32	1.06	0.054	308.9
74	d	Sabine River, TX	14.17	0.5	0.13	0.037	12.8
75	d		12.19	0.51	0.23	0.03	14.7
76	d		21.34	0.93	0.36	0.035	24.2
77	d	Mississippi River, LA	711.2	19.94	0.56	0.041	237.2
78	d	Mississippi River, MO	533.4	4.94	1.05	0.069	457.7
79	d		537.38	8.9	1.51	0.097	374.1
80	d	Wind Bighorn River, WY	44.2	1.37	0.99	0.142	184.6
81	d		85.34	2.38	1.74	0.153	464.6
82	d	Copper Creep, VA	16.66	0.49	0.2	0.08	16.84
83	d	Clinch River, VA	48.46	1.16	0.21	0.069	14.76
84	d	Copper Creek, VA	18.29	0.38	0.15	0.116	20.71
85	d	Powell River, TE	36.78	0.87	0.13	0.054	15.5
86	d	Clinch River, VA	28.65	0.61	0.35	0.069	10.7
87	d	Copper River, VA	19.61	0.84	0.49	0.101	20.82
88	d	Clinch River, VA	57.91	2.45	0.75	0.104	40.49
89	d		53.24	2.41	0.66	0.107	36.93
90	d	Copper Creek, VA	16.76	0.47	0.24	0.08	24.62
91	d	Missouri River, IA	180.59	3.28	1.62	0.078	1486.45
92	d	Minnesota River	80	2.74	0.034	0.0024	22.3
93	d		80	2.74	0.14	0.0097	34.9
94	d	Amite River	37	0.81	0.29	0.07	23.2
95	d		42	0.8	0.42	0.069	30.2
96	d	White River	67	0.55	0.35	0.044	30.2
97	d	Chattahoochee River	65.5	1.13	0.39	0.075	32.52
98	d	Nooksack River	86	2.93	1.2	0.53	153
99	d	Susquehanna River	203	1.35	0.39	0.065	92.9
100	d	Bayou Anacoco	20	0.42	0.29	0.045	13.9

Number	Data Source	Stream	Width $W$ (m)	Depth $h$ (m)	Velocity $U$ (m/s)	Shear velocity $u^*$ (m/s)	Disp. Coeff. $Kd$ (m <sup>2</sup> /s)
101	d	Muddy Creek	13	0.81	0.37	0.081	13.9
102	d		20	1.2	0.45	0.099	32.5
103	d	Missouri River	183	2.33	0.89	0.066	465
104	d		201	3.56	1.28	0.084	837
105	d	Missouri River	197	3.11	1.53	0.078	892
106	d	Missouri River	200	2.7	1.55	0.074	1500
107	e	Bayou Anacoco, La	19.8	0.41	0.29	0.044	13.94
108	e	Nooksake River	86	2.94	1.2	0.514	153.29
109	e	Antietam Creek	15.8	0.39	0.32	0.06	9.29
110	e		19.8	0.52	0.43	0.069	16.26
111	e		24.4	0.71	0.52	0.081	25.55
112	e	Monocacy River	35.1	0.32	0.21	0.043	4.65
113	e		36.6	0.45	0.32	0.051	13.94
114	e		47.5	0.87	0.44	0.07	37.16
115	e	Missouri River	182.9	2.23	0.93	0.065	464.52
116	e	Missouri River	201.2	3.56	1.27	0.082	836.13
117	e	Wind Bighorn Rivers	67.1	0.98	0.88	0.11	41.81
118	e	Elkhorn River	32.6	0.3	0.43	0.046	9.29
119	e		50.9	0.42	0.46	0.046	20.9
120	e	Sabine River, TX	35.1	0.98	0.21	0.041	39.48
121	f	Embarrass river	30	1.1	0.38	0.025	35.9
122	f	Illinois River, Henry	158	4.3	0.19	0.007	48.9
123	f	Illinois River, Henry	232	3.4	0.24	0.043	52
124	f	Illinois River, Kingston	202	4.6	0.18	0.036	49.1
125	f	Illinois River, Kingston	194	6.3	0.22	0.039	537.7
126	f	Illinois River, Marseilles	183	5.7	0.11	0.02	13.3
127	f	Kanawha River	259	3.3	0.17	0.017	24.2
128	f		259	3.4	0.17	0.018	22.1
129	f	Missouri River	230	3.5	1.08	0.085	455.1
130	f		176	3.4	1.61	0.082	966.2
131	f		229	3.4	1.24	0.082	309.8
132	f	New River	102	4.4	0.17	0.008	22.4
133	f	Salt Creek	167	0.2	0.47	0.159	43.2
134	f	Sangamon River	27	1.1	0.44	0.007	24.6
135	f	Yampa River	78	1.2	1.42	0.026	325.6
136	f		300	0.3	1	0.029	349.6
137	f		300	0.4	0.97	0.032	227.7
138	f		76	1.2	1.41	0.058	116.4

Data source: a - McQuivey & Keefer (1974); b - Fischer et al (1979); c – Rutherford (1994);

d - Deng et al (2001); e - Kashefipour & Falconer (2002); f - Carr & Rehmann (2007).

## APPENDIX B

### Derivation of Diffusive Wave Approximation

Initially, the reduced momentum equation, the channel conveyance and the continuity equation previously presented are recalled:

$$S_f = S_o - \frac{\partial h}{\partial x} \quad (2.12)$$

$$Q = K \sqrt{S_f} \rightarrow S_f = \frac{Q^2}{K^2} \quad (5.9)$$

$$\frac{\partial h}{\partial t} + \frac{1}{W} \frac{\partial Q}{\partial x} = 0 \quad (5.10)$$

Equation 5.9 is substituted into Equation 2.12 and then differentiated with respect to time:

$$\frac{\partial h^2}{\partial x \partial t} + \frac{2|Q|}{K^2} \frac{\partial Q}{\partial t} - 2 \frac{Q|Q|}{K^3} \frac{\partial K}{\partial t} = 0 \quad (10.1)$$

The cross derivatives of  $h$  in Equation 10.1 can be eliminated by the differentiation of Equation 5.10 with respect to distance:

$$\frac{1}{W} \frac{\partial^2 Q}{\partial x^2} + \frac{\partial h^2}{\partial t \partial x} = 0 \quad (10.2)$$

The substitution of Equation 10.2 into Equation 10.1 leads to:

$$\left( -\frac{1}{W} \frac{\partial^2 Q}{\partial x^2} \right) + \frac{2|Q|}{K^2} \frac{\partial Q}{\partial t} - 2 \frac{Q|Q|}{K^3} \frac{\partial K}{\partial t} = 0 \quad (10.3)$$

Since the channel conveyance  $K$  is function of the depth, one can write:

$$\frac{\partial K}{\partial t} = \frac{\partial K}{\partial h} \frac{\partial h}{\partial t} \quad (10.4)$$

Substituting Equation 10.4 in the Equation 5.10 results in:

$$\frac{\partial K}{\partial t} = -\frac{\partial K}{\partial h} \frac{1}{W} \frac{\partial Q}{\partial x} \quad (10.5)$$

Then, substituting Equation 10.5 into Equation 10.3 leads to:

$$\left(-\frac{1}{W} \frac{\partial^2 Q}{\partial x^2}\right) + \frac{2|Q|}{K^2} \frac{\partial Q}{\partial t} - 2 \frac{Q|Q|}{K^3} \frac{\partial K}{\partial h} \left(-\frac{1}{W} \frac{\partial Q}{\partial x}\right) = 0 \quad (10.6)$$

After some manipulation and reorganizing the terms Equation 10.6 becomes:

$$\frac{\partial Q}{\partial t} + \left(\frac{Q}{KW} \frac{\partial K}{\partial h}\right) \frac{\partial Q}{\partial x} - \left(\frac{K^2}{2W|Q|}\right) \frac{\partial^2 Q}{\partial x^2} = 0 \quad (10.7)$$

For a wide rectangular channel  $K = (W/n)h^{5/3}$  and:

$$\frac{\partial K}{\partial h} = \frac{5W}{3n} h^{2/3} \quad (10.8)$$

Substituting Equations 10.8 and 5.9 into Equation 10.7 and considering the bed slope  $S_o$  equal to the energy line slope  $S_f$  one can get:

$$\frac{\partial Q}{\partial t} + \frac{5}{3} U \frac{\partial Q}{\partial x} = \frac{Q}{2WS_o} \frac{\partial^2 Q}{\partial x^2} \quad (10.9)$$

Finally, Equation 10.9 can be written in advection-dispersion form as:

$$\frac{\partial Q}{\partial t} + C_e \frac{\partial Q}{\partial x} - D \frac{\partial^2 Q}{\partial x^2} = 0 \quad (10.10)$$

## APPENDIX C

### The Preissmann Scheme

The Preissmann scheme is a popular implicit scheme for solution of the one-dimensional Navier Stokes Equation. Such scheme is given by (Szymkiewicz, 2010):

$$f_p \approx \frac{\theta}{2}(f_j^{n+1} + f_{j+1}^{n+1}) + \frac{(1-\theta)}{2}(f_j^n + f_{j+1}^n) \quad (10.11)$$

$$\left. \frac{\partial f}{\partial t} \right|_p \approx \frac{1}{2} \left( \frac{f_j^{n+1} - f_j^n}{\Delta t} + \frac{f_{j+1}^{n+1} - f_{j+1}^n}{\Delta t} \right) \quad (10.12)$$

$$\left. \frac{\partial f}{\partial x} \right|_p \approx (1-\theta) \frac{f_{j+1}^n - f_j^n}{\Delta x} + \theta \frac{f_{j+1}^{n+1} - f_j^{n+1}}{\Delta x} \quad (10.13)$$

Where  $\theta$  is the weight factor. One should note that the Preissmann scheme is unconditionally stable and first order accurate (both in space and in time) when  $0.5 \leq \theta \leq 1$ . The application of the Preissmann Scheme over the Saint Venant equation results in the discretized continuity (C) and momentum (M) equations, as follows:

$$\frac{1}{W_p} \left[ (1-\theta) \frac{Q_{j+1}^n - Q_j^n}{\Delta x} + \theta \frac{Q_{j+1}^{n+1} - Q_j^{n+1}}{\Delta x} \right] + \frac{1}{2} \left( \frac{h_j^{n+1} - h_j^n}{\Delta t} + \frac{h_{j+1}^{n+1} - h_{j+1}^n}{\Delta t} \right) = 0 \quad (10.14)$$

$$\begin{aligned} & \frac{1}{2} \left( \frac{Q_j^{n+1} - Q_j^n}{\Delta t} + \frac{Q_{j+1}^{n+1} - Q_{j+1}^n}{\Delta t} \right) + \frac{(1-\theta)}{\Delta x} \left[ \left( \frac{Q^2}{A} \right)_{j+1}^n - \left( \frac{Q^2}{A} \right)_j^n \right] + \frac{\theta}{\Delta x} \left[ \left( \frac{Q^2}{A} \right)_{j+1}^{n+1} - \left( \frac{Q^2}{A} \right)_j^{n+1} \right] \\ & + g \cdot A_p \left[ (1-\theta) \frac{h_{j+1}^n - h_j^n}{\Delta x} + \theta \frac{h_{j+1}^{n+1} - h_j^{n+1}}{\Delta x} \right] + \left( \frac{g \cdot n_M^2 |Q|Q}{R^{4/3} A} \right)_p \end{aligned} \quad (10.15)$$

$$+ g \cdot A_p \left[ (1-\theta) \frac{z_{j+1}^n - z_j^n}{\Delta x} + \theta \frac{z_{j+1}^{n+1} - z_j^{n+1}}{\Delta x} \right] = 0$$

Where:

$$A_p = \frac{\theta}{2}(A_j^{n+1} + A_{j+1}^{n+1}) + \frac{(1-\theta)}{2}(A_j^n + A_{j+1}^n) \quad (10.16)$$

$$W_p = \frac{\theta}{2}(W_j^{n+1} + W_{j+1}^{n+1}) + \frac{(1-\theta)}{2}(W_j^n + W_{j+1}^n) \quad (10.17)$$

$$\begin{aligned} \left(\frac{g \cdot n_M^2 |Q|Q}{R^{4/3} A}\right)_p &= \frac{\theta}{2} \left[ \left(\frac{g \cdot n_M^2 |Q|Q}{R^{4/3} A}\right)_j^{n+1} + \left(\frac{g \cdot n_M^2 |Q|Q}{R^{4/3} A}\right)_{j+1}^{n+1} \right] \\ &+ \frac{(1-\theta)}{2} \left[ \left(\frac{g \cdot n_M^2 |Q|Q}{R^{4/3} A}\right)_j^n + \left(\frac{g \cdot n_M^2 |Q|Q}{R^{4/3} A}\right)_{j+1}^n \right] \end{aligned} \quad (10.18)$$

Where  $S_0$  is the bed slope,  $W$  is the river width,  $h$  is the flow depth,  $n_M$  is the Manning roughness coefficient,  $j$  is the cross-section index and  $n$  is the time level index.

The application of Equations 10.14 and 10.15 for the nodes  $j = 1, 2, 3 \dots M - 1$  result in a system of  $2(M - 1)$  non-linear equations with  $2M$  unknowns ( $h_j^{n+1}, h_{j+1}^{n+1}, Q_j^{n+1}$  and  $Q_{j+1}^{n+1}$ ). Therefore, two boundary conditions (Equations B) are required to complete the system. In this algorithm the upstream boundary condition is the hydrograph, given by Equation 10.19 while for downstream it is the normal depth, as showed in Equation 10.20.

$$Q_1^{n+1} - Q_{obs}^{n+1} = 0 \quad (10.19)$$

$$(Sf)_M^{n+1} = S_0 \rightarrow Q_M^{n+1} = \sqrt{\left(\frac{S_0 h^{10/3} B^2}{n_M^2}\right)_M^{n+1}} \quad (10.20)$$

Herein, the initial condition considers a uniform depth for a given initial discharge. Thus, the solution for this system of non-linear equations can be achieved using the Newton-Raphson method, as presented below:

$$\mathbf{J}^{(\kappa)} \cdot \Delta \mathbf{X}^{(\kappa+1)} = -\mathbf{R}^{(\kappa)} \quad (10.21)$$

Where  $\kappa$  is the index of iteration,  $\mathbf{J}^{(\kappa)}$  is the Jacobian matrix,  $\Delta \mathbf{X}^{(\kappa+1)}$  is the correction vector, and  $\mathbf{R}^{(\kappa)}$  is the residual matrix, i.e. the resultant value after the application of the calculated values of the ( $h_j^{n+1}, h_{j+1}^{n+1}, Q_j^{n+1}$  and  $Q_{j+1}^{n+1}$ ) in Equations 10.14 and 10.15. The matrix format of Equation 10.21 is presented below:

$$\begin{bmatrix}
\frac{\partial B_1}{\partial Q_1} & \frac{\partial B_1}{\partial h_1} & 0 & 0 & 0 & 0 & \dots & 0 & 0 & 0 & 0 \\
\frac{\partial C_1}{\partial Q_1} & \frac{\partial C_1}{\partial h_1} & \frac{\partial C_1}{\partial Q_2} & \frac{\partial C_1}{\partial h_2} & 0 & 0 & \dots & 0 & 0 & 0 & 0 \\
\frac{\partial M_1}{\partial Q_1} & \frac{\partial M_1}{\partial h_1} & \frac{\partial M_1}{\partial Q_2} & \frac{\partial M_1}{\partial h_2} & 0 & 0 & \dots & 0 & 0 & 0 & 0 \\
0 & 0 & \frac{\partial C_2}{\partial Q_2} & \frac{\partial C_2}{\partial h_2} & \frac{\partial C_2}{\partial Q_3} & \frac{\partial C_2}{\partial h_3} & \dots & 0 & 0 & 0 & 0 \\
0 & 0 & \frac{\partial M_2}{\partial Q_2} & \frac{\partial M_2}{\partial h_2} & \frac{\partial M_2}{\partial Q_3} & \frac{\partial M_2}{\partial h_3} & \dots & 0 & 0 & 0 & 0 \\
\vdots & \vdots & \vdots & \vdots & \vdots & \vdots & \dots & \vdots & \vdots & \vdots & \vdots \\
0 & 0 & 0 & 0 & 0 & 0 & \dots & \frac{\partial C_{M-1}}{\partial Q_{M-1}} & \frac{\partial C_{M-1}}{\partial h_{M-1}} & \frac{\partial C_{M-1}}{\partial Q_M} & \frac{\partial C_{M-1}}{\partial h_M} \\
0 & 0 & 0 & 0 & 0 & 0 & \dots & \frac{\partial M_{M-1}}{\partial Q_{M-1}} & \frac{\partial M_{M-1}}{\partial h_{M-1}} & \frac{\partial M_{M-1}}{\partial Q_M} & \frac{\partial M_{M-1}}{\partial h_M} \\
0 & 0 & 0 & 0 & 0 & 0 & \dots & 0 & 0 & \frac{\partial B_M}{\partial Q_M} & \frac{\partial B_M}{\partial h_M}
\end{bmatrix}
\begin{bmatrix}
\Delta Q_1 \\
\Delta h_1 \\
\Delta Q_2 \\
\Delta h_2 \\
\Delta Q_3 \\
\Delta h_3 \\
\vdots \\
\vdots \\
\Delta Q_M \\
\Delta h_{NM}
\end{bmatrix}
= -
\begin{bmatrix}
B_1 \\
C_1 \\
M_1 \\
C_2 \\
M_2 \\
\vdots \\
\vdots \\
C_{M-1} \\
M_{M-1} \\
B_M
\end{bmatrix}
\quad (10.22)$$

The solution of this system is obtained by matrix inversion (here using the Matlab resource:  $X=-\backslash R$ ), providing the corrections to the initial values of  $h_j^{n+1}$ ,  $h_{j+1}^{n+1}$ ,  $Q_j^{n+1}$  and  $Q_{j+1}^{n+1}$  in the next iteration, as shown in Equations 10.23 and 10.24.

$$(Q_j^{n+1})^{k+1} = (Q_j^{n+1})^k + \Delta Q_j \quad (10.23)$$

$$(h_j^{n+1})^{k+1} = (h_j^{n+1})^k + \Delta h_j \quad (10.24)$$

The procedure is repeated until the corrections are reduced to a given tolerable values:

$$|Q_j^{k+1} - Q_j^k| \leq \varepsilon_Q \text{ and } |h_j^{k+1} - h_j^k| \leq h_Q \quad (10.25)$$

Alternatively, the repetition can also be stopped when maximum number of iterations ( $N_{max}$ ) is achieved.

### The Crank Nicolson Scheme

This scheme is given by the application of a central difference in space and the trapezoidal method for time advance in the diffusive wave approximation, as showed in Equation 10.26.

$$\begin{aligned} & \frac{Q_j^{n+1} - Q_j^n}{\Delta t} + \frac{C_e}{2} \left[ \left( \frac{Q_{j+1} - Q_{j-1}}{2\Delta x} \right)^n + \left( \frac{Q_{j+1} - Q_{j-1}}{2\Delta x} \right)^{n+1} \right] \\ & - \frac{D}{2} \left[ \left( \frac{Q_{j+1} - 2Q_j + Q_{j-1}}{\Delta x^2} \right)^n + \left( \frac{Q_{j+1} - 2Q_j + Q_{j-1}}{\Delta x^2} \right)^{n+1} \right] = 0 \end{aligned} \quad (10.26)$$

After some manipulations and placing the time level index  $n + 1$  in the left side, Equation 10.26 becomes:

$$\begin{aligned} & -Q_j^{n+1} \left( \frac{C_a}{4} + \frac{C_d}{2} \right) + Q_j^{n+1} (1 + C_d) + Q_{j+1}^{n+1} \left( \frac{C_a}{4} - \frac{C_d}{2} \right) \\ & = Q_{j-1}^n \left( \frac{C_d}{2} + \frac{C_a}{4} \right) + Q_j^n (1 - C_d) - Q_{j+1}^n \left( \frac{C_a}{4} - \frac{C_d}{2} \right) \end{aligned} \quad (10.27)$$

Where  $C_a$  is the Courant number and  $C_d$  is the diffusive Courant number, given by:

$$C_a = C_e \frac{\Delta t}{\Delta x} \quad (10.28)$$

$$C_d = D \frac{\Delta t}{\Delta x^2} \quad (10.29)$$

One should consider that Equation 10.27 can be applied in nodes  $j = 2$  to  $M - 1$ . Then, the system of equation is completed using an initial condition  $Q(x, 0)$  and two equations given by the assumed boundary conditions. For the upstream boundary  $Q(0, t)$ , the discharge must be known in advance. For the downstream boundary, a possible solution is to consider the hydraulic diffusivity equal to zero using the upwind scheme. The Crank Nicolson scheme is then solved in matrix format:



Once the solution of the discharges is known, the flow depth can be obtained by the discretization of the continuity equation. To keep the accuracy of the model (second order) the leap-frog scheme can be applied in the internal nodes:

$$h_j^{n+1} = h_j^{n-1} - \frac{\Delta t}{W\Delta x} (Q_{j+1}^n - Q_{j-1}^n) \quad (10.32)$$

In the nodes close to boundaries the first order upwind scheme is then applied:

$$h_j^{n+1} = h_j^n - \frac{\Delta t}{W\Delta x} \left( \frac{Q_{j+1}^n - Q_j^n}{\Delta x} \right) \quad (10.33)$$

The solution of the equations above requires the initial condition  $h(x, 0)$ , the upstream boundary condition  $h(0, t)$  and the downstream boundary condition  $h(M, t)$ . A common initial condition is to consider the uniform flow for a given discharge. The upstream condition can be obtained using a depth-discharge curve applied to the upstream hydrograph. Finally, the downstream boundary condition can be either a depth-discharge curve or a constant water level, for the case where there is a reservoir downstream.

#### The QUICKEST Scheme

The QUICKEST (Quadratic Upstream Interpolation for Convective Kinematics with Estimated Streaming Terms) is an explicit, third-order approximation to solve unsteady flows in format of advection-diffusion (diffusive wave) developed by Leonard (1979). The method is non-diffusive, however due its explicit nature it is conditionally stable scheme, which limits are defined as function of the Courant numbers and the Peclet number. This scheme is given by Equation 10.34:

$$\begin{aligned}
Q_j^{n+1} = & Q_j^n + \left[ C_d(1 - C_a) - \frac{C_a}{6}(C_a^2 - 3C_a + 2) \right] Q_{j+1}^n \\
& - \left[ C_d(2 - 3C_a) - \frac{C_a}{2}(C_a^2 - 2C_a - 1) \right] Q_j^n \\
& + \left[ C_d(1 - 3C_a) - \frac{C_a}{2}(C_a^2 - C_a - 2) \right] Q_{j-1}^n + \left[ C_d(C_a) + \frac{C_a}{6}(C_a^2 - 1) \right] Q_{j-2}^n
\end{aligned} \tag{10.34}$$

The solution requires an initial condition, the upstream and downstream boundary conditions. Moreover, a different scheme is required in the nodes near the boundaries. Likewise the Crank Nicolson scheme, once the solution of the discharges is known, the flow depth can be obtained by the application of the continuity equation.

#### Modified Puls

This method is also known as the Level Pool Routing and it is a hydrologic routing based on conservation of mass, written as the storage differential equation:

$$\frac{dS}{dt} = I(t) - O(t) \tag{10.35}$$

Where  $S$  is the reservoir storage,  $I(t)$  is the inflow and  $O(t)$  is the outflow. The Modified Puls approach is usually applied for flood routing in reservoirs. Nevertheless, its use in channels can be made by the segmentation of the channel in several sub-reaches. The method is then applied in each segment according with the storage equation, written as (Chow, 1988; Szymkiewicz, 2010):

$$\frac{2S(t_{i+1})}{\Delta t} + O(t_{i+1}) = [I(t_{i+1}) + I(t_i)] + \left[ \frac{2S(t_i)}{\Delta t} - O(t_i) \right] \tag{10.36}$$

The Modified Puls routing approach assumes that the storage and the outflow are function of the water level elevation only. Hence, the left-hand side of the Equation 10.36 depends only of the water level elevation in the system. In general, the storage-elevation curve is a common data of reservoirs and the outflow-elevation relationship depends on the type of

hydraulic structure (e.g. spillways, etc.) and its operation. The solution for the level pool routing is given by the development of a function  $2S/\Delta t + O = f(O)$  and proceeding with the routing of the inflow hydrograph. The outflow hydrograph is obtained applying this procedure for every time step sequentially (Ramirez, 2015).

### Muskingum-Cunge

The Muskingum-Cunge method is a modification of the Muskingum method where the diffusive wave approximation takes place instead of the kinematic-wave. In general, the wide rectangular channel assumption is implicit on its derivation. This method is given by Equation 10.37 (Szymkiewicz, 2010):

$$Q_j^{n+1} = C_1 Q_{j-1}^n + C_2 Q_j^n + C_3 Q_{j-1}^{n+1} \quad (10.37)$$

The coefficients  $C_1$ ,  $C_2$  and  $C_3$  are given by:

$$C_1 = \frac{KX + 0.5\Delta t}{K(1 - X) + 0.5\Delta t} \quad (10.38)$$

$$C_2 = \frac{K(1 - X) - 0.5\Delta t}{K(1 - X) + 0.5\Delta t} \quad (10.39)$$

$$C_3 = \frac{-KX + 0.5\Delta t}{K(1 - X) + 0.5\Delta t} \quad (10.40)$$

Where the parameters  $K$  and  $X$  are equal to:

$$K = \frac{C_e}{\Delta x} \quad (10.41)$$

$$X = 0.5 - \frac{Q}{2WS_oKC_e^2} \quad (10.42)$$

These parameters can be kept constant to a chosen reference discharge or updated using the known discharges at every time step. The method application is simple, however the accuracy highly depends on the river bed slope, since the method can lead to underestimation of the peak flow in mild slopes (Fenton, 2011).

## APPENDIX D

### The Crank Nicolson Scheme Applied on Suspended Sediment Transport and Deposition

The Crank Nicolson scheme can be applied on the sediment concentration, taking in account the settling term  $k$  (Chapra, 2008):

$$\begin{aligned}
 & -C_{j-1}^{n+1} \left( \frac{C_{as}}{4} + \frac{C_{ds}}{2} \right)_j^n + C_j^{n+1} \left( 1 + C_{ds} + \frac{k\Delta t}{2} \right)_j^n + C_{j+1}^{n+1} \left( \frac{C_{as}}{4} - \frac{C_{ds}}{2} \right)_j^n \\
 & = C_{j-1}^n \left( \frac{C_{as}}{4} + \frac{C_{ds}}{2} \right)_j^n \\
 & + C_j^n \left( 1 - C_{ds} - \frac{k\Delta t}{2} \right)_j^n - C_{j+1}^n \left( \frac{C_{as}}{4} - \frac{C_{ds}}{2} \right)_j^n
 \end{aligned} \tag{10.43}$$

Where  $C_j^n$  refers to the suspended sediment concentration at the cross section  $j$  and in the time level  $n$  in the computational grid. In addition,  $C_{as}$  is the Courant number and  $C_{ds}$  is the diffusive Courant number, given by:

$$C_{as} = U \frac{\Delta t}{\Delta x} \tag{10.44}$$

$$C_{ds} = K_d \frac{\Delta t}{\Delta x^2} \tag{10.45}$$

One should consider that the Equation 10.43 can be applied in nodes  $j = 2$  to  $M - 1$ . Then, the system of equation is completed using an initial condition  $C(x, 0)$  and two boundary conditions. For the upstream boundary  $C(0, t)$ , the sediment concentration must be known in advance. For the downstream boundary, a possible solution is to consider the longitudinal dispersion coefficient equal to zero, applying then the upwind scheme. Thus, the Crank Nicolson scheme can be written in the matrix format:

$$\begin{aligned}
& \begin{bmatrix} \left(1 + C_{ds} + \frac{k\Delta t}{2}\right)_2 & \left(\frac{C_{as}}{4} - \frac{C_{ds}}{2}\right)_2 & & & \\ -\left(\frac{C_{as}}{4} + \frac{C_{ds}}{2}\right)_3 & \left(1 + C_{ds} + \frac{k\Delta t}{2}\right)_3 & \left(\frac{C_{as}}{4} - \frac{C_{ds}}{2}\right)_3 & & \\ & \dots & \dots & \dots & \\ & & -\left(\frac{C_{as}}{4} + \frac{C_{ds}}{2}\right)_{M-1} & \left(1 + C_{ds} + \frac{k\Delta t}{2}\right)_{M-1} & \left(\frac{C_{as}}{4} - \frac{C_{ds}}{2}\right)_{M-1} \\ & & & -\left(\frac{C_{as}}{2}\right)_M & \left(1 + \frac{C_{as}}{2}\right)_M \end{bmatrix} \begin{bmatrix} C_2 \\ C_3 \\ \dots \\ C_{M-1} \\ C_M \end{bmatrix}^{n+1} \\
& = \begin{bmatrix} \left(1 - C_{ds} - \frac{k\Delta t}{2}\right)_2 & -\left(\frac{C_{as}}{4} - \frac{C_{ds}}{2}\right)_2 & & & \\ \left(\frac{C_{ds}}{2} + \frac{C_{as}}{4}\right)_3 & \left(1 - C_{ds} - \frac{k\Delta t}{2}\right)_3 & -\left(\frac{C_{as}}{4} - \frac{C_{ds}}{2}\right)_3 & & \\ & \dots & \dots & \dots & \\ & & \left(\frac{C_{ds}}{2} + \frac{C_{as}}{4}\right)_{M-1} & \left(1 - C_{ds} - \frac{k\Delta t}{2}\right)_{M-1} & -\left(\frac{C_{as}}{4} - \frac{C_{ds}}{2}\right)_{M-1} \\ & & & \left(\frac{C_{as}}{2}\right)_M & \left(1 - \frac{C_{as}}{2}\right)_M \end{bmatrix} \begin{bmatrix} C_2 \\ C_3 \\ \dots \\ C_{M-1} \\ C_M \end{bmatrix}^n \\
& + \left(\frac{C_{ds}}{2} + \frac{C_{as}}{4}\right) \begin{bmatrix} C_1^{n+1} + C_1^n \\ 0 \\ \dots \\ 0 \\ 0 \end{bmatrix}
\end{aligned} \tag{10.46}$$

One should note that the courant number and the diffusive courant number are allowed to vary in each node. Thus, this numerical model can be coupled either with a steady or unsteady flow simulation. The calculation of the sediment concentration for the next time steps is made by matrix inversion. Since the resultant matrix is a tridiagonal matrix, one can apply the Thomas algorithm (Chapra & Canale, 2009) or using a built in function, as in Matlab for instance.